A Direct Search for Dirac Magnetic Monopoles

by

Michael James Mulhearn

Submitted to the Department of Physics
in partial fulfillment of the requirements for the degree of

Doctor of Philosophy

at the

MASSACHUSETTS INSTITUTE OF TECHNOLOGY

Oct 2004

© Massachusetts Institute of Technology 2004. All rights reserved.

Author .....
Department of Physics
October 5, 2004

Certified by .....
Christoph M. E. Paus
Associate Professor
Thesis Supervisor

Accepted by .....
Thomas J. Greytak
Associate Department Head for Education

A Direct Search for Dirac Magnetic Monopoles

by

Michael James Mulhearn

Submitted to the Department of Physics
on October 5, 2004, in partial fulfillment of the
requirements for the degree of
Doctor of Philosophy

Abstract

Magnetic monopoles are highly ionizing and curve in the direction of the magnetic field. A new dedicated magnetic monopole trigger at CDF, which requires large light pulses in the scintillators of the time-of-flight system, remains highly efficient to monopoles while consuming a tiny fraction of the available trigger bandwidth. A specialized offline reconstruction checks the central drift chamber for large dE/dx tracks which do not curve in the plane perpendicular to the magnetic field. We observed zero monopole candidate events in 35.7 pb^{-1} of proton-antiproton collisions at $\sqrt{s} = 1.96$ TeV. This implies a monopole production cross section limit $\sigma < 0.2$ pb for monopoles with mass between 100 and 700 GeV, and, for a Drell-Yan like pair production mechanism, a mass limit $m > 360$ GeV.

Thesis Supervisor: Christoph M. E. Paus
Title: Associate Professor

Dedication

To those from whom I've wandered for this work: Mom, Dad, Chris, Maricruz, Meg, Doug, and Katie. And to Mila, whom I found along the way.

Acknowledgments

My thesis advisor, Christoph Paus, knew when to leave me alone and when to lift my spinning tires. Gerry Bauer and Sham Sumorok were always willing to listen.

My fellow students shattered the myth of divisive competitiveness at MIT; we worked to get through graduate school together. Ivan Furic was alongside from beginning to end. My friends and colleagues at Fermilab gave crucial support and encouragement; the dinner club tempered their's by calling this a "purple elephant search". Daniel Whiteson has consistently given me advice better than his years entitle him to.

The idea for this thesis came from Jonathan Lewis and David Stuart. Jonathan was a key ally from the beginning. Arnd Meyer, Peter Wilson and Bill Badgett were there for the integration. Mathew Jones helped stretch the TOF electronics into a trigger. Eric James wrote new firmware for the muon trigger, Theresa Shaw for the ADMEM, and Carla Pilcher for PreFRED. Philipp Schieferdecker wrote the original GEANT simulation code, and Steve Tether worked out the Runge-Kutta integration. Alex Madorsky designed the TOTRIB and taught me how to write drivers; that was the best part of this thesis.

Contents

1 Introduction **17**

2 Theory **19**

2.1 The Duality Transformation 19

2.2 Motion in a Magnetic Field 20

2.3 Dirac's Quantization Condition 22

2.4 Magnetic-Electric Interactions 24

2.5 Monopole Pair Production 26

2.6 Ionization and Delta Rays 27

2.7 Multiple Scattering 29

2.8 Çerenkov Radiation 30

3 Tevatron and CDF Detector **31**

3.1 Tevatron 32

3.2 The CDF Detector 35

3.3 Standard Definitions at CDF 38

3.4 Central Outer Tracker (COT) 40

3.5 Time of Flight 44

3.6 The CDF Trigger 45

4 Time-of-Flight Trigger **49**

4.1 TOMAIN and TOF ADMEMs 51

4.1.1 Technical Description 52

4.1.2 Channel Swappers 54
4.1.3 Software 56
4.2 Trigger Cables and Patch Panel 58
4.3 TOTRIB 60
4.3.1 Technical Description 60
4.3.2 Detector Coverage, Channel Definitions and Data Path 64
4.3.3 The Input, Algorithm and Output 67
4.3.4 VME Interface 68
4.4 Muon Matchbox and Muon PreFRED 70
4.5 BSC-TOF PreFRED 71
4.6 Timing 73
4.7 Trigger Tables 75

5 Adding Monopoles to GEANT 77
5.1 Code Layout 78
5.2 Monopole Tracking 80
5.3 Energy Loss and Delta Rays 82
5.4 Multiple Scattering 84
5.5 Code Validation 85
5.5.1 Comparison with a Stand-Alone Simulation 85
5.5.2 Comparison between analytic and Runge-Kutta solutions . . . 88
5.6 Summary 89

6 Trigger Efficiency and Dataset 97
6.1 Acceptance 97
6.2 Electronics Response 104
6.3 Spoilers 109
6.4 Timing 118
6.5 Digital Response 119
6.6 Dataset 122

7 Candidate Selection **123**

7.1 Width Cut 125

7.2 Segment Finding 129

8 Results **139**

A Time-of-Flight Trigger Details **147**

List of Figures

2-1 A monopole-electron collision 23
2-2 The crossing symmetry of monopole-electron interactions 26
2-3 Monopole production cross section 27
2-4 Energy loss of monopoles and protons 29

3-1 The Fermilab accelerator complex 32
3-2 Peak instantaneous luminosity 35
3-3 The CDF detector 36
3-4 CDF tracking sub-detectors 40
3-5 COT Wire planes 41
3-6 COT super-cell 42
3-7 CDF trigger 46

4-1 TOF trigger electronics 50
4-2 TOF ADMEM block schematic 53
4-3 Origin of channel swapping 55
4-4 The Qietest menu 57
4-5 TOF trigger cables 58
4-6 TOF trigger cable shield grounding 59
4-7 TOTRIB connector labels 61
4-8 TOTRIB Block Schematic 62
4-9 CDF clock signal 63
4-10 CDF bunch zero signal 63
4-11 CDF recover signal 64

4-12 CDF halt signal 64
4-13 HIP and MIP trigger bit definitions 65
4-14 TOTRIB coverage 65
4-15 TOTRIB data path 66
4-16 TOF cosmic trigger algorithm 72
4-17 Fine Timing 73
4-18 TOF trigger timing diagram 74

5-1 GEANT tracking package 78
5-2 Monopole tracking algorithm 80
5-3 Energy loss of protons in air 83
5-4 Energy loss of monopole in air 84
5-5 TOF acceptance comparison 86
5-6 Energy difference at TOF for GEANT and MonSim 87
5-7 z difference at TOF for GEANT and MonSim 88
5-8 ϕ difference at TOF for GEANT and MonSim 89
5-9 Typical r-z trajectory comparison 90
5-10 Typical E-r trajectory comparison 91
5-11 Tail r-z trajectory comparison 92
5-12 Tail E-r trajectory comparison 93
5-13 Energy difference at TOF for different algorithms 94
5-14 z difference at TOF for different algorithms 95
5-15 ϕ difference at TOF for different algorithms 96

6-1 TOF acceptance 98
6-2 TOF acceptance PDF dependence 99
6-3 TOF acceptance kinematic model dependence 100
6-4 Kinematics of $m = 200$ GeV Monopoles 101
6-5 Kinematics of $m = 400$ GeV Monopoles 102
6-6 Kinematics of $m = 700$ GeV Monopoles 103
6-7 TOF data calibration 105

6-8 TOF calibrated charge distribution 107
6-9 Calibrated TOF trigger thresholds 108
6-10 TOF laser calibration 110
6-11 Response function from TOF laser calibration 111
6-12 Comparison of non-linear behavior 112
6-13 Z mass distribution 114
6-14 TOF spoilers 115
6-15 TOF spoiler luminosity dependence 116
6-16 TOF spoiler sum p_{T} dependence 117
6-17 TOF pulse arrival times 118
6-18 TOF timing window 120
6-19 TOF timing efficiency 121

7-1 The monopole search 124
7-2 Corrected COT universal curve 126
7-3 COT width response 127
7-4 Logarithmic extrapolation of COT width response 128
7-5 COT raw hit distribution 130
7-6 Run dependence of COT universal curve 131
7-7 Segment curvature in Monte Carlo 132
7-8 Segment ϕ_0 in Monte Carlo 133
7-9 Segment finding efficiency on high p_{T} tracks 134
7-10 Segment finding efficiency with Monte Carlo 135
7-11 Background estimate from minimum bias data 137

8-1 Monopole cross section limit ($n = 1$) 141
8-2 Monopole cross section limit ($n = 2$) 143
8-3 Comparison with previous limits 144
8-4 Background estimate from trigger data 145
8-5 Nearest candidate 146

A-1 Coincidence data schematic 149

List of Tables

3.1 Accelerator parameters 34

4.1 TOF ADMEM trigger lookup table 54

4.2 Simple XTRP algorithm for TOF 70

4.3 BSC-TOF PreFRED bit assignment 71

4.4 TOF trigger timing parameters 75

4.5 Trigger table parameters 76

8.1 Summary of efficiency 140

A.1 TOF hardware locations 147

A.2 TOF ADMEM pedestal register addresses 147

A.3 CDF control signals 148

A.4 Additional CDF control signals 148

A.5 TOTRIB input channel definitions (first 30°) 149

A.6 TOTRIB input channel definitions (second 30°) 150

A.7 TOTRIB input channel definitions (last 30°) 150

A.8 TOTRIB output channel mapping (first 30°) 151

A.9 TOTRIB output channel mapping (second 30°) 152

A.10 TOTRIB output channel mapping (last 30°) 153

A.11 TOTRIB MIP front-panel connector A3 channel mapping 154

A.12 TOTRIB MIP front-panel connector B3 channel mapping 154

A.13 TOTRIB C0 connector output channel mapping 155

A.14 TOTRIB C1 connector output channel mapping 156

A.15 TOTRIB VME registers 156
A.16 XTRP crack bits 157
A.17 Muon Matchbox HIP bits 157

Chapter 1

Introduction

The existence of magnetic monopoles would add symmetry to Maxwell's equations [1] without breaking any known physical law. More dramatically, it would make charge quantization a consequence of angular momentum quantization, as first shown by Dirac [2]. With such appeal, monopoles continue to excite interest and new searches despite their elusiveness to date.

Grand unified theories predict monopole masses of about 10^{17} TeV, so there have been extensive searches for high-mass monopoles produced by cosmic rays [3]. Indirect searches for low-mass monopoles have looked for the effects of virtual monopole/anti-monopole loops added to QED Feynman diagrams [4]. Detector materials exposed to radiation from $p\bar{p}$ collisions at the Tevatron have been examined for trapped monopoles [5]. All results have been negative [6].

This thesis entails a search for Dirac monopoles with mass less than 1 TeV at CDF. By a "Dirac" monopole, we mean a particle without electric charge or hadronic interactions and with magnetic charge g satisfying the Dirac quantization condition:

$$\frac{ge}{\hbar c} = \frac{n}{2} \Longleftrightarrow \frac{g}{e} = \frac{n}{2\alpha} \approx 68.5 \cdot n$$

Dirac magnetic monopoles are highly ionizing due to the large value of g. In the CDF detector, they are accelerated in the direction of the solenoidal magnetic field, causing relativistically stretched parabolic trajectories. This is in sharp contrast to ordinary

charged particles, which are circular in the plane perpendicular to the magnetic field.

Because of the unique signature from monopoles, it is possible to effectively eliminate background while maintaining high efficiency. By demonstrating monopole consistent behavior throughout the detector, we expect that a single observed event could be compellingly claimed a discovery.

With such a loud signal, the main challenge of the search is to effectively trigger on magnetic monopoles. CDF cannot possibly record every event, and so physics triggers are needed to make full use of the available luminosity. We have built and commissioned a dedicated highly ionizing particle (HIP) trigger, which requires large light pulses in CDF's Time-of-Flight (TOF) detector. The trigger is highly efficient and consumes a tiny fraction of CDF's bandwidth.

Triggered events are recorded to tape for additional analysis offline. For this search, a specialized reconstruction isolates monopole candidates by checking for abnormally high ionization and non-curvature in $r - \phi$ using CDF's main tracking chamber.

In the remaining chapters, we discuss the theory of magnetic monopoles, the detector and trigger, the monopole simulation, the trigger efficiency, and event selection. We then present results.

Chapter 2

Theory

The original theoretical justification for magnetic monopoles is that they add symmetry to Maxwell's equations [1] and explain charge quantization in terms of angular momentum quantization. More recently, grand unified theories (GUTs) have predicted the existence of magnetic monopoles, but at masses beyond the reach of any presently conceivable particle accelerator [6, 7].

This chapter explores the new symmetry, the Dirac quantization condition, and a possible production mechanism. The properties of a magnetic monopole, its trajectory and interactions with material, are examined to see how one could be detected.

2.1 The Duality Transformation

The Maxwell equations extended to include magnetic charge take the following form:

$$\begin{aligned} \vec{\nabla} \cdot \vec{D} &= 4\pi \rho_{\mathrm{e}} \\ \vec{\nabla} \cdot \vec{B} &= 4\pi \rho_{\mathrm{m}} \\ -\vec{\nabla} \times \vec{E} &= \frac{\partial}{\partial t}\vec{B} + 4\pi \vec{j}_{\mathrm{m}} \\ \vec{\nabla} \times \vec{H} &= \frac{\partial}{\partial t}\vec{D} + 4\pi \vec{j}_{\mathrm{e}} \end{aligned} \tag{2.1}$$

As usual, $\vec{E}$ is the electric field, $\vec{D}$ the electric displacement, $\vec{B}$ the magnetic induction, and $\vec{H}$ the magnetic field. The quantities $\rho_{\rm e}$ and $\vec{j}_{\rm e}$ are the familiar electric charge density and electric current density. The addition of magnetic charge introduces $\rho_{\rm m}$ and $\vec{j}_{\rm m}$, the magnetic charge density and magnetic current density.

The form of these equations is invariant under a general duality transformation ($\xi \in \Re$):

$$\begin{aligned} \vec{E} &= \vec{E}' \cos\xi + \vec{H}' \sin\xi & \vec{D} &= \vec{D}' \cos\xi + \vec{B}' \sin\xi \\ \vec{H} &= -\vec{E}' \sin\xi + \vec{H}' \cos\xi & \vec{B} &= -\vec{D}' \sin\xi + \vec{B}' \cos\xi \\ \rho_{\rm e} &= \rho'_{\rm e} \cos\xi + \rho'_{\rm m} \sin\xi & \vec{j}_{\rm e} &= \vec{j}'_{\rm e} \cos\xi + \vec{j}'_{\rm m} \sin\xi \\ \rho_{\rm m} &= -\rho'_{\rm e} \sin\xi + \rho'_{\rm m} \cos\xi & \vec{j}_{\rm m} &= -\vec{j}'_{\rm e} \sin\xi + \vec{j}'_{\rm m} \cos\xi \end{aligned} \tag{2.2}$$

The original Maxwell equations are recovered if all particles have the same ratio of magnetic charge to electric charge, which can be set to zero by the right choice of the angle ξ. A useful special case of the duality transformation is when $\xi = \pi/2$; the extended Maxwell equations are invariant under the replacements

$$\begin{aligned} \rho_{\rm e} &\to \rho_{\rm m} & \vec{j}_{\rm e} &\to \vec{j}_{\rm m} & \vec{E} &\to \vec{H} & \vec{D} &\to \vec{B} \\ \rho_{\rm m} &\to -\rho_{\rm e} & \vec{j}_{\rm m} &\to -\vec{j}_{\rm e} & \vec{B} &\to -\vec{D} & \vec{H} &\to -\vec{E} \end{aligned} \tag{2.3}$$

This is the transformation meant by "duality" or the "dual" of an EM quantity. Magnetic charge and electric charge are mirror images of one another, and interchangeable. Apart from being theoretically satisfying, this duality can be used to derive monopole versions of formulas familiar from standard classical electrodynamics.

2.2 Motion in a Magnetic Field

Duality implies a Lorentz force law for a magnetic monopole carrying magnetic charge g:

$$\vec{F} = g(\vec{B} - \vec{\beta} \times \vec{E}) \tag{2.4}$$

A magnetic monopole interacts with a magnetic field as an electron interacts with an electric field.

The general case requires a numerical integration, but the motion in a uniform magnetic field can be solved analytically. Unlike the non-relativistic case, the differential equation

$$\frac{d\vec{p}}{dt} = g\vec{B} \tag{2.5}$$

couples the different coordinates due to the presence of γ in the momentum: $p_i = \gamma m \beta_i$.

We take the uniform magnetic field to be along the z axis, $\vec{B} = B_0\hat{z}$, and start with the special case of the initial momentum perpendicular to the magnetic field: $\vec{p_0} = p_0\hat{x}$. An integration of Equation 2.5 leads to

$$p_z = \gamma m \beta_z = gB_0 t \tag{2.6}$$

$$p_x = \gamma m \beta_x = p_0 \tag{2.7}$$

and eliminating gamma gives

$$\beta_z = \beta_x \cdot \frac{gB_0 t}{p_0}$$

which can be used to decouple the z and x coordinates to obtain:

$$\beta_z = \frac{gB_0 t}{\sqrt{m^2 + p_0^2 + gB_0 t}} \tag{2.8}$$

$$\beta_x = \frac{p_0}{\sqrt{m^2 + p_0^2 + gB_0 t}} \tag{2.9}$$

One more integration provides the equation of motion:

$$\vec{r}(t) = \frac{p_0}{gB_0}\sinh^{-1}(\frac{gB_0 t}{E_{t0}})\hat{z} + \frac{\sqrt{E_{t0}^2 + (gB_0 t)^2} - E_{t0}^2}{gB_0}\hat{x} \tag{2.10}$$

where $E_{t0} = \sqrt{m^2 + p_{x0}}$ is the initial transverse energy, equivalent to the total initial energy in this special case.

This special solution handles monopoles with arbitrary initial transverse momen-

tum. Since the monopole is accelerated by the magnetic field, the momentum along the magnetic field will take on every possible value, while the transverse momentum remains constant. This means the general solution can be obtained by translating the special solution in space and time. From the differential equation for the z coordinate, the time translation needed is:

$$\Delta t = p_{z0}/gB_0 \tag{2.11}$$

Translating the special solution by this amount of time, and moving the origin to t=0 we obtain the general solution:

$$\begin{aligned}\vec{r}(t) =& \frac{p_0}{gB_0}(\sinh^{-1}(\frac{gB_0(t+\Delta t}{E_{t0}}) - \sinh^{-1}(\frac{gB_0\Delta t}{E_{t0}}))\hat{z} \\ &+ \frac{E_t 0}{gB_0}(\sqrt{1+\frac{(gB_0(t+\Delta t))^2}{E_{t0}^2}} - \sqrt{1+\frac{(gB_0\Delta t)^2}{E_{t0}^2}})\hat{x}\end{aligned} \tag{2.12}$$

This describes a parabola, stretched by relativity, accelerating in the direction of the magnetic field. In the plane perpendicular to the magnetic field, the motion is in a straight line, in sharp contrast to electrically charged particles, which curve in this plane.

2.3 Dirac's Quantization Condition

The classical derivation of Dirac's Quantization Condition [1] is obtained by considering the angular momentum transfered to a magnetic monopole by a collision with an electron.

The magnetic monopole moves parallel to the x axis at constant velocity β, interacting with the electron located on the origin as shown in Figure 2-1. We consider the case where the impact parameter d is large: a glancing collision.

The force on the magnetic monopole is given by

$$\vec{F} = g\vec{\beta} \times \vec{E} \tag{2.13}$$

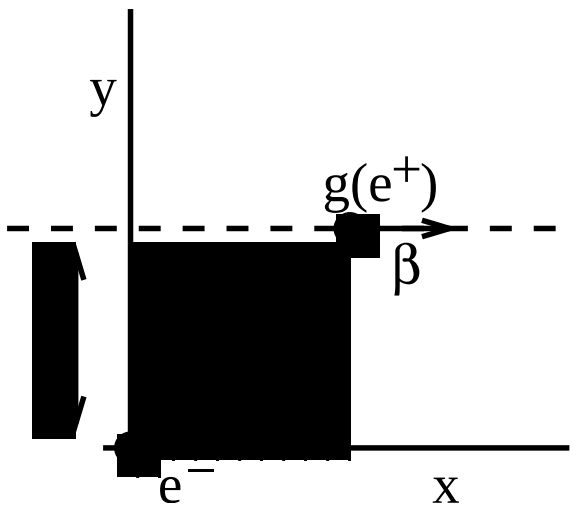

Figure 2-1: A monopole (or positron) makes a glancing collision with an electron located at the origin.

where the electric field from the electron is

$$\vec{E} = -e\frac{\vec{r}}{r^3} \tag{2.14}$$

leading to

$$\begin{aligned} F_z &= \frac{-\beta ged}{(d^2 + (\beta ct)^2)^{\frac{3}{2}}} \\ F_x &= F_y = 0 \end{aligned} \tag{2.15}$$

The only non-zero force acting on the monopole is along the z axis, which causes a net impulse

$$\Delta p_z = \int_{-\infty}^{+\infty} F_z dt = \int_{-\infty}^{+\infty} \frac{-\beta geddt}{(d^2 + (\beta ct)^2)^{\frac{3}{2}}} = \frac{-2eg}{cd} \tag{2.16}$$

The angular momentum transfered is

$$|\Delta\vec{L}| = |\vec{r} \times \Delta\vec{p}| = d \cdot \Delta p_z = \frac{2eg}{c} \tag{2.17}$$

The Dirac quantization condition is obtained by noting that this angular momentum

transfer must come in integral quantities of $\hbar$, leading to:

$$eg = \frac{n\hbar c}{2} \tag{2.18}$$

The Dirac quantization condition implies that

$$g/e = \frac{n}{2\alpha} \sim 68.5n \tag{2.19}$$

This means that the magnetic charge quanta, g, is quite large. For an ion, we write the total electric charge as ze where z is the atomic charge. Likewise, we write the total magnetic charge as ng where n is the quantum number from the Dirac quantization condition.

2.4 Magnetic-Electric Interactions

As a monopole passes through a medium, it interacts with the atoms in the medium. To understand the nature of these magnetic-electric interactions [8], we first consider the effect of the passing monopole in Figure 2-1 on the electron at the origin. To obtain the field of the moving monopole, we find the field of a moving positron, and use duality to obtain the field for a magnetic monopole.

The electromagnetic field at the origin in a frame moving with the positron is given by

$$E_x = \frac{e\beta t}{(d^2 + (\beta t)^2)^{\frac{3}{2}}} \tag{2.20}$$

$$E_y = \frac{ed}{(d^2 + (\beta t)^2)^{\frac{3}{2}}} \tag{2.21}$$

with all other field components zero. Recalling the Lorentz transformation for electromagnetic fields in terms of the field parallel ($\|$) and perpendicular ($\perp$) to the velocity

vector [1],

$$E'_{\parallel} = E_{\parallel}, \qquad \vec{E}'_{\perp} = \gamma(\vec{E}_{\perp} + \vec{\beta} \times \vec{B}) \tag{2.22}$$

$$B'_{\parallel} = B_{\parallel}, \qquad \vec{B}'_{\perp} = \gamma(\vec{B}_{\perp} - \vec{\beta} \times \vec{E}) \tag{2.23}$$

the non-zero field components due to the moving charge at the origin, in the rest frame of the electron, are

$$E^e_x = \frac{e\beta t}{(d^2 + (\beta t)^2)^{\frac{3}{2}}} \tag{2.24}$$

$$E^e_y = \frac{e\gamma d}{(d^2 + (\beta t)^2)^{\frac{3}{2}}} \tag{2.25}$$

$$B^e_z = \frac{e\beta d}{(d^2 + (\beta t)^2)^{\frac{3}{2}}} \tag{2.26}$$

We obtain the field for a moving monopole by applying the duality transformation:

$$B^g_x = \frac{g\beta t}{(d^2 + (\beta t)^2)^{\frac{3}{2}}} \tag{2.27}$$

$$B^g_y = \frac{g\gamma d}{(d^2 + (\beta t)^2)^{\frac{3}{2}}} \tag{2.28}$$

$$E^g_z = -\frac{g\beta d}{(d^2 + (\beta t)^2)^{\frac{3}{2}}} \tag{2.29}$$

The stationary electron is only affected by the electric fields, and the x averages to zero over the course of the interaction, so the only fields that contribute are E^e_y for the positron and E^g_z for the monopole. We obtain the latter with the replacement

$$e \to \beta g \tag{2.30}$$

Under the naive assumption that the isotropy of matter makes the difference in direction immaterial, a monopole is effectively a passing particle with electrical charge βg. There is, however, a correlated response of matter to the passing monopole which becomes increasingly important for slow moving monopoles and dense media [10]. For nearly relativistic monopoles in a gas, the naive treatment is adequate.

2.5 Monopole Pair Production

Duality suggests a new magnetic coupling constant in analogy with the fine structure constant:

$$\alpha_g = \frac{g^2}{\hbar c} \tag{2.31}$$

Due do the large value of g, this coupling constant is larger than one, which makes monopole production non-perturbative. This means that there is no universally accepted prediction from field theory about the production of monopoles.

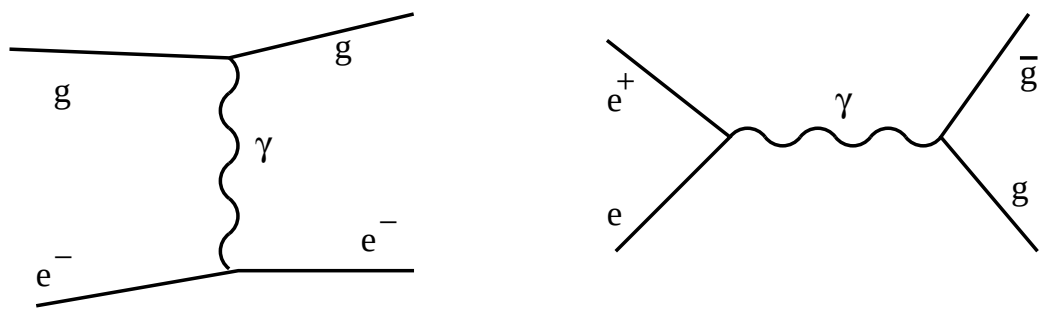

Figure 2-2: Monopole pair production is related to monopole-electron scattering by a crossing symmetry.

However, a physically motivated production model has been suggested [5]. We have seen that the interaction of a monopole with an electron merely makes the replacement $e \to g\beta$. If we imagine how this interaction might look to first order in Quantum Field Theory, we have the diagram on the left of Figure 2-2. But this is related to the Drell-Yan like monopole pair production mechanism, depicted on the right, by a crossing symmetry. It seems reasonable to make the replacement $e \to g\beta$ in the Drell-Yan production mechanism as well. Note that β, the velocity of the monopole pairs in the photon rest frame, is a Lorentz invariant, depending only on the mass of the monopoles and the photon mass. Feynman diagram must be manifestly Lorentz invariant!

This Drell-Yan like monopole pair production mechanism is our primary benchmark. As shown in Figure 2-3, it is the usual Drell-Yan cross section scaled by g/e^2 with a β^2 dependence alongside the usual phase-space β turn on.

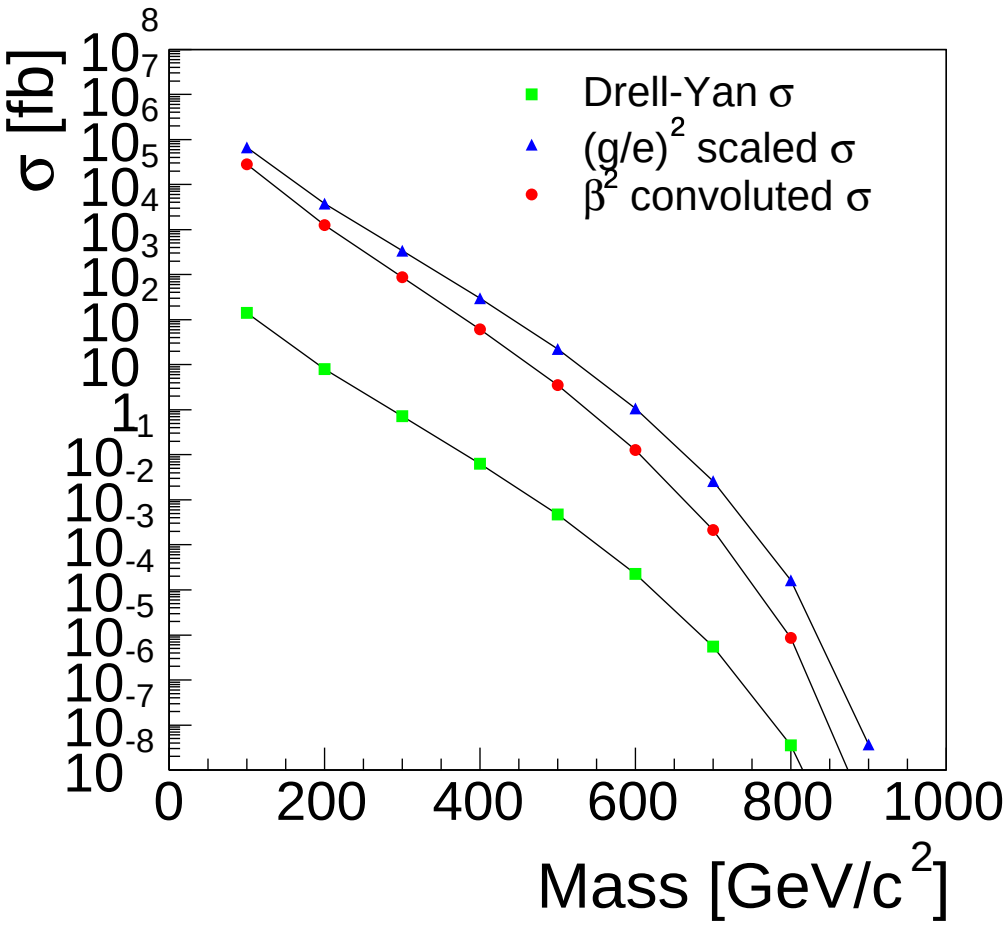

Figure 2-3: The monopole pair production cross section is obtained from the lepton pair production cross section with the replacement $e \rightarrow g\beta$. The normal lepton Drell-Yan cross section is scaled by $(g/e)^2$, then convoluted with a β^2 factor.

2.6 Ionization and Delta Rays

The energy loss per path-length traveled, dE/dx, due to ionization for a particle with electric charge ze is given by the Bethe-Bloch formula [9],

$$-\frac{dE}{dx} = z^2 \frac{KZ}{A} \frac{1}{\beta^2} \left[\frac{1}{2} \ln \left(\frac{2m_{\mathrm{e}}\beta^2\gamma^2}{I^2} \right) - \beta^2 \right] \tag{2.32}$$

where $K = 4\pi N_{\mathrm{A}} r_{\mathrm{e}}^2 m_{\mathrm{e}} c^2$. The properties of the medium are the atomic number Z, the atomic mass A, and the mean excitation energy I. The constants are the electron

mass m_e, classical electron radius r_e and Avogadro's number N_A. Typical values are $K/A = 0.000307$ GeV for $A = 1$ g mol^{-1} and $I = Z \cdot 10$ eV. For now, we omit contributions that are significant for small ionization and dense media, referred to as the shell and density corrections.

This formula is derived by considering the impulse imparted to an electron in the material by the passage of the charged particle [1]. As shown in Section 2.4, replacing the EM field tensor for a moving electric charge by its dual shows that the only field component that delivers a net impulse to the electron is an electric field proportional to both the monopole charge ng and its speed β. The net effect is to replace ze by $ng\beta$:

$$-\frac{dE}{dx} = (ng/e)^2 \frac{KZ}{A} \left[\frac{1}{2} \ln \left(\frac{2m_e \beta^2 \gamma^2}{I^2} \right) - \beta^2 \right]. \tag{2.33}$$

The same conclusion is reached by considering the generalized non-relativistic scattering cross section for small scattering angles [7]. The familiar result for electric-electric scattering (Rutherford scattering),

$$\frac{d\sigma}{d\Omega} \approx \frac{1}{2m\beta} \frac{(ze)^2}{\beta^2} \frac{1}{(\theta/2)^4} \tag{2.34}$$

becomes for magnetic-electric scattering

$$\frac{d\sigma}{d\Omega} \approx \frac{1}{2m\beta} (ng)^2 \frac{1}{(\theta/2)^4} \tag{2.35}$$

where m is the mass of the light particle.

The ionization energy loss for a magnetic monopole in air is compared to an ordinary charged particle in Figure 2-4. There are two differences: the monopole curve is flatter due to canceling of the $1/\beta^2$ factor and higher due to the large value of $g/e \approx 68.5$. The large ionization energy loss means that the range of monopoles in most solid materials is quite short.

To an electron in matter, a passing monopole is effectively a passing nuclei of charge $z \sim n \cdot 68.5 \cdot \beta$. The mean energy loss, energy loss fluctuations, and delta ray production are all different aspects of this interaction. The equations describing these

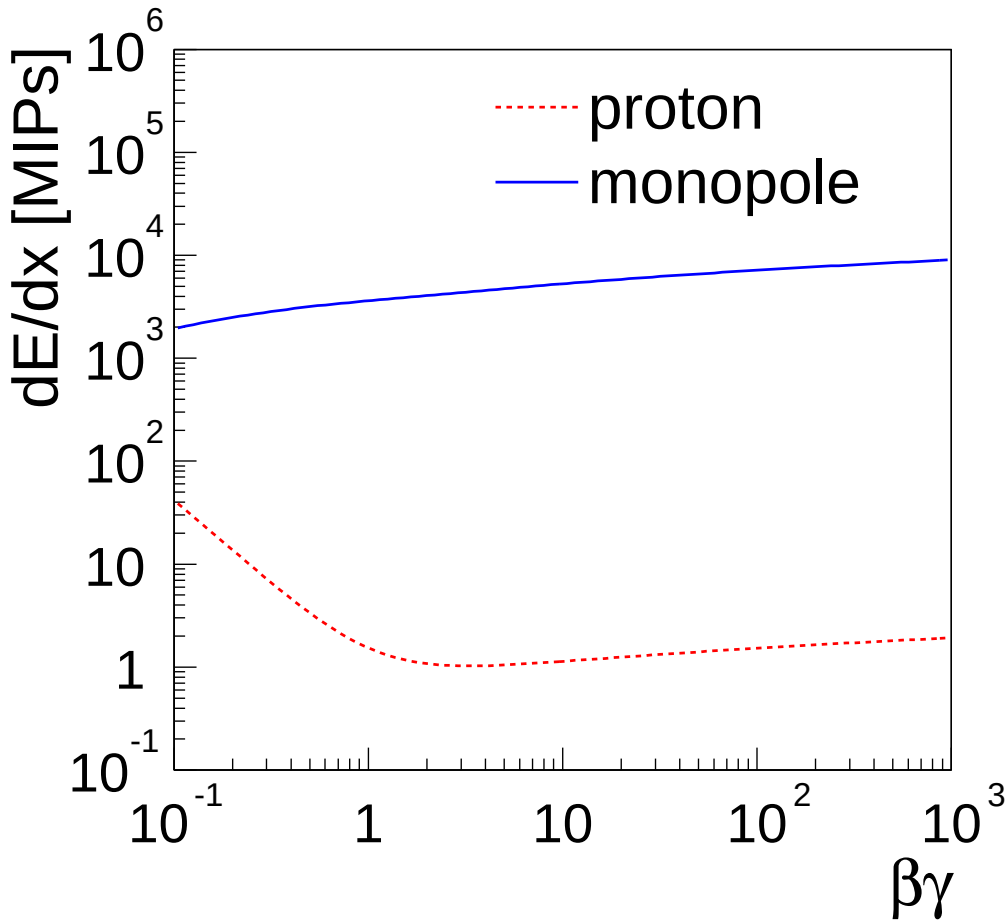

Figure 2-4: The energy loss of monopoles and protons in air.

phenomena are valid for a wide range of nuclei, up to $z \sim 200$. So for small values of n, the replacement $ze \rightarrow ng\beta$ is justified.

As mentioned above, the correlated response of matter to a monopole's passage leads to corrections which are important for small ionization and dense media. A full treatment is provided by Ref. [10].

2.7 Multiple Scattering

The formula for multiple scattering of monopoles from the nuclei of atoms is deduced in a similar fashion. By exactly the same exercise as before—replacing the EM tensor for an electron with its dual—the monopole multiple scattering formula differs from

the electric equivalent only by the replacement $ze \to ng\beta$. For massive monopoles, the scattering angle is small, and multiple scattering is a small effect.

2.8 Çerenkov Radiation

Starting with the far fields of a moving charge [1] and applying the duality transformation, one obtains the far fields for a moving monopole. The Poynting vector, $(\vec{E} \times \vec{B})/4\pi$, in the two cases differs only by a substitution of electric with magnetic charge. There is no β factor because both the electric and magnetic fields are involved, not just the electric field as in the interactions considered above. For Çerenkov radiation, we merely replaces electric charge with magnetic charge ($ze \to ng$). We are again naively ignoring the correlated response of matter, which should lead to a correction, but massive monopoles are not relativistic enough to generate much Çerenkov Radiation, and the naive model is adequate.

Chapter 3

Tevatron and CDF Detector

Fermilab's Tevatron currently produces proton-antiproton ($p\overline{p}$) collisions at higher energies than any other experimental facility. It will remain on the energy frontier until experiments at the Large Hadron Collider (LHC) begin taking data in about 2007. The Tevatron collisions occur at two points on an underground ring, which has a radius of about one kilometer. At these collision points are two detectors: the Collider Detector at Fermilab (CDF) and D0. This analysis uses data collected by the CDF experiment.

Between 1997 and 2001, the accelerator complex underwent major upgrades aimed at increasing the luminosity of the accelerator to provide 2 fb^{-1} of integrated luminosity or more. The upgraded machine accelerates 36 bunches of protons and antiprotons, whereas the original machine accelerated 6 bunches. Consequently, the time between bunch crossings has been decreased from 3.5 μs to 396 ns.

The higher rate operation required major detector upgrades to ensure a fast enough response time. The new electronics is based on a 132 ns clock cycle; this is slightly faster than currently needed, a design choice to accommodate a now unlikely upgrade to an even higher number of bunches.

3.1 Tevatron

Fermilab uses a series of accelerators to produce the high energy $p\overline{p}$ collisions studied at CDF and D0 [11]. The paths taken by protons and antiprotons from initial acceleration to collision in the Tevatron are shown in Figure 3-1.

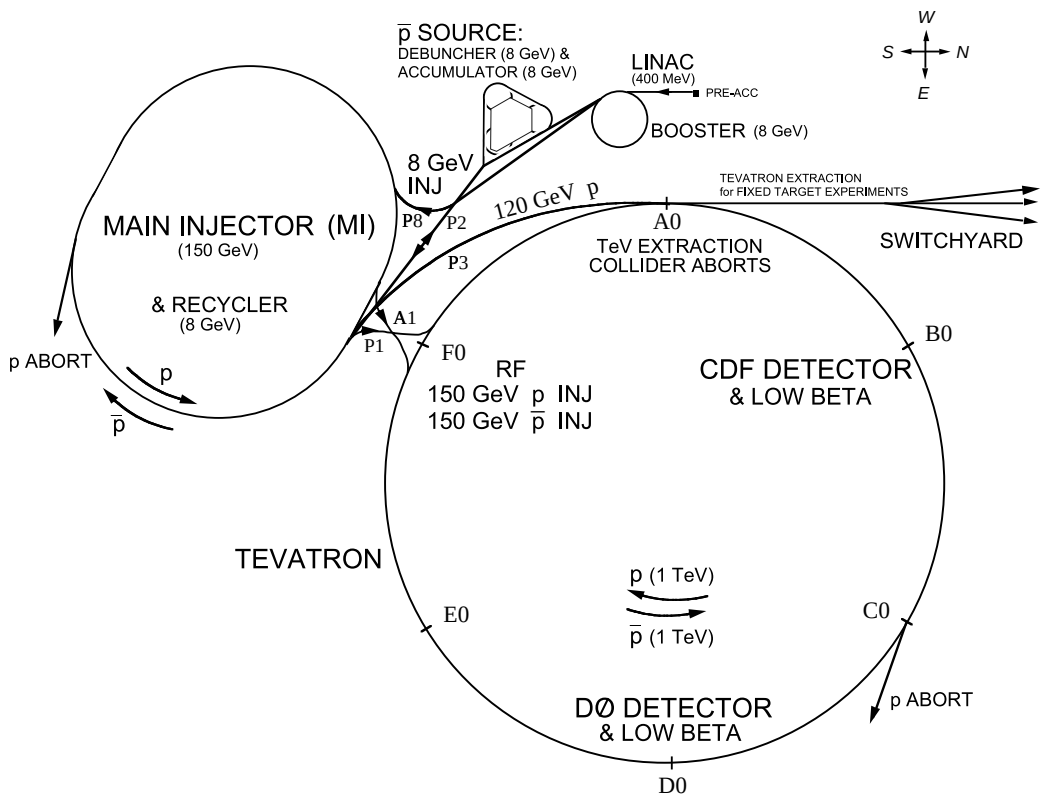

Figure 3-1: The Fermilab accelerator complex.

The Cockcroft-Walton pre-accelerator provides the first stage of acceleration [12]. Inside this device, hydrogen gas is ionized to create H^- ions, which are accelerated to 750 keV of kinetic energy. Next, the H^- ions enter a linear accelerator (Linac), approximately 500 feet long, where they are accelerated to 400 MeV [13]. An oscillating electric field in the Linac's RF cavities accelerates the ions and groups them into bunches. The ions moving too fast reach the cavity while the electric field is weak, while the ions moving too slow reach the cavity while the electric field is strong.

The 400 MeV H^- ions are then injected into the Booster, a circular synchrotron 74.5 m in diameter [13]. A carbon foil strips the electrons from the H^- ions at

injection, leaving bare protons. The intensity of the proton beam is increased by injecting new protons into the same orbit as the circulating ones. The protons are accelerated from 400 MeV to 8 GeV by another series of of RF cavities. Each turn around the Booster, the protons gain 500 keV of kinetic energy; but in the steady state, they lose exactly this much energy through radiation.

To produce antiprotons, protons from the Booster are accelerated to 120 GeV by the Main Injector and directed at a nickel target [11]. In the collisions, about 20 antiprotons are produced per one million protons, with a mean kinetic energy of 8 GeV. The antiprotons are focused by a lithium lens and separated from other particle species by a pulsed magnet. The Main Injector replaced the Main Ring accelerator which was situated in the Tevatron tunnel. The Injector is capable of containing larger proton currents than its predecessor, which results in a higher rate of antiproton production.

The RF cavities cannot constrain the antiprotons in the plane transverse to the beam direction. The collider requires narrow beams, so the transverse excursions of the antiprotons must be reduced. Since this process reduces the kinetic energy spread, it is referred to as "cooling" the beam. New batches of antiprotons are initially cooled in the Debuncher synchrotron, collected and further cooled using stochastic cooling [14] in the 8 GeV Accumulator synchrotron. Pickup sensors first sample the average transverse excursions for portions of each bunch. Later, kicker magnets apply correcting forces. This has the effect of damping the antiprotons on average, making a cool narrow beam. It takes between 10 and 20 hours to build up a "stack" of antiprotons which is then used for collisions in the Tevatron. Antiproton availability is most often the limiting factor for attaining high luminosities.

The stochastic cooling is done by the Antiproton Recycler [11], which is also intended to recycle antiprotons when the beam quality has gotten poor after many collisions. The Recycler cools the antiprotons and integrates them with a new stack.

Roughly once a day, stacks of protons and antiprotons are transferred to the Main Injector for acceleration to 150 GeV and injection into the Tevatron. The stacks contain 36 bunches, with a proton bunch containing around 3×10^{11} protons and an

antiproton bunch containing around 3×10^{10} antiprotons. There are more protons because they are more easily produced.

The Tevatron is the last stage of Fermilab's accelerator chain [11]. It receives 150 GeV protons and antiprotons from the Main Injector and accelerates them to 980 GeV. The protons and antiprotons circle the Tevatron in opposite directions. The beams are brought to collision at two "collision points", B0 and D0. The two collider detectors, the Collider Detector at Fermilab (CDF) and D0 are built around the collision points.

The luminosity of collisions is given by:

$$\mathcal{L} = \frac{f N_B N_p N_{\overline{p}}}{2\pi(\sigma_p^2 + \sigma_{\overline{p}}^2)} F\left(\frac{\sigma_l}{\beta^*}\right) \tag{3.1}$$

where f is the revolution frequency, N_B is the number of bunches, $N_{p/\overline{p}}$ are the number of protons/antiprotons per bunch, and $\sigma_{p/\overline{p}}$ are the root mean square (RMS) beam sizes at the interaction point. F is a form factor which corrects for the bunch shape and depends on the ratio of σ_l, the bunch length, to β^*, the beta function, at the interaction point. The beta function is a measure of the beam width.

Table 3.1 shows a comparison of Run I accelerator parameters with Run II design parameters [15]. Figure 3-2 shows peak luminosities during the Run II data taking.

Parameter	Run I	Run II
number of bunches (N_B)	6	36
bunch length [m]	0.6	0.37
bunch spacing [ns]	3500	396
protons per bunch (N_p)	2.3×10^{11}	2.7×10^{11}
antiprotons per bunch ($N_{\overline{p}}$)	5.5×10^{10}	3.0×10^{10}
total antiprotons	3.3×10^{11}	1.1×10^{12}
$\beta^*(cm)$	35	35
interactions per crossing	2.5	2.3
typical luminosity [$cm^{-2}s^{-1}$]	0.16×10^{31}	0.8×10^{32}
integrated luminosity [fb^{-1}]	0.12	4.4 by 2009
record luminosity [$cm^{-2}s^{-1}$]	—	1.1×10^{32}

Table 3.1: Accelerator parameters for Run I and Run II.

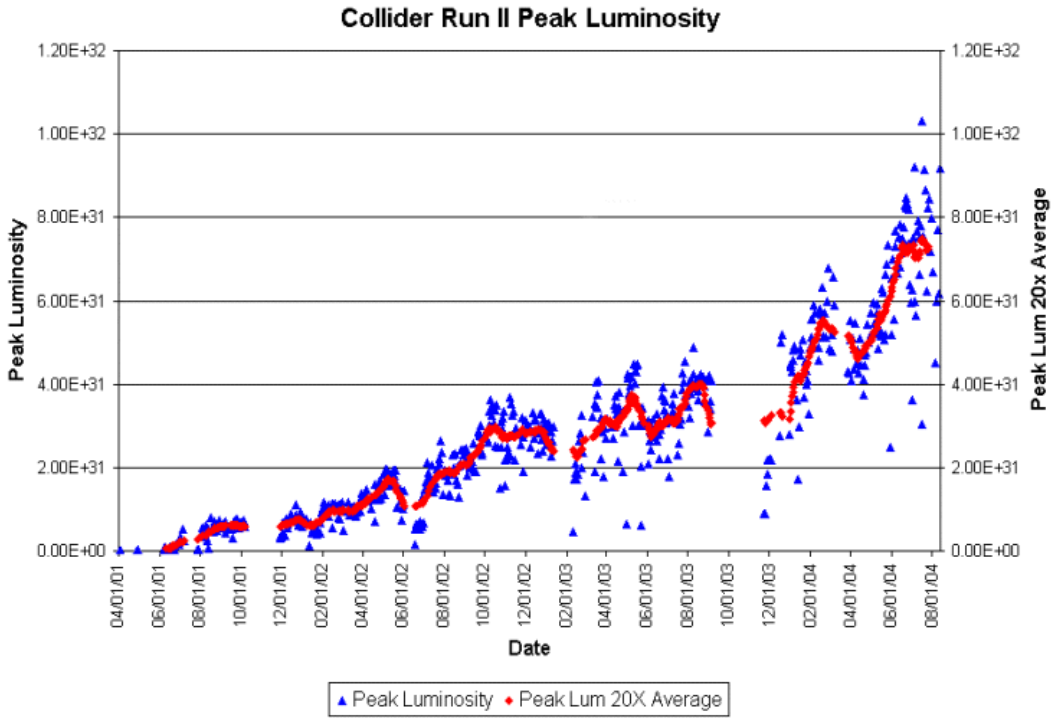

Figure 3-2: Peak instantaneous luminosity for Run II data taking.

3.2 The CDF Detector

The CDF detector [15] has been upgraded substantially from it's original version [16]. It is designed to detect particles created by $p\overline{p}$ collisions at the Tevatron's B0 interaction site and to measure their properties. It is a multipurpose detector, meaning the design is not aimed at one particular physics measurement, but rather at extracting generally useful information about the created particles.

A diagram of the CDF detector is shown in Figure 3-3. A quadrant of the detector is cut out to expose the different sub-detectors. The sub-detector systems are arranged around the beam-pipe, where the $p\overline{p}$ collisions occur. The beam-pipe is made of beryllium because this metal combines good mechanical qualities with a low nuclear-interaction cross-section.

The first system encountered by a typical particle traversing the CDF detector is the integrated tracking system. The tracking system is barrel-shaped and consists of cylindrical subsystems which are concentric with the beam. It is designed to detect charged particles and measure their momenta and displacements from the point of

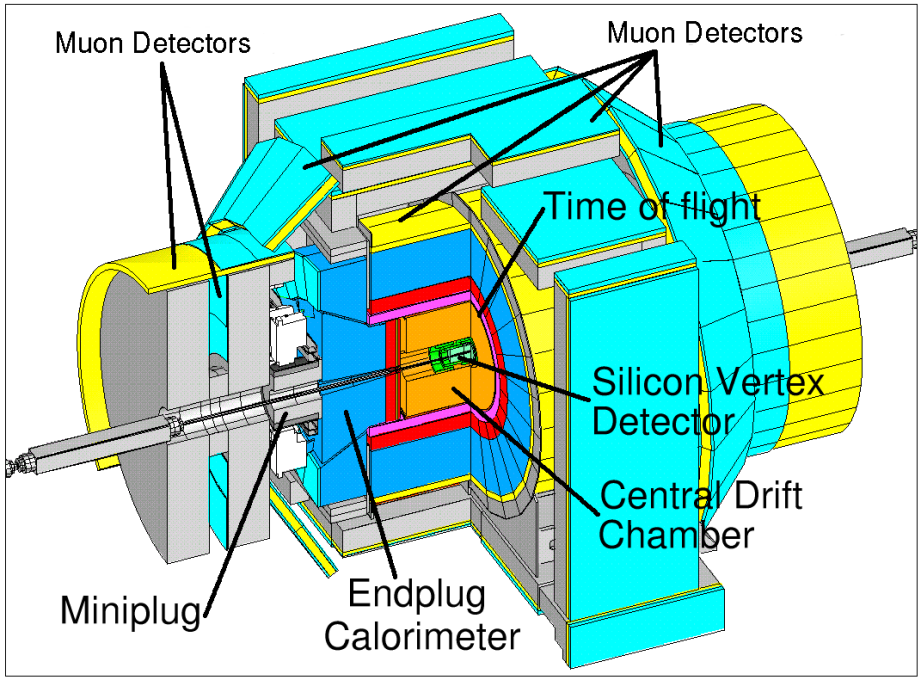

Figure 3-3: The CDF detector with a quadrant cut to expose the different sub-detectors.

collision, the primary interaction vertex.

The innermost tracking devices are silicon tracking detectors, which make precise position measurements of the path of a charged particle. A silicon tracking detector is a reverse biased p-n junction. When a charged particle passes through the detector material, it causes ionization. In the semiconductor material, electron-hole pairs are produced. Electrons drift toward the anode, and holes drift toward the cathode, where the charge is gathered. By segmenting the p or n side of the junction into "strips" and reading out the charge deposition separately on every strip, the position of the charged particle is measured.

A layer of silicon sensors, called Layer 00 (L00), is installed directly onto the beryllium beam-pipe, at an average radius of 1.7 cm from the beam [17]. Five concentric layers of silicon sensors (SVX) are located at radii between 2.5 and 10.6 cm [18]. The Intermediate Silicon Layers (ISL) consists of one layer at a radius of 22 cm in the central region and layers at radii 20 and 28 cm in the forward regions [19].

Surrounding the silicon detector is the Central Outer Tracker (COT), a 3.1-m-long

cylindrical open-cell drift chamber with inner and outer radii of 40 and 137 cm. The COT has axial and stereo layers to provide three-dimensional tracking information. The COT is the heart of CDF. Particles are usually first detected in the COT, then additional information from other detectors is added [20].

The next system encountered by a typical particle is the Time-of-Flight (TOF) system, designed to provide particle identification for low-momentum charged particles. TOF scintillator bars surround the COT in a barrel shape. The timing information from the TOF is combined with the momentum measurement from the COT to deduce a particle's mass [21].

Both the tracking and Time of Flight systems are placed inside a superconducting coil, which generates a 1.4 T solenoidal magnetic field. Upon leaving the coil, a typical particle encounters the calorimetry systems, which measure the energy of particles that shower when interacting with matter.

The CDF sampling calorimeter system [15] uses updated electronics to handle the faster bunch crossings, but the active detector parts were reused without modification. The calorimeter has a projective tower geometry; it is segmented in η and φ towers that point to the interaction region. The coverage of the calorimetry system is 2π in φ and $|\eta| < 4.2$ in pseudo-rapidity. The calorimeter system is divided into three regions from smallest $|\eta|$ to largest: central, plug and forward. Each calorimeter tower consists of an electromagnetic shower counter followed by a hadron calorimeter. This allows for comparison of the electromagnetic and hadronic energies deposited in each tower, and therefore separation of electrons and photons from hadrons.

The central calorimeters use scintillator as the active detector medium, while the plug and forward calorimeters use gas proportional chambers. The active medium of the electromagnetic calorimeters is alternated with lead sheets, while the hadron calorimeters use layers of iron.

The calorimetry systems are surrounded by muon detector systems. When interacting with matter, muons act as minimally ionizing particles; they only deposit small amounts of ionization energy in the material. They are the only particles likely to penetrate both the tracking and calorimeter systems, and leave tracks in the muon

detection system.

The CDF detector has four muon systems [22]: the Central Muon Detector (CMU), Central Muon Upgrade Detector (CMP), Central Muon Extension Detector (CMX), and the Intermediate Muon Detector (IMU). The CMU and CMP detectors are made of drift cells, and the CMX detector is made of drift cells and scintillation counters, which are used to reject background based on timing information. Using the timing information from the drift cells of the muon systems, short tracks (called "stubs") are reconstructed. Tracks reconstructed in the COT are extrapolated to the muon systems. Based on the projected track trajectory in the muon system, the estimated errors on the tracking parameters and the position of the muon stub, a χ^2 value of the track-stub match is computed. To ensure good quality of muons, an upper limit is placed on the value of χ^2_φ, the χ^2 of the track-stub match in the φ coordinate.

At the Tevatron, $p\overline{p}$ collisions happen at a rate of 2.5 MHz, and the readout of the full detector produces 250 kB of data. There is no medium available which is capable of recording data this quickly, nor would it be practical to analyze all of this data later on. CDF uses a deadtimeless trigger system to select the most interesting events for the data acquisition system to record.

In this analysis, we use only the Central Outer Tracker, the Time-of-Flight detector, and the global data acquisition and trigger system. These are described in greater detail below.

3.3 Standard Definitions at CDF

Because of the barrel-like detector shape, CDF uses a cylindrical coordinate system (r, φ, z) with the origin at the center of the detector and the z axis along the nominal direction of the proton beam. The y axis points upward. Since the coordinate system is right-handed, this also defines the direction of the x axis.

Electrically charged particles moving through a solenoidal magnetic field follow helical trajectories. Reconstructed particle trajectories are referred to as "tracks".

The plane perpendicular to the beam is referred to as the "transverse plane", and the transverse momentum of the track is referred to as p_{T}.

As opposed to e^+e^- collisions, in $p\overline{p}$ collisions, all of the center of mass energy of the $p\overline{p}$ system is not absorbed in the collision. The colliding partons inside the proton carry only a fraction of the kinetic energy of the proton. As a result, the center of mass system of the parton collisions is boosted along the beam direction (the "longitudinal" direction) by an unknown amount. Quantities defined in the transverse plane are conserved in the collisions. For instance, the sum of all transverse momenta of particles in the collisions is zero ($\sum \vec{p_{\mathrm{T}}} = 0$).

To uniquely parametrize a helix in three dimensions, five parameters are needed. The CDF coordinate system chooses three of these parameters to describe a position, and two more to describe the momentum vector at that position. The three parameters which describe a position describe the point of closest approach of the helix to the beam line. These parameters are d_0, φ_0, and z_0, which are the ρ, φ and z cylindrical coordinates of the point of closest approach of the helix to the beam. The momentum vector is described by the track curvature (C) and the angle of the momentum in the $r - z$ plane ($\cot\theta$). From the track curvature we can calculate the transverse momentum. The curvature is signed so that the charge of the particle matches the charge of the curvature. From $\cot\theta$, we can calculate $p_z = p_{\mathrm{T}} \times \cot\theta$. At any given point of the helix, the track momentum is a tangent to the helix. This means that the angle φ_0 implicitly defines the direction of the transverse momentum vector at the point of closest approach p_{T}.

The impact parameter (d_0) of a track is another signed variable; its absolute value corresponds to the distance of closest approach of the track to the beam-line. The sign of d_0 is taken to be that of $\hat{p} \times \hat{d} \cdot \hat{z}$, where $\hat{p}$, $\hat{d}$ and $\hat{z}$ are unit vectors in the direction of p_{T}, d_0 and z, respectively.

An alternate variable that describes the angle between the z axis and the momentum of the particle is pseudo-rapidity (η) which is defined as:

$$\eta \equiv -\ln\tan(\theta/2) \tag{3.2}$$

3.4 Central Outer Tracker (COT)

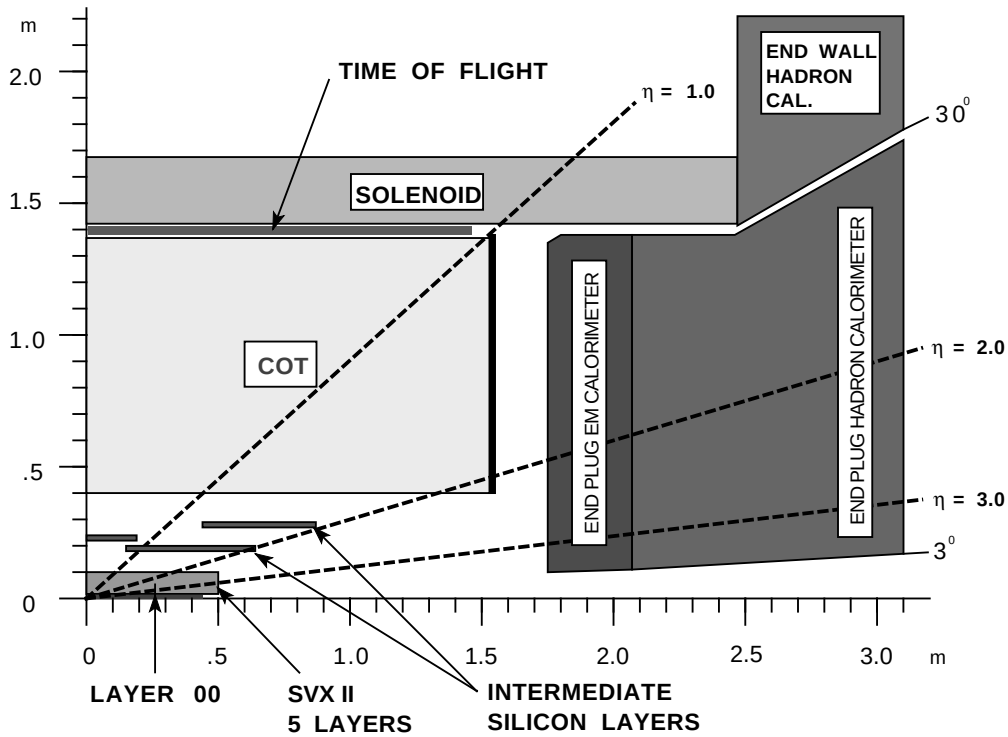

Figure 3-4: The CDF tracking sub-detectors.

The COT drift chamber provides accurate information in the $r - \varphi$ plane for the measurement of transverse momentum, and substantially less accurate information in the $r - z$ plane for the measurement of the z component of the momentum, p_z. The COT contains 96 sense wire layers, which are radially grouped into eight "super-layers", as inferred from the end plate section shown in Figure 3-5. Each super-layer is divided in φ into "super-cells", and each super-cell has 12 sense wires and a maximum drift distance that is approximately the same for all super-layers. Therefore, the number of super-cells in a given super-layer scales approximately with the radius of the super-layer. The entire COT contains 30,240 sense wires. Approximately half the wires run along the z direction, and are called axial wires. The other half are strung at a small angle (2°) with respect to the z direction, and are called stereo wires. The

small angle stereo wires resolve the z position of a track, making 3D tracking possible.

The active volume of the COT begins at a radius of 43 cm from the nominal beam-line and extends out to a radius of 133 cm. The chamber is 310 cm long. Particles originating from the interaction point which have $|\eta| < 1$ pass through all 8 super-layers of the COT. Particles which have $|\eta| < 1.3$ pass through 4 or more super-layers. This is a slight simplification; the true acceptance depends on the primary vertex position.

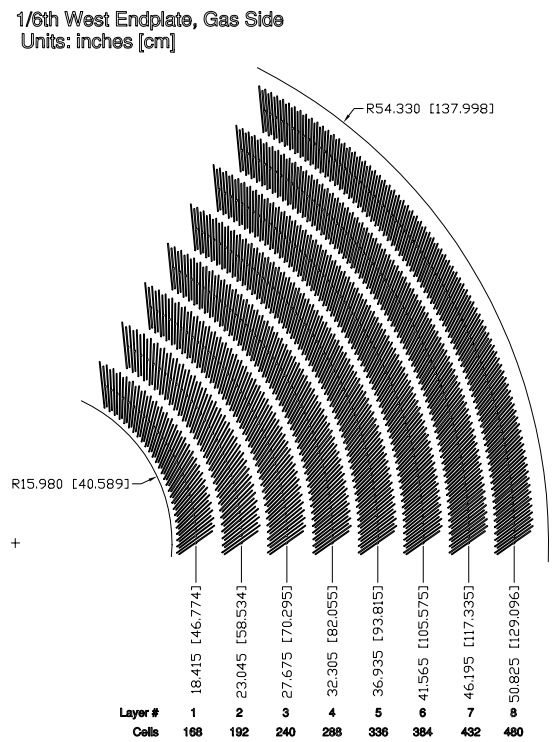

Figure 3-5: The wire planes on a COT end-plate.

The super-cell layout, shown in Figure 3-6 for super-layer 2, consists of a wire plane containing sense and potential (for field shaping) wires and a field (or cathode) sheet on either side. Both the sense and potential wires are 40 μm diameter gold plated Tungsten. The field sheet is 6.35 μm thick Mylar with vapor-deposited gold on both sides. Each field sheet is shared with the neighboring super-cell.

The COT is filled with an Argon-Ethane-CF4 (50:35:15) gas mixture. The mixture is chosen to have a constant drift velocity across the cell width. When a charged particle passes through, the gas is ionized. Electrons drift toward the sense wires.

The electric field in a cylindrical system grows exponentially with decreasing radius. As a result, the electric field very close to the sense wire is large, resulting in an avalanche discharge when the charge drifts close to the wire surface. This effect provides a gain of $\sim 10^4$. The maximum electron drift time is approximately 100 ns. Due to the magnetic field that the COT is immersed in, electrons drift at a Lorentz angle of $\sim 35°$. The super-cell is tilted by 35° with respect to the radial direction to compensate for this effect.

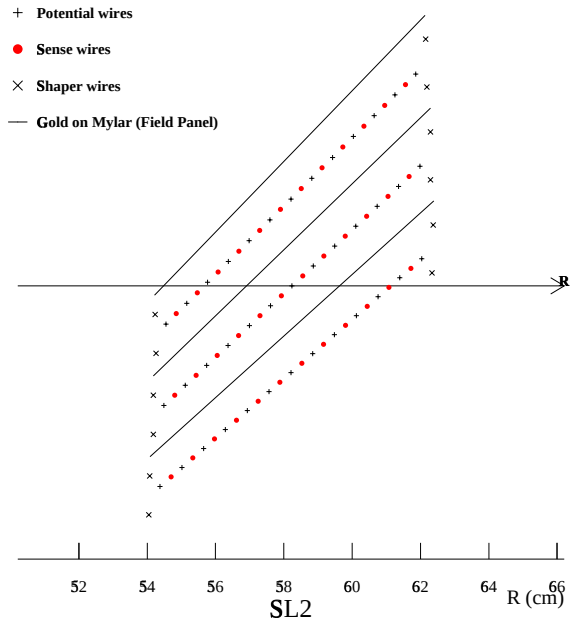

Figure 3-6: The wire layout in a COT super-cell. Here super-layer 2 is depicted.

Signals on the sense wires are processed by the ASDQ (Amplifier, Shaper, Discriminator with charge encoding) chip, which provides input protection, amplification, pulse shaping, baseline restoration, discrimination and charge measurement [23]. The charge measurement is encoded in the width of the discriminator output pulse, and is used for particle identification by measuring the ionization along the trail of the charge particle (dE/dx). The pulse is sent through $\sim$ 35 ft of micro-coaxial cable, via repeater cards to time-to-digital converter (TDC) boards in the collision hall.

Charged particles leave small charge depositions as they pass through the tracking system. By following, or "tracking" these depositions, pattern recognition algorithms

reconstruct the charged particle track.

There are several pattern recognition algorithms used to reconstruct tracks in the CDF tracking system. Most of the tracks are reconstructed using "Outside-In" algorithms which follow the track from outside of the tracking system inward. This is because the occupancy is much higher toward the center of the detector, making pattern recognition more difficult.

The track is first reconstructed using only COT information. The COT electronics report the hit time and integrated charge for every wire in an event. The hit time is the time that an avalanche occurred at a sense wire. The hit time minus the time of flight is the drift time of the charge in the gas. The time of flight is calculated assuming the particles travel at the speed of light.

The helical track, when projected into the two dimensional $r - \varphi$ plane, is a circle. This simplifies pattern recognition, so the first step of pattern recognition in the COT looks for circular paths in axial super-layers of the COT. Super-cells in the axial super-layers are searched for sets of 4 or more hits that fit to a straight line. These sets are called "segments". The straight-line fit for a segment gives sufficient information to extrapolate rough measurements of curvature and φ_0. Once segments are found, they must be linked together to form tracks. One approach is to link together segments for which the measurements of curvature and φ_0 are consistent. However, higher occupancy toward the innermost super-layers can cause this approach to fail. Another approach is to improve the curvature and φ_0 measurement of a segment reconstructed in super-layer 8 by constraining its circular fit to the beam-line, and then adding hits which are consistent with this path. Once a circular path is found in the $r - \varphi$ plane, segments and hits in the stereo super-layers are added by their proximity to the circular fit. This results in a three-dimensional track fit.

Combined, these two approaches have a high track reconstruction efficiency ($\sim$ 95%) for tracks which pass through all 8 super-layers ($p_{\mathrm{T}} \geq 400$ MeV$/rmc^2$). The track reconstruction efficiency mostly depends on the local density of tracks. If there are many tracks close to each other, hits from one track can shadow hits from the other track, resulting in efficiency loss.

Once a track is reconstructed in the COT, it is extrapolated into the SVX. Based on the estimated errors on the track parameters, a three-dimensional "road" is formed around the extrapolated track. Starting from the outermost layer, and working inward, silicon clusters found inside the road are added to the track. As a cluster gets added, the road gets narrowed according to the knowledge of the updated track parameters. Reducing the width of the road reduces the chance of adding a wrong hit to the track, and also reduces computation time. In the first pass of this algorithm, $r - \varphi$ clusters are added. In the second pass, clusters with stereo information are added to the track.

3.5 Time of Flight

The CDF Time-of-Flight (TOF) system is located just outside the COT, inside the superconducting magnetic coil, as in Figure 3-4. The TOF is designed to distinguish low-momentum pions, kaons and protons by measuring the time it takes these particles to reach the TOF from the primary vertex. The particle momentum is known from the tracking system, the time-of-flight measurement therefore provides an indirect measurement of the mass [21].

The TOF is composed of 216 bars of Saint-Gobain (formerly Bicron) BC-408 blue-emitting plastic scintillator, forming an annulus 300 cm long with a radius of 144 cm. The bars have a slightly trapezoidal shape to accommodate the annulus shape, with an approximate width and height of 4 cm.

When fast moving charged particles pass through the scintillator bars, they excite the atoms in the plastic through ionization energy-loss. The excited atoms lose part of this energy by emitting photons of light. Good scintillator materials are characterized by short relaxation times and low attenuation of the generated light.

The scintillator light is converted to a signal voltage by Hamamatsu R5946mod 19-stage fine-mesh photo-multiplier tubes (PMTs) installed on both ends of the scintillator bars. The 19-stage high-gain design is needed to ensure adequate gain inside CDF's 1.4 T magnetic field. The photo-multiplier tubes are followed by dual-range

pre-amplifiers before transmission to the readout electronics over shielded twisted pair cables. The dual range increases the dynamic range of the TOF electronics for the magnetic monopole search without adversely effecting the performance for ordinary particles. An initial high-gain region for ordinary tracks is followed by a second low-gain region for larger pulses.

The digitization of the pre-amplified PMT pulses is performed by TOF Transition (TOMAIN) and ADC/Memory (ADMEM) boards. The TOMAIN boards begin ramping an output voltage as soon as the pulse exceeds a threshold, and stop ramping at a common stop signal. The output voltage is digitized by the ADMEMs. Because a large pulse will go above threshold faster than a small pulse, an integrated charge measurement is needed to correct this time-walk effect. The TOMAIN boards integrate the charge for a fixed time interval (20 ns for the data in this analysis) after the pulse goes above threshold, then convert the integrated charge to an output current, which is digitized by the ADMEM. The integrated charge measurement is the basis for the TOF highly ionizing particle trigger, used for the monopole search [26].

The timing resolution of the TOF system is about 110 ps for particles crossing the bar exactly in front of one of the photomultiplier tubes. Because light is attenuated in the bar, the timing resolution is worse for tracks crossing far from a PMT.

3.6 The CDF Trigger

Each second, the CDF deadtimeless trigger decides which 50 of 2.5 million events to write to tape. It accomplishes this with a three tiered system, as shown in Figure 3-7, with each level given more time to make a more precise decision. The Level 1 and Level 2 decision are made entirely on fast custom electronics. The Level 3 decision is made with software on off-the-shelf PCs.

After digitizing an event, each sub-detector's front end readout cards store the event data in a digital pipeline. For every 132 ns Tevatron clock cycle, the event is moved up one slot in the pipeline. A small sub-set of the data follows an alternate path to custom electronics, where a Level 1 trigger decision is made. Physics triggers

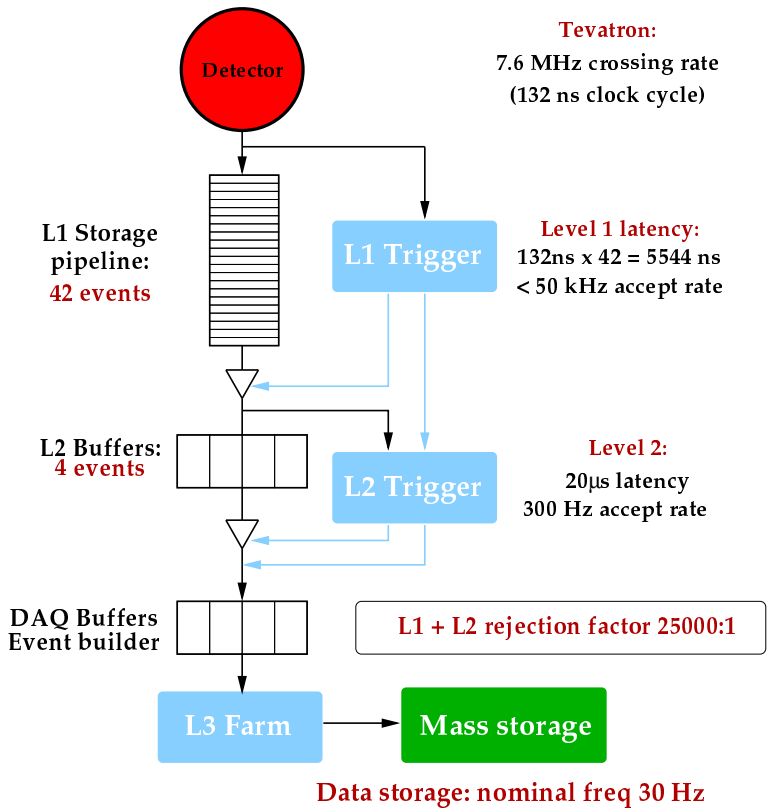

Figure 3-7: The CDF trigger.

are combined into a global Level 1 decision, which is sent back to the front end crates just as the event is emerging from the end of the Level 1 pipeline. The decision arrives 42 events after the event, but because sub-detectors have different intrinsic delays due to cable lengths and other effects, the pipeline length is adjusted to ensure synchronization.

Upon a Level 1 accept, the data for the event is sent to one of four Level 2 buffers, buying additional time for the Level 2 decision. Like the Level 1 pipeline, the Level 2 buffers are implemented in each sub-detector's front-end readout cards. Some additional information from the front-end cards is included in the Level 2 decision, which must be made quickly enough to clear out buffers for additional Level 1 accepts.

Upon a Level 2 accept, the Level 2 buffer is readout from each front end crate, and assembled by the event builder into a complete event. The event is sent to one of 300 Level 3 PCs, where a final software trigger decision is made. At this stage, nearly full event reconstruction is possible.

The Level 1 pipeline has 42 slots, allowing 5 μs for the trigger decision. The rejection factor is about 150, so the Level 1 accept rate is below 50 kHz. At Level 2, there are 4 buffers available, allowing 20 μs for the trigger decision. The Level 2 rejection factor is an addition 150, making the accept rate about 300 Hz. The Level 3 rejection rate is about 10, resulting in 30 events per second written to tape.

Much of the interesting physics at CDF is contained in the trigger. The ability to tag events with displaced vertices, for instance, provides an excellent B-physics sample. The magnetic monopole search uses a custom Level 1 trigger to require high ionization.

Chapter 4

Time-of-Flight Trigger

The Time-of-Flight (TOF) trigger provides three Level 1 triggers using the integrated charge measurement of photomultiplier tube (PMT) pulses, which is primarily intended to correct discriminator threshold effects on the time measurement. The highly ionizing particle (HIP) trigger checks for abnormally large pulses caused by particles such as magnetic monopoles. The minimum ionizing particle (MIP) multiplicity trigger requires that the total number of normal sized pulses is within a specified range. The TOF cosmic trigger requires two nearly back to back hits in the TOF system [24].

An overview of the TOF trigger hardware is presented in Figure 4-1, and the crate locations are listed in Table A.1. The TOF scintillators form a cylinder around the tracking region; each 15° wedge contains nine TOF scintillator bars. The bars are instrumented on both ends with PMTs and dual-range pre-amplifiers. The pre-amplifiers make the PMT signal more robust for transmission and extend the dynamic range. An initial linear region at high gain is followed by a short non-linear transition region, then a second linear region at lower gain. The high-gain region is intended for typical pulses from ordinary particles, the second low-gain region is to avoid saturation for highly ionizing particles [21, 25, 26, 27].

The digitization of the pre-amplified PMT pulses is done by TOF Transition (TOMAIN) and ADC/Memory (ADMEM) boards. Field Programmable Gate Arrays (FPGAs) in the ADMEMs set trigger bits for pulse heights larger than MIP and HIP

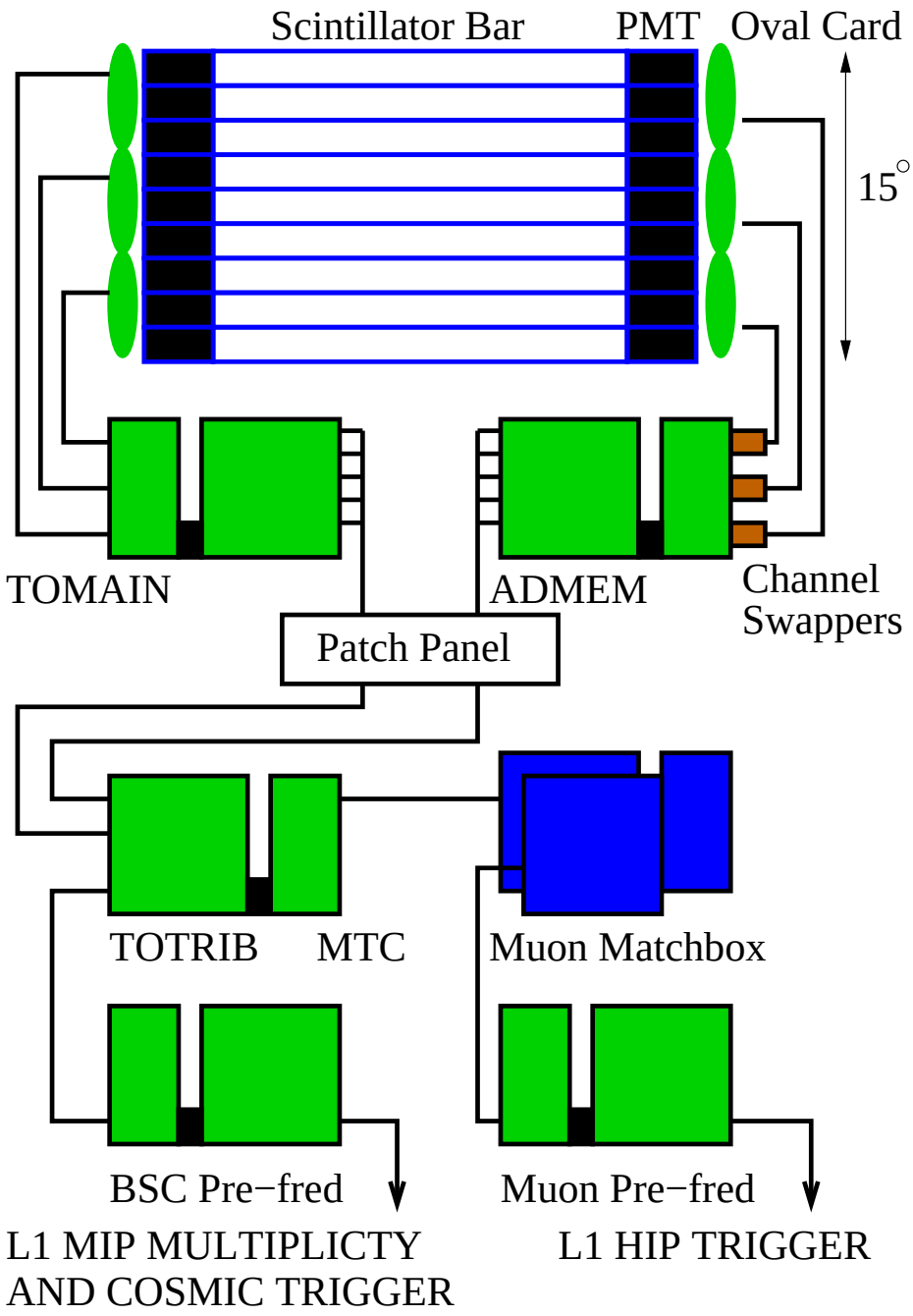

Figure 4-1: The TOF trigger electronics for a 15° wedge.

thresholds.

Additional logic is performed by the special purpose TOF trigger board (TOTRIB), which collects data from TOF ADMEMs and checks for coincidences of pulses above HIP and MIP thresholds on both the east and west sides of TOF scintillator bars. The full coincidence data has five bits per nine TOF scintillator bars, but by combining multiple channels, coincidences are calculated at coarser granularity for Level 1 track matching and the TOF cosmic trigger. The TOTRIB also counts the number of MIP coincidences.

HIP east-west coincidences from the TOTRIB are matched to rapidly reconstructed drift chamber tracks using extra channels in the muon trigger system. The high density of inputs to the muon trigger requires the use of serial fiber optic links, prepared by Muon Transition Cards (MTCs). The TOTRIB simplifies the muon match card (Matchbox) programming by providing coincidence data at the same granularity as the extrapolation (four bits per 30°).

At present luminosities, some features of the HIP trigger are not needed to control the rate. The extrapolation bits are always high, to always satisfy the track matching requirement. This means that any HIP coincidence causes the trigger to fire. Also, although the muon match cards report the full coincidence data to the global Level 2 trigger, no special Level 2 trigger is needed. A Level 1 TOF HIP trigger causes an automatic Level 2 and Level 3 accept.

At CDF, each trigger component uses specially programmed Level 1 interface cards, called PreFRED cards, to set the global Level 1 trigger bits appropriately. Because the TOF HIP trigger uses the muon system, the TOF HIP trigger bit is set by the Muon PreFRED. The two TOF MIP triggers use extra channels in the Beam Shower Counter (BSC) PreFRED.

4.1 TOMAIN and TOF ADMEMs

The signal from TOF PMTs is digitized on ADC/Memory (ADMEM) modules. The ADMEM's versatile design is used on various detectors at CDF, mainly calorimetry.

In order to work for TOF, a specially designed transition card (TOMAIN) performs analog services on the PMT signals: converting the time interval between the PMT pulse arrival time and a common stop to an output voltage, and converting the integrated charge of the PMT pulse into an output current pulse.

4.1.1 Technical Description

On the ADMEM, the current pulse digitization is normally made using the ADC cards (Cafe cards). The measurement is made with 10-bit precision, with additional range information making a wide 17-bit dynamic range after linearization. This precision is adequate for the TOF charge measurement, but not for the timing measurement, and so a replacement card is needed. Because the replacement ADC requires neither the wide dynamic range nor linearization features of the Cafe card, it is called the Decaf card.

The ADMEM receives the analog output signals from the TOMAIN card through the J3 connector of the VME backplane, as depicted in Figure 4-2. Digitized charge measurements from the Cafe cards, and time from the Decaf cards, are sent to FPGAs on the ADMEM which hold the results in the Level 1 pipeline awaiting a Level 1 accept, and Level 2 buffers awaiting a Level 2 accept. The ADMEM contains 5 FPGAs for this purpose, each handling 4 input channels. In TOF ADMEMs, each FPGA handles two charge and two time measurements, except the last FPGA, which handles a single charge and time measurement, because the TOF uses only 18 of 20 ADMEM channels.

These FPGAs also perform trigger logic. Because the TOF trigger logic is different from the calorimeter trigger logic, new firmware was written to check whether the two charge measurements are greater than adjustable HIP or MIP thresholds [28]. To limit costs, a single HIP output bit is set if either of the charge measurements exceeded its HIP threshold, and likewise for the single MIP output bit. The logical `OR` is implemented in the ADMEMs trigger lookup table, as shown in Table 4.1.

It is desirable to change the firmware for the L1/L2/trigger FPGAs, but not the VME firmware. However, the trigger firmware requires two MIP and two HIP

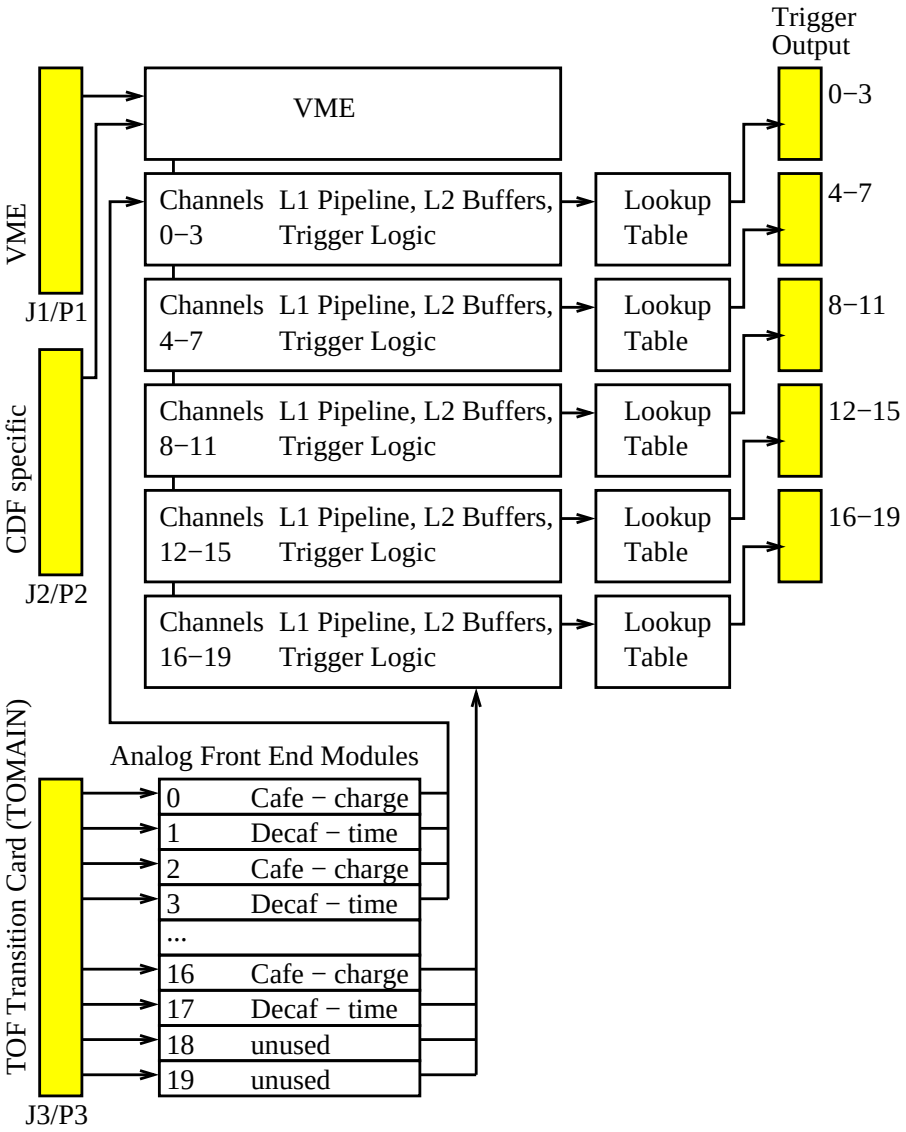

Figure 4-2: A block schematic of the TOF ADMEM. The ADMEM has many features not essential to the trigger, which have been omitted from this diagram.

input				output	
HIP1	HIP2	MIP1	MIP2	HIP	MIP
0	0	0	0	0	0
0	0	0	1	0	1
0	0	1	0	0	1
0	0	1	1	0	1
0	1	0	1	1	1
0	1	1	1	1	1
1	0	1	0	1	1
1	0	1	1	1	1
1	1	1	1	1	1

Table 4.1: The TOF ADMEM trigger lookup table is a logical `OR`. It is impossible to have HIP on and MIP off.

thresholds per FPGA, which need to be easily set through the VME interface. This was accomplished by co-opting the usual pedestal register for each trigger FPGA; the pedestal register VME addresses are listed in Table A.2. The new trigger FPGA keeps a stack of 5 registers—interpreted as four thresholds and the pedestal—pushing a value in from the right with each write to the pedestal address. The TOF ADMEM driver merely writes the thresholds to the same address in order. We choose to absorb the pedestal into the threshold and set the pedestal register to zero.

4.1.2 Channel Swappers

The TOF signal cables group TOF scintillators in threes, and the same cables are used on the east and west side of the detector, which introduces an unintended channel swap on the east side of the CDF detector, as illustrated in Fig 4-3. To correct this problem, we produced very small 9-pin to 9-pin adapter, called channel swappers, and installed them between the signal cables and the TOMAIN boards. Because this is part of the signal path, we took great care to check that the adapters do not degrade the signal. It is amusing that the TOF cable length calibration measures a systematic timing difference of a few centimeters between the east and west.

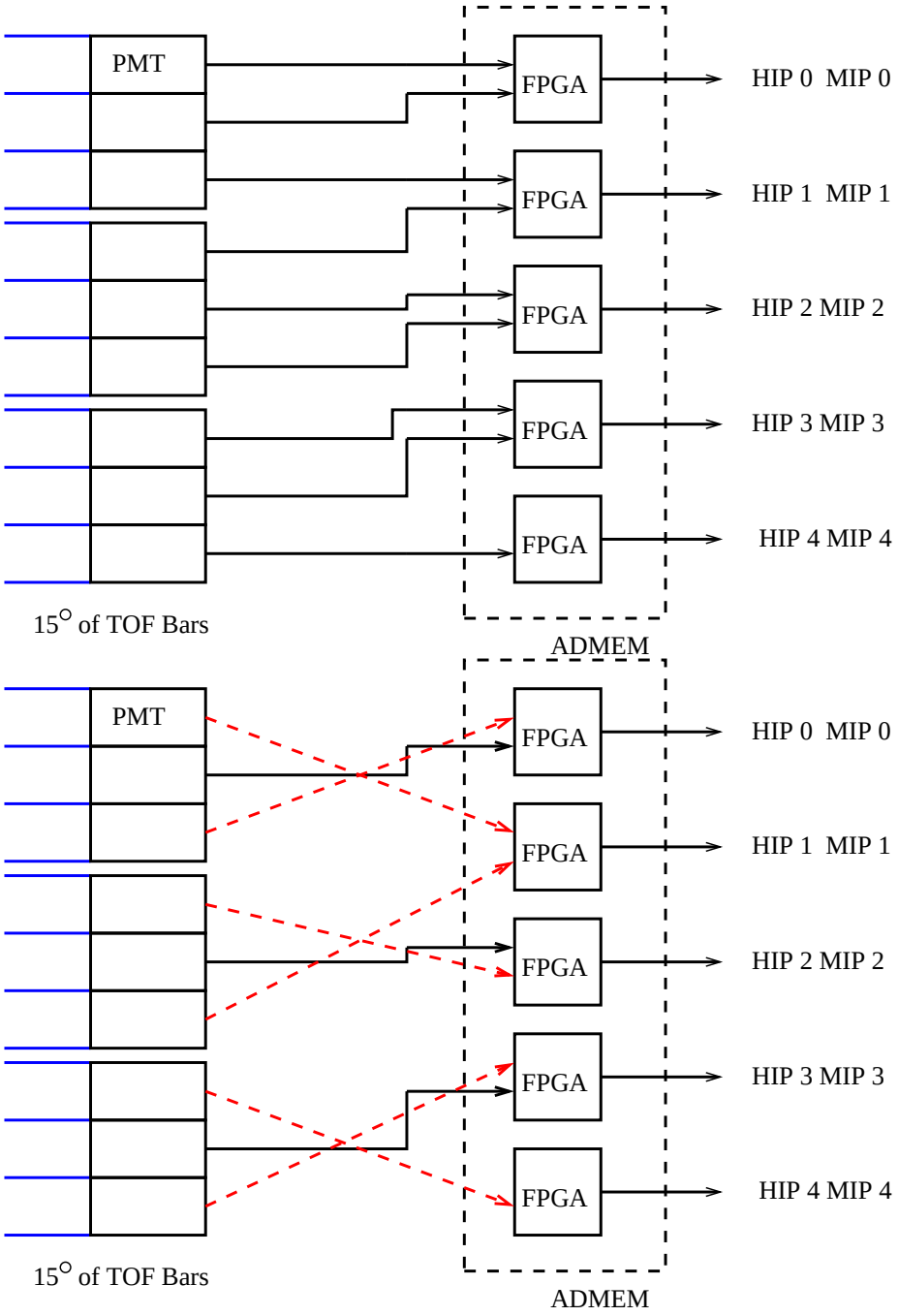

Figure 4-3: The TOF signal cables group TOF scintillators in threes, and the same cables are used on the east and west side of the detector, which introduces an unintended channel swap on the east side of the CDF detector.

4.1.3 Software

In order to properly configure the TOF ADMEMs for the TOF trigger, the Front End Readout (FER) code was slightly modified. Each crate reads the HIP and MIP calibration constants from a file located at
`/cdf/code-common/cdfonline/tof/trigger/config/admem`
on the online cluster. Eventually, these will be read from the calibration database, but this has not yet been implemented. Each channel's trigger thresholds is obtained from the trigger table global threshold as:

$$Q_i = A_i + B_i * Q_{global}.$$

These thresholds are then sent to the corresponding ADMEM FPGA as already discussed. At present, we ignore Q_{global} by setting B_i to zero, and use A_i to set the HIP and MIP thresholds (there are separate calibration constants for HIP and MIP.) This is because it is much easier to change a calibration table then a trigger table.

For maintenance, the ADMEM menu driven tool "Qietest" was modified to include features needed for the TOF ADMEMs. In the Level 1 trigger menu, shown in Figure 4-4, a new ADMEM type, 10, corresponds to TOF ADMEMs. When this ADMEM type is selected, choosing option 3 causes the TOF firmware to be downloaded to the L1/L2/trigger FPGAs. Choosing option 4 causes Table 4.1 to be written to the trigger look-up table.

During the commissioning, additional ADMEM driver code was written to fill the ADMEMs diagnostic buffer with any desired pattern. One particularly useful pattern outputs all ones on the B0 event and zeros otherwise. This was essential for timing in the trigger. There is additional code for dumping the L2 buffers, cold starting, or printing the current configuration, all from the command line. All the code is located on the online machines in the directory
`/cdf/code-common/cdfonline/tof/trigger/code/admem`.
It is essential to have command line code to check what is going on in real time;

```
*****************  L1 trigger Menu   ************************
*         OPTIONS                          Current Setting
* 1.  ADMEM type (CEM=0,PEM=1,WHA=2,                0
*                 CHA=3,PHA=4,Unit Weight=5,
*                 BSC-1=6,BSC-2=7,ADMEM-1=8,ADMEM-2=9,TOF=10)
* 2.  Directory of the S_record files
*        /cdf/code-common/cdfonline/fer/current/src/qietest/
* 3.  Configure ADMEMs (FPGA)
* 4.  Down load Et look-up table
* 5.  TSCR(Trigger Sum Cable Receiver)             14
* 6.  Checking
* 7.  Pedestal registers                           50
* 8.  CAFE data input (0=DCcal,1=Ext.)             0
* 9.  Number of events                             10
*10.  DAC range                                    0-100
*11.  Step of DAC changing                         10
*12.  Select QIE                                   0-19
*13.  Select TSCR channels                         0-7
*14.  ADMEM                                        5
*15.  File Name(to save the checking results)
*        /data1/cdf_cal/trigger.dat
*16.  Identify ADMEMs
*17.  Trigger Algorithm version                    19DEC01
*18.  Print ADMEM version tags
* Q.  Back
option ->
```

Figure 4-4: The Level 1 trigger menu from the ADMEM utility program Qietest.

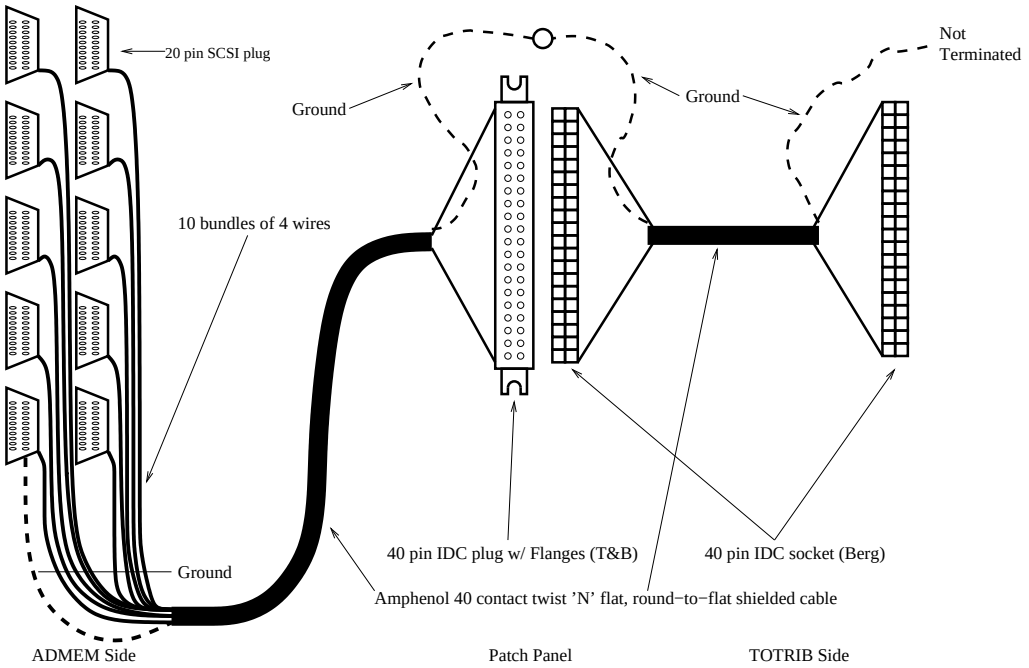

Figure 4-5: The TOF trigger cables are driven at the ADMEM side by 10 connectors shared by two ADMEMs. To avoid ground loops, the cable shield is connected to the housing of only one of the ten connectors. At the patch panel, the mass terminated cable is connected to an outgoing TOTRIB side cable. Each TOTRIB accepts six trigger cables.

otherwise one would have to wait for a run to finish and data to become available for each test.

4.2 Trigger Cables and Patch Panel

The ADMEMs are located in crates mounted on the east and west sides of the CDF detector, while the TOTRIBs are located in the first floor counting room. Because the TOF trigger was added after the CDF detector was moved into the collision hall, the usual movable cable tray–which allows cables to remain attached to the detector while it moves in and out of the collision hall—was not accessible. Instead, we installed a patch panel in the top north west corner of the detector. Cables run from the ADMEMs along the detector to the patch panel, then from the patch panel to the ceiling and up to the first floor counting room. When the detector moves, the cables

will have to be detached at the patch panel.

Each of the five trigger FPGAs on the ADMEM has a separate output, but the TOF trigger uses only two channels from each output. For this reason, we decided to use one trigger cable for every two ADMEMs. Each cable has 10 20-pin SCSI connectors on the ADMEM side, but only 4 pins from each connector is connected to the cable, as illustrated in Fig. 4-5. These are connected to an Amphenol 40 contact twist-n-flat round-to-flat cable. On the other side, a 40 pin Berg IDC plug is permanently installed in the patch panel using the built in flanges. The cables that run from the patch-panel to the TOTRIB use the same cable terminated by Berg IDC sockets on both sides.

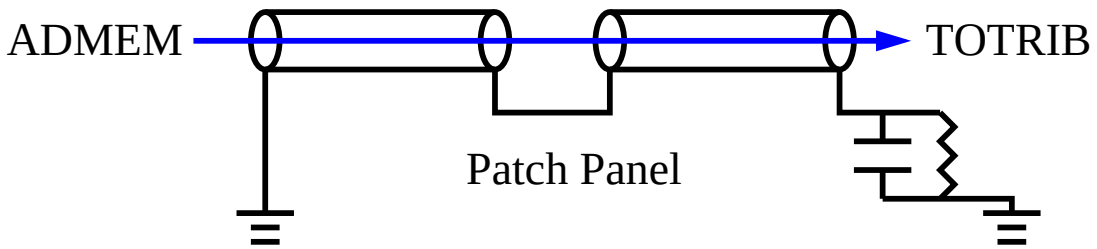

Figure 4-6: The TOF trigger cable shield is grounded at the ADMEM side (driving end). The shield of corresponding cables are connected at the patch panel but kept isolated from other pairs. At the receiving end, the shield is connected to ground by a resistor and capacitor, or left isolated.

To prevent ground loops, the shield of the cable is grounded to the first ADMEM only. At the patch panel the shield of each incoming wire is connected to the corresponding outgoing shield, but isolated from other pairs. At the receiving end, the TOTRIB isolates the shield from each of the six input cables. We have found that the noise Level is low with the shield left floating on the receiving end, but if noise becomes a problem, there is space on the TOTRIB to install a resistor and capacitor between the cable shield and ground, as in Figure 4-6.

4.3 TOTRIB

The TOF ADMEMs check for pulses in the TOF PMTs larger than HIP and MIP thresholds. To perform additional trigger logic, special purpose TOF trigger boards (TOTRIBs) are used. The TOTRIB collects data from east and west ADMEMs and checks for coincidences of HIP and MIP hits. The full coincidence data is at a resolution of a few bars, but by combining multiple channels, coincidences are calculated at coarser scales for Level 1 track matching and the TOF cosmic trigger. The TOTRIB also sums the number of MIP coincidences.

4.3.1 Technical Description

The TOTRIB is a 9U single wide VME board, as illustrated in Fig. 4-7. Low Voltage Differential Signaling (LVDS) [29] input is taken from front panel connectors (A0-2, B0-2) and received on three coincident unit FPGAs where the trigger logic is performed, as shown in Figure 4-8. Each FPGA performs a bitwise AND on its corresponding east and west data to obtain the coincidence data. Coarser granularity data is calculated by performing appropriate bitwise ORs as defined in Section 4.3.3.

To calculate the MIP sum, each FPGA calculates a partial sum for its share of the data and the partial sums are added on the central FPGA. This is accomplished using the same firmware on all three FPGAs by providing the outer two FPGAs with logical input sums that are permanently set to zero. The outer FPGAs send their output sums to the inner FPGA, which sends its output sum to the front panel (B3) in LVDS.

The MIP sum and scatter pattern are sent to the BSC PreFRED card for creating the MIP multiplicity and cosmic trigger. Because this PreFRED is shared by several systems and has limited capacity to delay inputs, the TOTRIB delays the MIP output on the front panel from one to 256 clock cycles; five clock cycles is the current setting.

The TOTRIB sends the HIP and MIP coincidence data to the Muon Transition Card in Transistor-Transistor Logic (TTL) format through the backplane J3 connector. It is sent on the clock cycle immediately after the data is latched. To ensure that

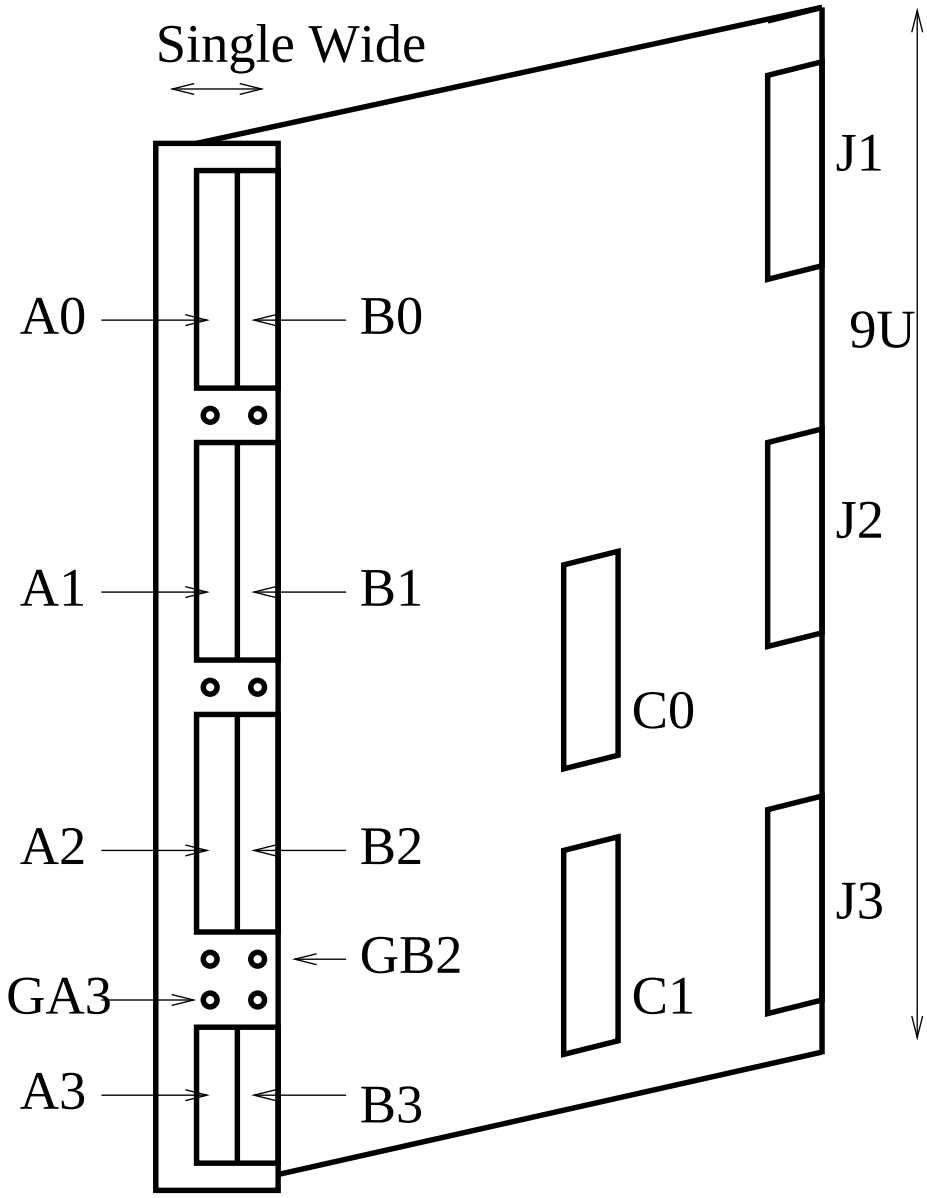

Figure 4-7: The TOTRIB's front panel has room for 6 input connectors (A0, B0, A1, B1, A2 and B2), enough to handle the trigger bits sent by ADMEMs from 90° of the detector. The 2 front panel outputs (A3 and B3) provide the MIP output. For future flexibility, addition connectors (C0 and C1) are mounted to the board behind the front-panel.

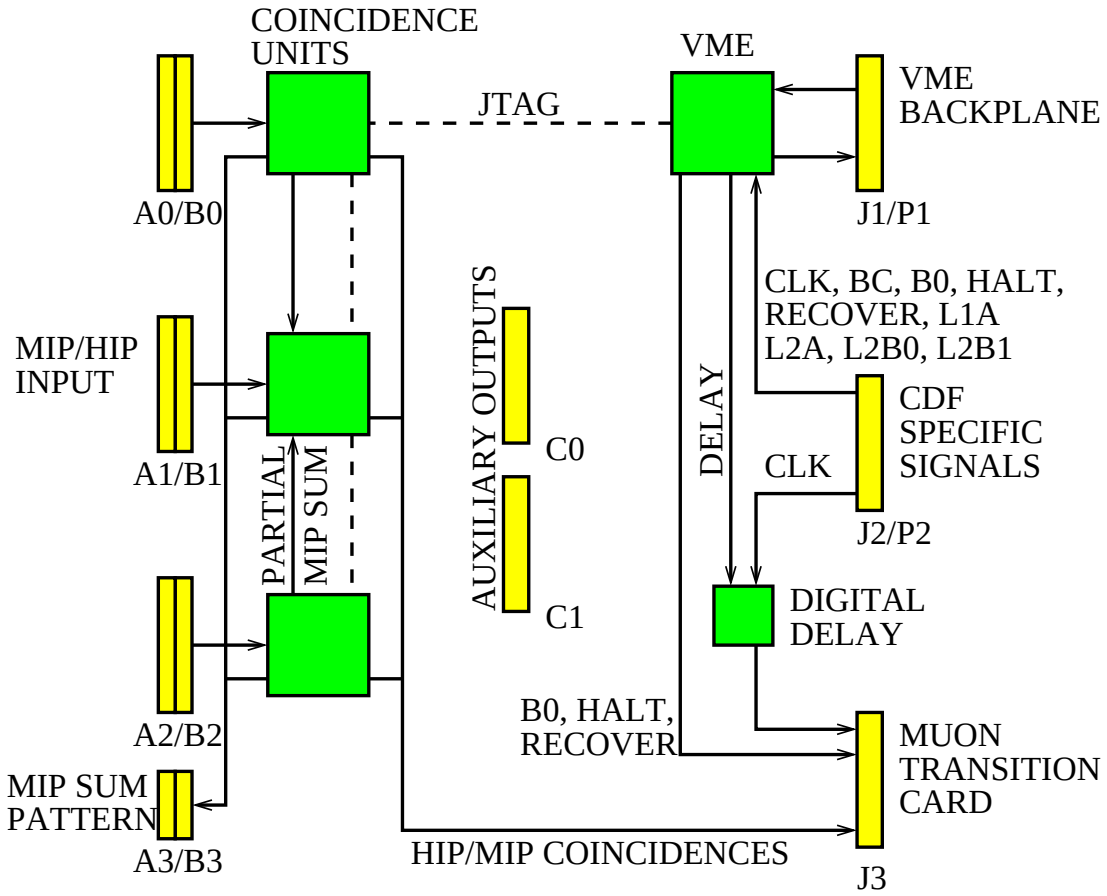

Figure 4-8: A block schematic of the TOTRIB. There are three coincidence unit FPGAs which perform the trigger logic, and an additional FPGA for VME services.

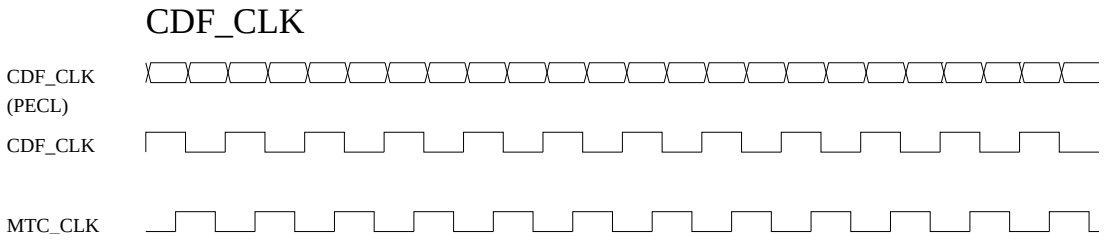

Figure 4-9: The TOTRIB converts the CDF clock taken from the VME backplane from PECL to TTL and adds a programmable phase delay.

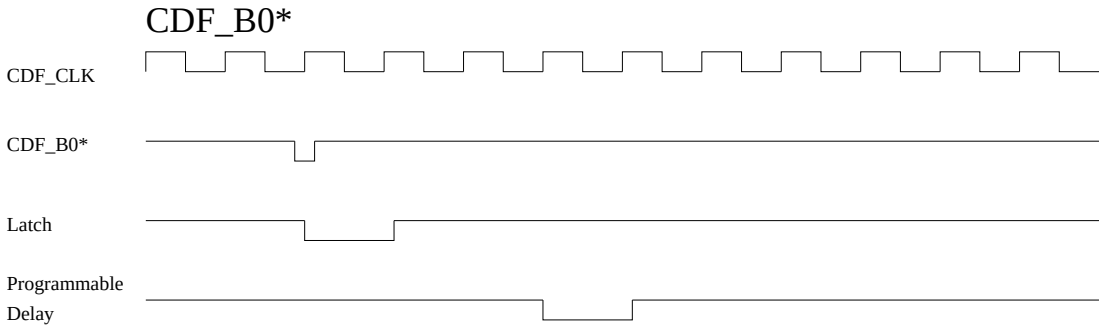

Figure 4-10: The TOTRIB latches the bunch zero signal for one clock cycle, and adds an eight bit programmable delay, or up to 256 clock cycles. Output is active low TTL.

the rising edge of the clock does not come while the data is in transition, the `CDF_CLK` sent to the J3 connector is given a programmable delay, as in Figure 4-9. The clock is in positive emitter coupled logic (PECL), a format used for high speed differential digital signaling. For synchronization, the B0 signal is sent with a programmable integer delay, as shown in Figure 4-10. When this bit is low, the corresponding data is from the first bunch crossing.

The Muon Transition Card uses the recover interval to calibrate the fiber optic hot links that transmit data to the Muon Matchbox. For this reason, the TOTRIB latches the CDF_Recover signal and extends it for a variable length of time as shown in Figure 4-10. The CDF_Halt signal is latched on the TOTRIB and transmitted through the J3 connector, as shown in Figure 4-12 [30].

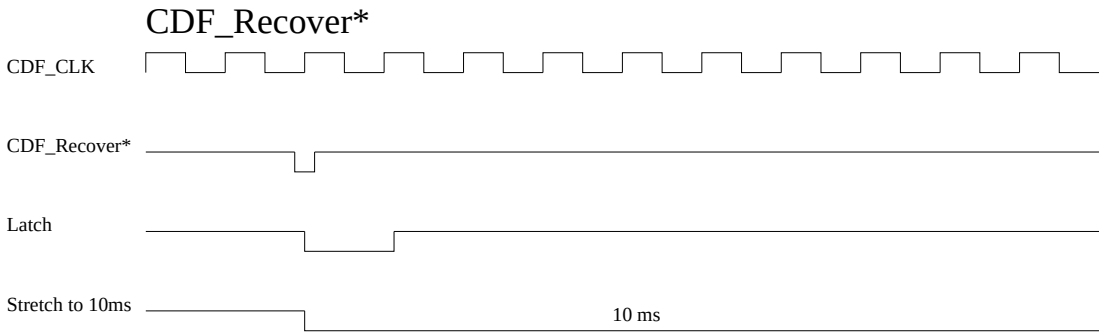

Figure 4-11: The TOTRIB latches the CDF recover signal and extends it for up to 10 ms. Output is active low TTL.

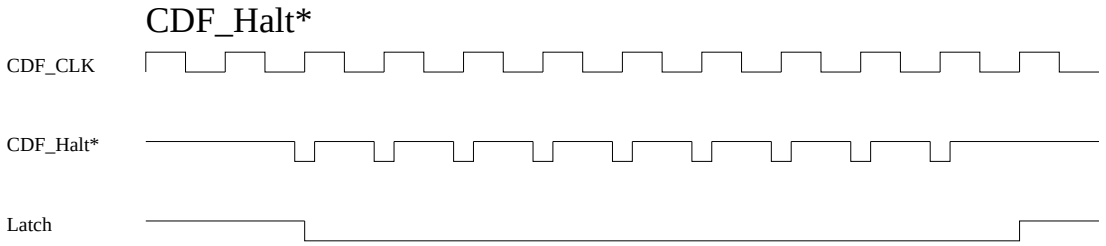

Figure 4-12: The TOTRIB latches the halt signal. A hypothetical single halt signal would be held for one clock-cycle only (as in first 3 lines of Figure 4-11). Output is active low TTL.

4.3.2 Detector Coverage, Channel Definitions and Data Path

Because a single ADMEM covers 9 bars and contains 5 FPGAs, each ADMEM presents five MIP and five HIP trigger bits to the TOTRIB. The first 4 bits refer to hits in pairs of the first eight bars and the 5th bit refers to a hit in the ninth bar. For example, HIP 2 off means no HIP level pulse was detected in either the fifth or sixth bar, and MIP 4 on means that a MIP level pulse was detected in the ninth bar; Figure 4-13 illustrates the trigger bit definitions.

Each TOTRIB accommodates six 20 bit 40 contact Berg IDC connectors that must be shared between the east and west side. Thus each trigger cable handles 2 ADMEMs, and a single TOTRIB will cover 6 ADMEMs on each side, 54 bars, or 90° of the detector. Four TOTRIBs cover the entire detector, as illustrated in Figure 4-5 and Figure 4-14.

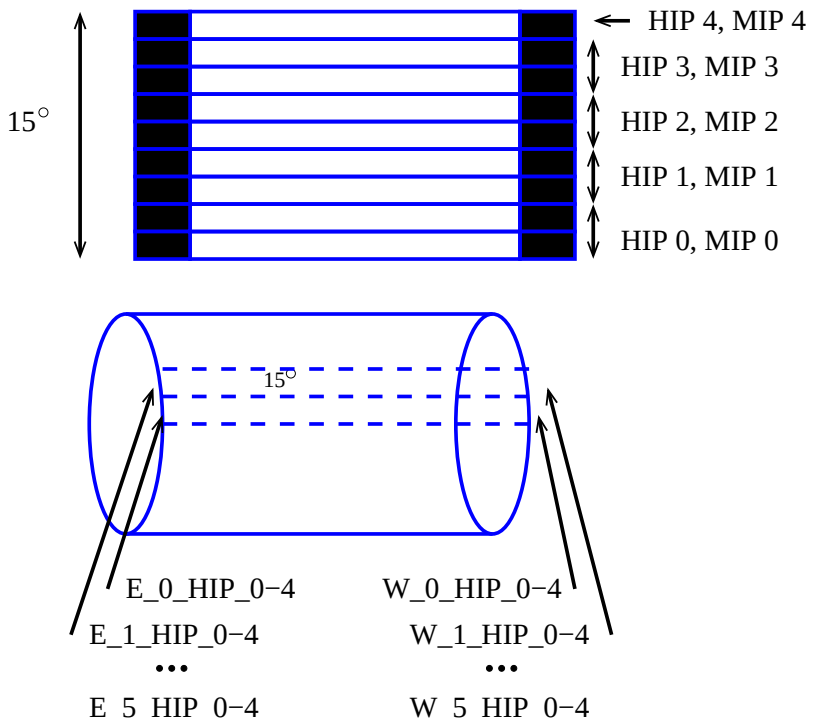

Figure 4-13: The first four HIP and MIP trigger bits refer to hits in pairs of the first eight bars. The fifth HIP or MIP bit refers to a hit in the ninth bar. Within a 90° wedge, the first 15° of bits are 0_HIP_0-4 and 0_MIP_0-4, the next 15° of bits are 1_HIP_0-4 and 1_MIP_0-4, up to 5_HIP_0-4. An E or W denotes east side or west side.

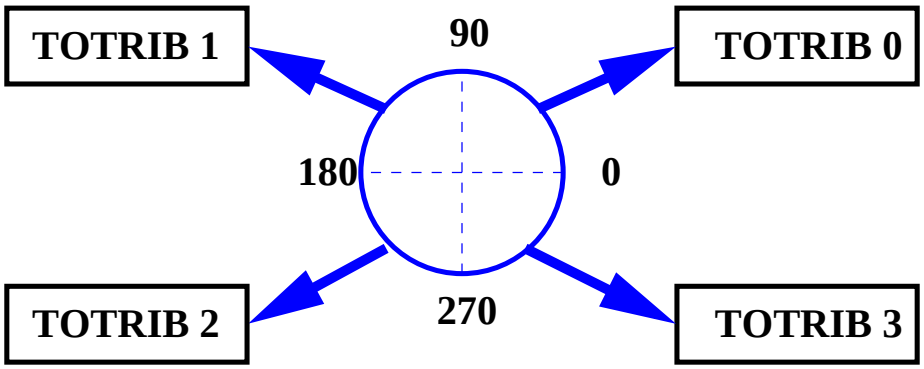

Figure 4-14: Four TOTRIBs cover the entire detector. This view faces west.

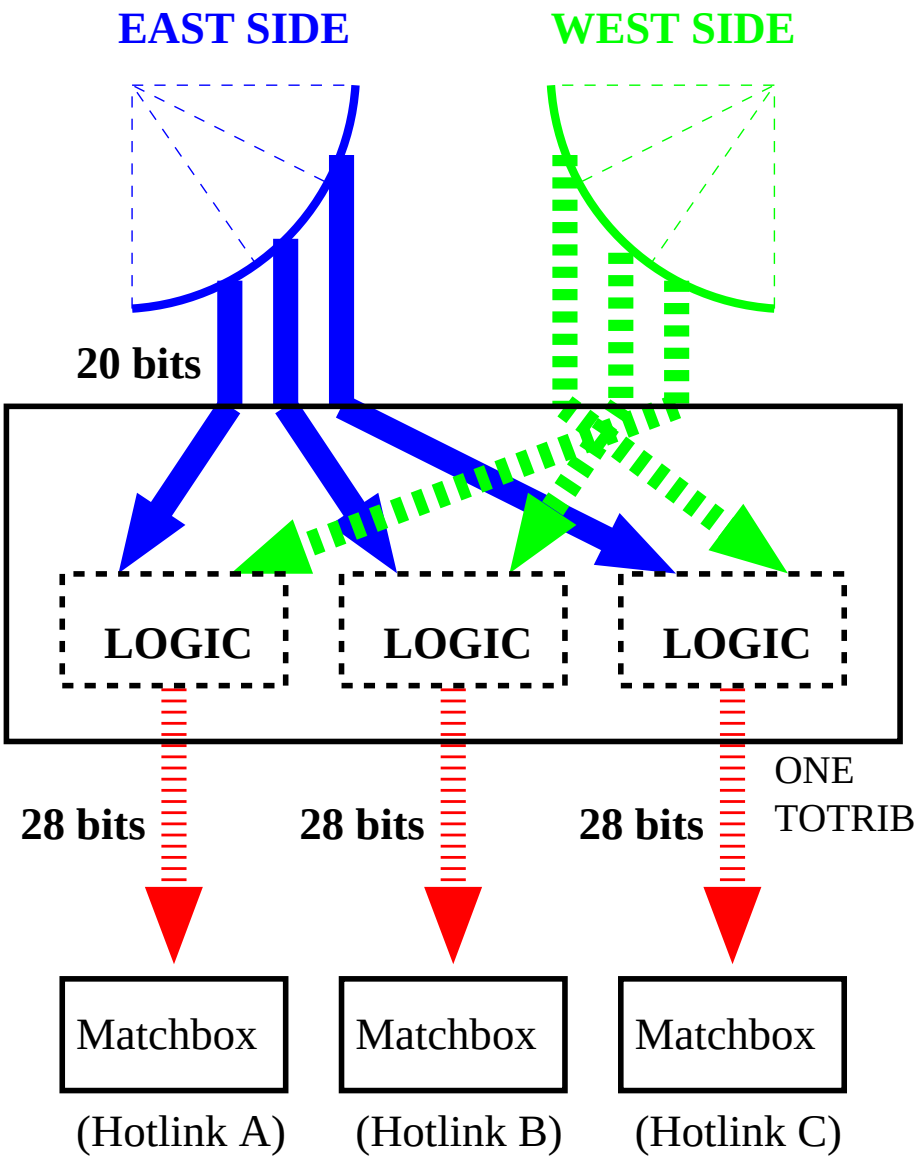

Figure 4-15: The data path in one TOTRIB.

The TOTRIB brings data from opposite sides of the detector together and checks for coincidences. The incoming data fill 20 bits per 30° per side as shown in Figure 4-15. and Figure A-1. Coarse granularity data is made by taking the logical OR of the data in a roughly 7.5° wedge. The output data fill 28 bits per 30°: 10 fine bits plus 4 coarse bits of MIP data and the same amount of HIP data. Each 30° wedge of data is sent to a corresponding Muon Matchbox through a hotlink provided by the Muon Transition Card.

4.3.3 The Input, Algorithm and Output

The TOTRIB receives LVDS trigger bits from the ADMEMs through roughly 90 m(300′) of Amphenol Twist 'N' Flat cable (Amphenol P/N 169-2832-040) terminated with a 40 channel Berg IDC connection socket. Each TOTRIB accepts six sockets with pin outs in Table A.5, Table A.6 and Table A.7.

The programmable logic checks for coincidences of HIP and MIP bits on both sides of the detector. The coincident bit for channel J of ADMEM number I is taken from the corresponding east (E) and west (W) input bits:

$$\begin{aligned} I_MIP_J &= E_I_MIP_J \ \& \ W_I_MIP_J \\ I_HIP_J &= E_I_HIP_J \ \& \ W_I_HIP_J \end{aligned}$$

Coarse data for matching with the XTRP is obtained by looking for any hit within a roughly 7.5° wedge. The first two bits (0 and 1) and last three bits (2,3, and 4) of each ADMEM output are combined:

$$\begin{aligned} I_MIP_01 &= I_MIP_0 \parallel I_MIP_1 \\ I_MIP_234 &= I_MIP_2 \parallel I_MIP_3 \parallel I_MIP_4 \\ I_HIP_01 &= I_HIP_0 \parallel I_HIP_1 \\ I_HIP_234 &= I_HIP_2 \parallel I_HIP_3 \parallel I_HIP_4 \end{aligned}$$

These MIP and HIP data proceed to a Muon Transition Card in TTL format through the J3 connector on the VME backplane. The transition board divides the 90° of data from each TOTRIB equally between three Matchboxes using fiber optic cables, or hotlinks. The channel mapping is shown in Table A.8, Table A.9 and Table A.10.

The total number of MIP coincidences in the TOTRIB is the only data needed for the MIP high multiplicity trigger. However, it is possible that other triggers will need access to the pattern of MIP hits as well as the total sum.

On the front panel, there are two output connectors, as shown on Figure 4-7. The first connector outputs the 5 bit MIP coincidence sum. The second outputs the 6 bit MIP hit pattern for 15° wedges:

$$I_MIP = I_MIP_0 \parallel I_MIP_1 \parallel I_MIP_2 \parallel I_MIP_3 \parallel I_MIP_4$$

In order to add the MIP high multiplicity trigger to a PreFRED card, the 5 bit coincidence sum is output in LVDS format with a programmable delay. The front panel MIP outputs are shown in Table A.12 and Table A.11.

To provide flexibility for future additions to the TOF trigger, the complete MIP and HIP scatter patterns are output to board mounted connectors in LVDS format; the pin outs are listed in Table A.13 and Table A.14.

4.3.4 VME Interface

The TOTRIB has an additional FPGA dedicated to VME services, using the J1 backplane connector according to the VME specifications. Most of the board parameters are set in VME buffers:

- `TOTRIB_IDPROM`: Read only memory that identifies the board as a TOTRIB.
- `TOTRIB_CLKDELAY` : The phase of the clock signal sent to the Muon Transition Card in steps of 5 ns (5 bits.)

- `TOTRIB_B0DELAY` : Number of clock cycles to delay the B0 signal sent to the Muon Transition Card for data synchronization (8 bits.)

- `TOTRIB_RCVRLNG` : Length of the recover interval (in clock cycles) sent to the muon transition card (18 bits), used to calibrate the fiber optic links.

Other board parameters are implemented as IEEE 1149.1 boundary scan (JTAG) registers. The VME interface allows access to the JTAG chain connecting the coincidence unit FPGAs to the VME FPGA. This requires the driver code to apply the appropriate steps to use the JTAG state machine: resetting the state, writing the instruction register a read or write command, then reading or writing the data register. The JTAG control register contains the following parameters:

- `TOTRIB_PIPELENGTH`: The length in clock cycles of the digital pipeline holding diagnostic data awaiting a Level 1 accept. (8 bits.)

- `TOTRIB_MIPDELAY` : The number of clock cycles to delay output to the front panel (A3,B3). The minimum is one clock cycle. (8 bits.)

The JTAG data mask register specifies input channels to ignore in case of hardware failure. This register is re-purposed as a fake data buffer for the debugging transmitter board, a modified TOTRIB that outputs fake data through the front panel connectors (A0-A2 and B0-B2.)

The VME interface allows readout of diagnostic data by the CDF data acquisition system; the required CDF specific signals are received on the J2 backplane connector. At each clock cycle the data calculated by each coincidence unit is placed in a digital pipeline, with a length specified by `TOTRIB_PIPELINE`. The data emerging from the pipeline is synchronized with the Level 1 Accept (`L1A`) signal; upon receipt of a `L1A`, the data is stored in one of four Level 2 buffers. Upon a Level 2 Accept, the readout of the data commences. The VME interface presents a virtual L2 VME buffer according to the CDF standard. As each word in the L2 buffer is requested, the VME FPGA assembles it from 8 bit installments extracted from the real buffers contained in the coincidence unit FPGAs. This somewhat slow approach is possible because

Matching quantity	XFT track quantity
ϕ_{TOF}	ϕ_{SL6}
$\Delta\phi_{\mathrm{TOF}}$	$7.5°$

Table 4.2: A simple XTRP algorithm for TOF.

the TOTRIB contains relatively little data; the readout time is dominated by other detectors with much larger buffers.

4.4 Muon Matchbox and Muon PreFRED

The TOF HIP trigger uses the Muon Matchbox to require a track pointing to a TOF bar with HIP level pulses. This is done at Level 1 using tracks roughly reconstructed by the extremely fast tracker (XFT) [31] and the extrapolator (XTRP). The muon trigger is divided into 30° wedges; the XTRP provides four bits per 30° of resolution for the TOF trigger, which is why the TOTRIB calculates coincidences at this resolution: I_MIP_01 and I_MIP_234 from section 4.3.3 and Tables A.8, A.9, and A.10. The Muon Matchbox performs a bitwise AND of the TOTRIB's HIP pulse data and the XTRP's extrapolated track data. These are the only bits used by the Muon Matchbox to make the HIP trigger decision, the other bits from the TOTRIB are included for possible future use in the Level 2 trigger decision.

The CDF calorimeters have wire chambers covering cracks in the calorimeter coverage, and a special trigger fires when the XTRP finds tracks pointing toward them. The XTRP bits available for the TOF trigger are extra crack extrapolation bits. The TOF reinterpretation of these bits, and their location in the Muon Trigger Data Bank (TCMD) is shown in Table A.16. The non-uniform phi resolution is due to the grouping of TOF bars into four pairs followed by a single bar at the ADMEMs.

The TOF data is split between two FPGAs on each Matchbox: an "East" and a "West" FPGA for the Muon detectors, 0° to 15° and 15° to 30° for the TOF, as in Table A.17. The four bits of XTRP data (crack bits) are flipped at the input to the second FPGA: (A, B, C, D) becomes (C, D, A, B). This decides the bit interpretation;

the logic on both FPGAs is identical. The overall HIP trigger decision is the logical OR of all of the individual HIP decisions made by each FPGA:

$$\mathrm{HIP} = \mathrm{HIP}_{0,0} \mid \mathrm{HIP}_{0,1} \mid \mathrm{HIP}_{1,0} \mid \mathrm{HIP}_{1,1} \mid ... \mid \mathrm{HIP}_{11,0} \mid \mathrm{HIP}_{11,1}.$$

The track matching at the Muon Matchbox has been found to be unnecessary for controlling the rate at present luminosities. The rate can be controlled by the pulse height thresholds and east-west coincidence requirement alone. For this reason, the XTRP has been programmed to always send all four TOF bits high, as if there is a track pointing to every TOF bar. If track matching is needed in the future, a simple extrapolation procedure is needed to fill the XTRP lookup tables. The simplest procedure is outlined in Table 4.2; the extrapolated ϕ is taken from the ϕ position in super-layer 6 (near the TOF bar) and the ϕ resolution is one half of a wedge.

4.5 BSC-TOF PreFRED

There are two MIP triggers, a multiplicity trigger and a cosmic trigger, both implemented on the BSC-TOF PreFRED. For the MIP multiplicity trigger, the four partial MIP sums from the front panel output of the TOTRIBs are added together. If the sum is within a specified range, the trigger fires. There is also the possibility to have a second multiplicity trigger, using a separate range, but the same MIP threshold. The cosmic trigger uses the 15° resolution MIP scatter pattern from the TOTRIBs front panel to require nearly back to back MIP wedges, as in Figure 4-16.

trigger	PreFRED bit(s)
TOF_MULTIPLICITY	8,9
TOF_COSMIC	9

Table 4.3: The BSC-TOF PreFRED bit assignment.

Because the BSC-TOF PreFRED handles only a limited number of input channels, a multiplicity trigger cannot run at the same time as the TOF cosmic trigger. The PreFRED masks out the scatter pattern input when the multiplicity trigger is used,

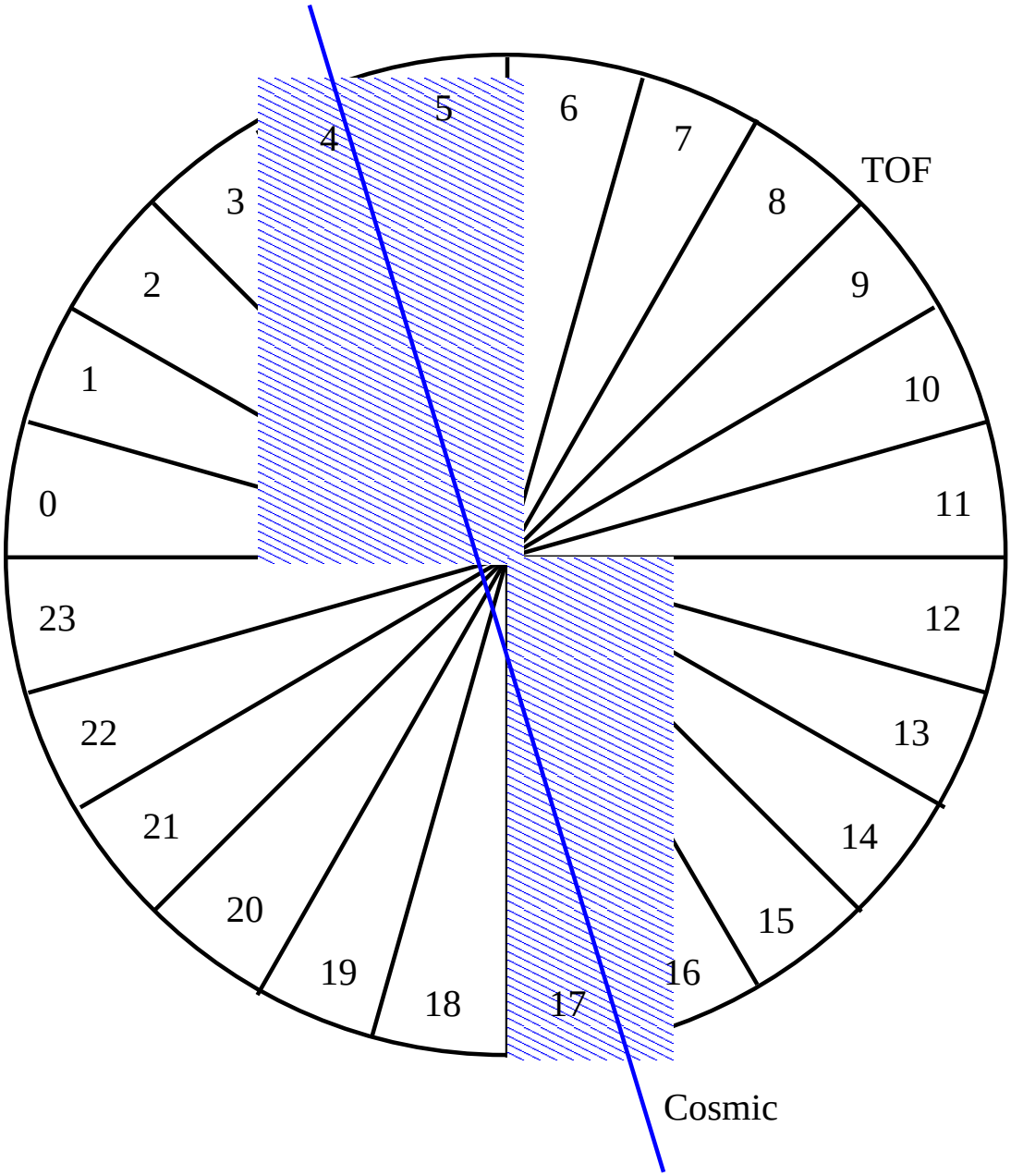

Figure 4-16: The TOF cosmic trigger requires two nearly back to back hits in the TOF system.

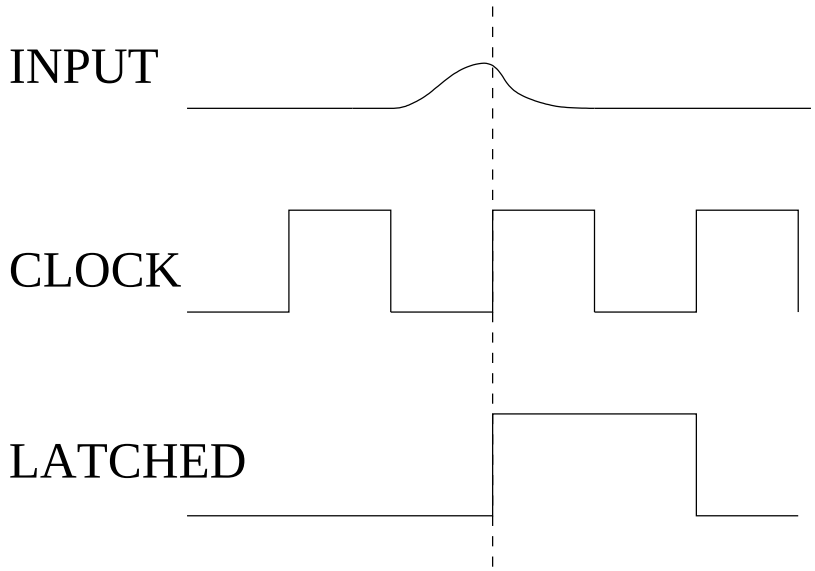

Figure 4-17: The clock phase is adjusted to ensures that data is latched while the input is valid.

and the sum when the cosmic trigger is used. This also allows the cosmic trigger and multiplicity trigger to share a precious PreFRED bit, as in Table 4.3.

The BSC-TOF PreFRED is also unable to separately synchronize the trigger data from the many different detectors sent to it. For this reason, the MIP output is delayed by 5 clock cycles on the TOTRIB to arrive in sync with the delayed BSC data.

4.6 Timing

There are two timing considerations for digital electronics: the clock phase and the synchronization of data. These are often referred to as fine and coarse timing adjustments.

Typically a digital device samples an input at the leading edge of a clock cycle, and holds the value for the rest of the cycle. Adjusting the phase of the clock, the fine timing adjustment, ensures that this *latching* occurs at a time when the input is valid, as illustrated in Figure 4-17. For robust digital signals, there is often only a brief period of transition where the input signal is invalid, but for signals attenuated and distorted by long cables the transition can take longer.

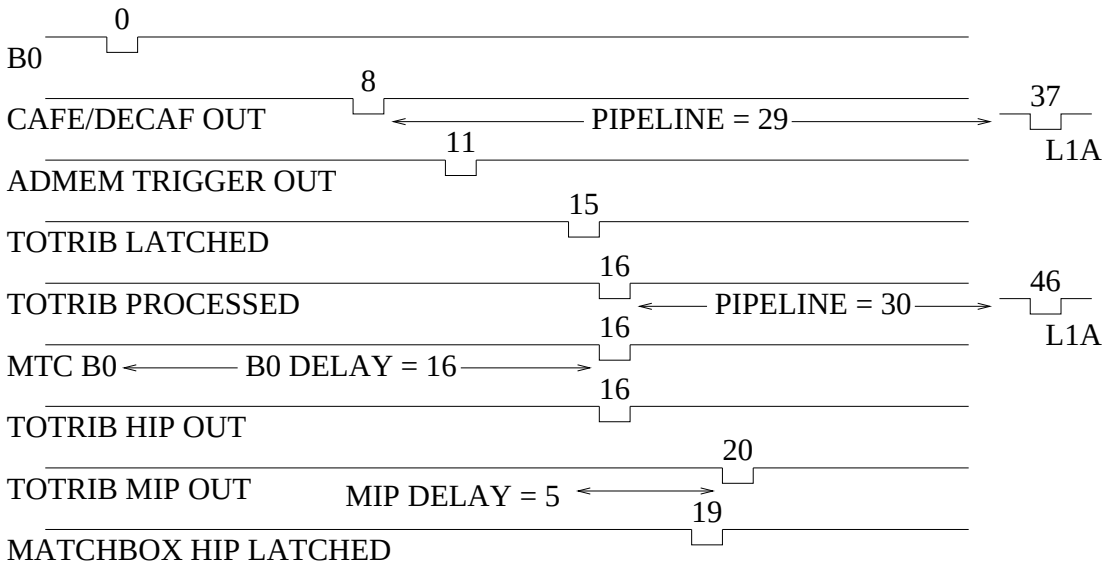

Figure 4-18: By carefully accounting for electronics delays at each stage, the TOF trigger timing parameters are explained.

The fine timing adjustment at the TOTRIB was made by measuring the phase of the output data relative to the `CDF_CLK` with an oscilloscope, and adding an appropriate length of cable. A more robust solution would have been to include an adjustable phase to the `CDF_CLK` used on the TOTRIB. Such a phase is added to the clock sent to the Muon Transition Card where it is hardly needed, due to the robustness of signals passing through the J3 connector. The fine timing adjustment to the MIP trigger output is made on the BSC-TOF PreFRED.

Since CDFs myriad detectors process data at different speeds, various coarse timing adjustments insure that the data is synchronized when needed. For the readout, the synchronization mechanism is called the Level 1 Pipeline. Data is held in a pipeline with the length adjusted so that data is coming out just as the global Level 1 decision for that event reaches the front end crate.

For other synchronization purposes, the CDF system uses the first or each group of bunch crossing, Bunch Zero, as a reference. At the bunch zero event, a `CDF_B0` signal is asserted on the backplane of the CDF front end crate. This is the main synchronization signal. The TOTRIB latches and delays the `CDF_B0` signal before sending it to the Muon Transition Card along with the trigger data. This delay

Component	Parameter	Setting
ADMEM	PIPELENGTH	29
TOTRIB	PIPELENGTH	30
TOTRIB	BO_DELAY	16
TOTRIB	MIP_DELAY	5
TOTRIB	CLK_DELAY	10

Table 4.4: Timing parameters for the TOF trigger.

means that the bunch zero bit is active for the data which comes from the bunch zero event. The Muon Matchbox then automatically synchronizes the data arriving from various detectors using this bit. To avoid rehashing the downstream timing of muon trigger, the TOF trigger data needs to reach the matchbox within 20 clock cycles, which it manages with a single clock cycle to spare. This is the reason that the MTC delay is so small. Typically, the clock phase would be a half clock cycle away from the transition, but we choose to move the latching phase up to just after the data becomes valid, and manage to buy an extra clock cycle.

The MIP data is delayed on the TOTRIB, using another pipeline, in order to synchronize it with other data going to the BSC-TOF PreFRED data. Synchronizing at the source allows the data from the TOTRIB to tag along, as if it was coming from another detector, without any adjustment at the PreFRED.

With a careful accounting of processing time, one can see how the various timing parameters from Table 4.4 emerge. This is depicted in Figure 4-18.

4.7 Trigger Tables

The global CDF trigger is configure using a trigger table. At the lowest level, a trigger table consists of trigger options, which are the specific triggers, and the cuts and parameters associated with each trigger option. The trigger validation code checks that a series of cuts and parameters are valid for a trigger option, usually reflecting hardware constraints. Paths are used to specify a combination of triggers that results in data being written to tape, and datasets specify which trigger paths

HIP (L1)					
Cuts	Units	Type	Range	Step	Default
TOF_THRESH	MIP	float	0-100	0.05	10
XFT_PT	GeV/c	float	1.5-192.	0	none
TOF_MULTIPLICITY (L1)					
Cut	Units	Type	Range	Step	Default
TOF_THRESH	MIP	float	0-100	0.05	10
N_MIN	None	integer	0-120	1	1
N_MAX	None	integer	0-120	1	120
TOF_COSMIC (L1)					
Cut	Units	Type	Range	Step	Default
TOF_THRESH	MIP	float	0-100	0.05	10

Table 4.5: Trigger table parameters for all three TOF trigger options.

should be grouped together.

The cuts and parameters for the TOF trigger options are listed in Table 4.5. To ensure that the trigger table settings reflect possible hardware configurations, there are rules:

- There can be at most one HIP special option. TOF_THRESH from this instance of HIP(L1) special options is conceptually TOF_THRESH_HIP.
- TOF_THRESH from first instance of TOF_MULTIPLICITY or TOF_COSMIC is conceptually TOF_THRESH_MIP. All other instances of these options must have the same value.
- There can be zero or one TOF_COSMIC special options, and there can be zero to two TOF_MULTIPLICITY special options, but there cannot be a TOF_COSMIC and a TOF_MULTIPLICITY special option in the same table.

Chapter 5

Adding Monopoles to GEANT

GEANT is a widely used tool for detector description and simulation [32], but does not handle particles with magnetic charge. In this chapter we describe an extension to track a simple monopole having magnetic charge, but no electric charge or hadronic interactions.

GEANT simulates particles passing through a detector, calculating each trajectory step by step, handling the motion in an arbitrary magnetic field, interactions with material in the detector, and decays of unstable particles.

Each step size is chosen small enough to accurately treat all processes independently. For instance, the energy loss continuously effects the trajectory, but for a small enough step size it can be calculated after the particle has been transported. GEANT uses path length, not time, as the independent variable in its integrations, a simplification mainly because material interactions have characteristic lengths.

The step size is taken from many constraints. For example, a large field gradient, strong trajectory curvature, or rapid energy loss reduces the size. When a step size cannot be estimated ahead of time, it is done iteratively; if a calculated effect is too large, the step is recalculated with a reduced size.

Discreet processes are handled differently. For an unstable particle, the proper lifetime is chosen at the start by drawing an exponentially distributed random number using the particle's mean lifetime as the parameter. At each step, the remaining lifetime and the particle's momentum are used to calculate a decay distance. If the

step size eventually chosen is smaller than this distance, the elapsed proper time of the step is subtracted from the particle's remaining lifetime. Otherwise the step size is shortened to the decay distance and the decay process is performed at the end of the step.

Material interactions are handled in a similar fashion, with a random distance drawn using the interaction length as a parameter. Because this is meaningful only if the interaction length of the material is constant, GEANT does not allow a step to cross a volume boundary. It handles this internally by treating boundary crossing as if it were another kind of interaction guaranteed to occur at the boundary.

5.1 Code Layout

GEANT uses a modular design which allows different particles to share appropriate code. User entry points are provided using names beginning with `GU` (e.g. `GUTRACK`); the default behavior is to merely call GEANT code, but users can add there own special purpose code as needed.

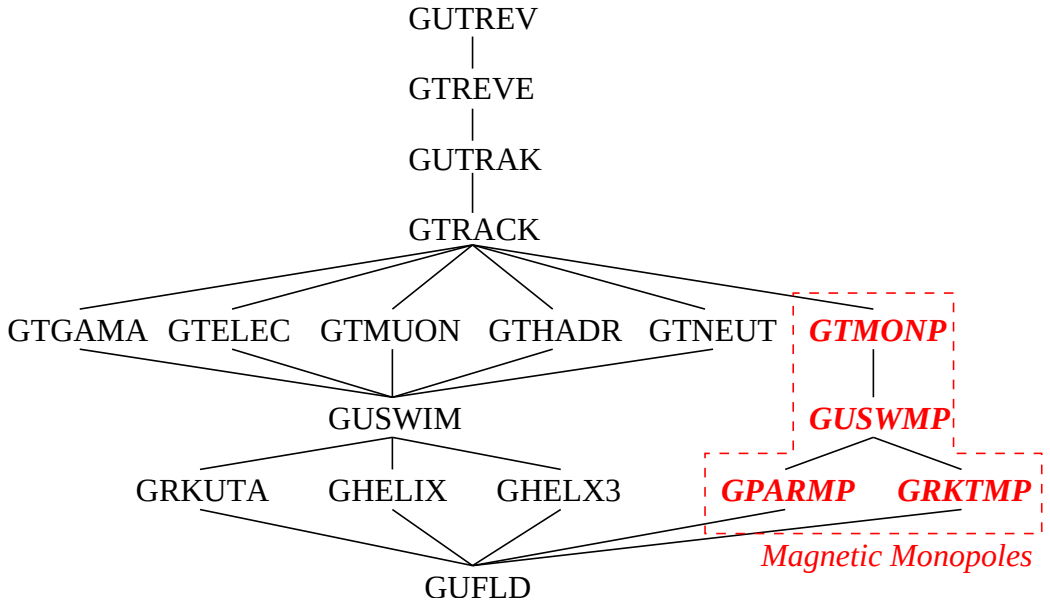

Figure 5-1: The GEANT tracking package with the addition of Monopoles.

Figure 5-1 shows a partial calling graph for GEANT tracking. Our additions, covered in detail below, are in the dashed box. There are three important divisions

in this graph:

1. At the highest level, GEANT performs bookkeeping tasks and decides the appropriate code to call for each particle. Code for the entire event, `GUTREV` and `GTREVE`, calls generic code to step through one track, `GUTRAK` and `GTRACK`.

2. At the next level, the appropriate particle specific code—`GTGAMA`, `GTELEC`, `GTMUON`, `GTHADR`, `GTNEUT`, or `GTMONP`—is chosen by "tracking type" based on charge, mass, equations of motion, and the types of interactions considered. This code performs a single step, deciding the appropriate step size and handling interactions.

3. At the lowest level, the actual numerical integration of the equations of motion is performed. A user routine—`GUSWIM` or `GUSWMP`— chooses which numerical integration—`GRKUTA`, `GHELIX`, `GHELX3`, `GPARMP`, or `GRKTMP`—to use based on the uniformity and strength of the magnetic field as calculated by the user supplied routine `GUFLD`.

Additional GEANT code, not shown in the calling graph, calculates physics processes such as energy loss fluctuations and multiple scattering. The particle specific tracking code selects appropriate physics processes to apply.

We add Dirac monopoles in a manner consistent with GEANT's organization. Because the equations of motion for magnetic monopoles and standard GEANT particles are completely different, we use a new tracking type, `ITRTYP`= 9, corresponding to routine `GTMONP` and alter `GTRACK` accordingly.

Normally in GEANT, the particle specific code calls `GUSWIM` to transport the particle. The arguments to `GUSWIM` do not allow the integration routines to alter the total energy, because the magnetic field does no work on an electric charge. The magnetic field does work on a magnetic charge, however, and so a change is needed. Rather than modify `GUSWIM` and all code that calls it, we have `GTMONP` call a new similar routine `GUSWMP`. `GUSWMP` calls an appropriate numerical integration of the equations of motion: `GPARMP` for an analytic solution and `GRKTMP` for Runge-Kutta integration.

5.2 Monopole Tracking

The main monopole tracking routine, `GTMONP`, is derived from the charged hadron tracking routine, `GTHADR`, but with decays, hadronic interactions, and stopping calculations omitted. The relevant kinematic parameters are the same for monopoles and hadrons, so no additional parameters are needed.

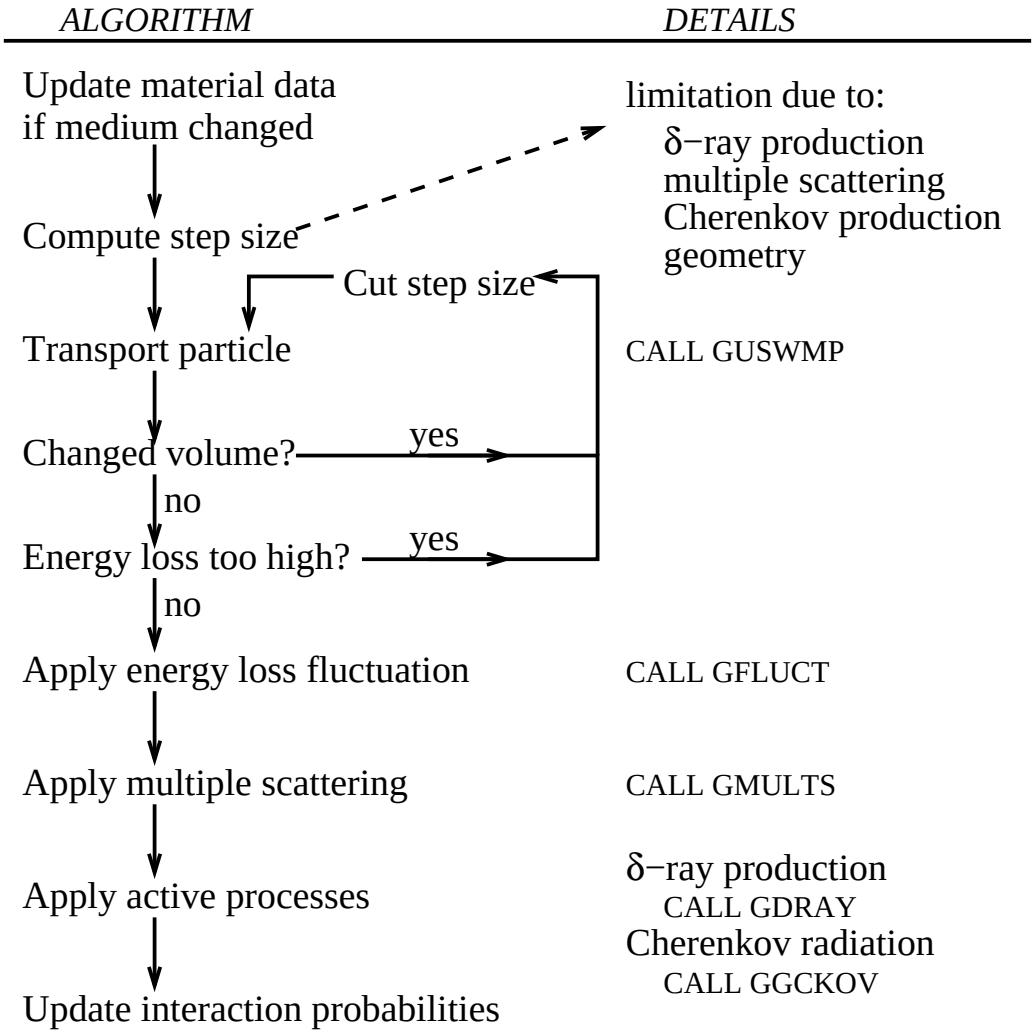

Figure 5-2: The algorithm for the monopole tracking routine GTMONP.

Figure 5-2 illustrates the monopole tracking algorithm. A step size is chosen based on the particle's position in the volume and material interactions. It is transported by the numerical integration, and the effects of interactions are calculated. If the effects are too large, the step size is reduced and the calculations are repeated.

In order to transport a monopole according to the kinematics of Section 2.2, a suitable numerical routine is chosen. For a constant magnetic field in the z direction, `GPARMP` applies an analytic solution to the equations of motion. A simple numerical integration is still needed to obtain the step size from the time based analytic solution. For non-uniform magnetic fields, `GRKTMP` performs a fourth order Runge-Kutta integration of the equations of motion. There are more efficient integration methods available but they are unreliable if the integrand is not guaranteed to be smooth [33]. That is usually the case for HEP applications, where the magnetic field map is often based on table lookups and split into several pieces, each covering a different region of the detector.

The step size is limited to ensure that the relative error in the total momentum at each step is less than one part in 10^5, which is hard coded for the moment. The safe step size estimate, Δs_{safe}, for a maximum relative error δ is given by

$$\Delta s_{safe} = 7388 \cdot \frac{p^2}{gE|\vec{B}|}\delta^{1/5}. \tag{5.1}$$

Here E is the total energy, p the total momentum, and $\vec{B}$ the magnetic field. The formula is obtained using the step doubling procedure outlined in Reference [33].

An independent limit on the error of each momentum component is not implemented because a component may reverse sign, due to the magnetic force, leading to a step size of zero at the turning point. The step size is already limited to keep the particle in the same volume and by material interactions; additional limits are unnecessary because the position is only related to the momentum. If we take care of the momentum the position will take care of itself.

The path length parametrization of the equations of motion has a singularity at zero total momentum, but we have disregarded it. It is beyond the scope of the GEANT simulation to model the trapping of monopoles in matter. In a solenoidal field with the magnetic field parallel to the beam line it is possible for a monopole to come to a momentary complete stop, only to be accelerated by the magnetic field. But these events are irrelevant; the monopole is swept out inside the beam-pipe without

reaching the detector. If a proper treatment of the singularity is needed, it can be stepped around using the time parameterization. When a particles kinetic energy drops below a small threshold, the usual behavior of GEANT is to stop the particle and deposit the remaining energy in the current medium. This is sufficient for our purposes.

5.3 Energy Loss and Delta Rays

After transporting the particle according to the equations of motion, the energy loss due to ionization is calculated. As shown in Section 2.6, a magnetic monopole does not obey the standard Bethe-Bloch formula. We have implemented both the full treatment of Ref. [10] and the naive model $e \to g\beta$, which are nearly equivalent for our purposes. The full treatment is implemented in the routine `GDRELO`. At present, it is called at each step in `GTMONP`, but a more efficient treatment would be to generate a new monopole energy loss table as is done for other particles.

Because the naive monopole energy loss formula is related to the standard formula by a simple substitution and both depend only on β and not m when $m \gg m_e$, one can adapt the proton loss tables and need not calculate new ones.

The monopole energy loss $\frac{dE}{dx}^{mon}$ is obtained by scaling the proton energy loss $\frac{dE}{dx}$:

$$\frac{dE}{dx}^{mon} = \frac{dE}{dx} \cdot (ng)^2 \cdot \beta^2$$

The proton is considered to have the same velocity as the monopole, so that the energy is:

$$T_0 = \frac{m_p}{m_{mon}} \cdot T_{mon}$$

The proton energy loss is interpolated from GEANT's lookup table $\frac{dE}{dx}(T_n)$, which gives the energy loss at discreet energies. This requires finding the index i corresponding to the proton energy, T_0, such that $T_i < T_0 \leq T_{i+i}$. The interpolated value is then:

$$\frac{dE}{dx}(T_0) = \frac{dE}{dx}(T_i) + \frac{T_0 - T_i}{T_{i+1} - T_i} \cdot \left(\frac{dE}{dx}(T_{i+1}) - \frac{dE}{dx}(T_i) \right)$$

The index i and interpolation coefficient are already calculated in GEANT for charged hadrons and heavy ions in subroutine `GEKBIN`; we modified it to do exactly the same thing for monopoles. `GTMONP` performs the interpolation and the final scaling.

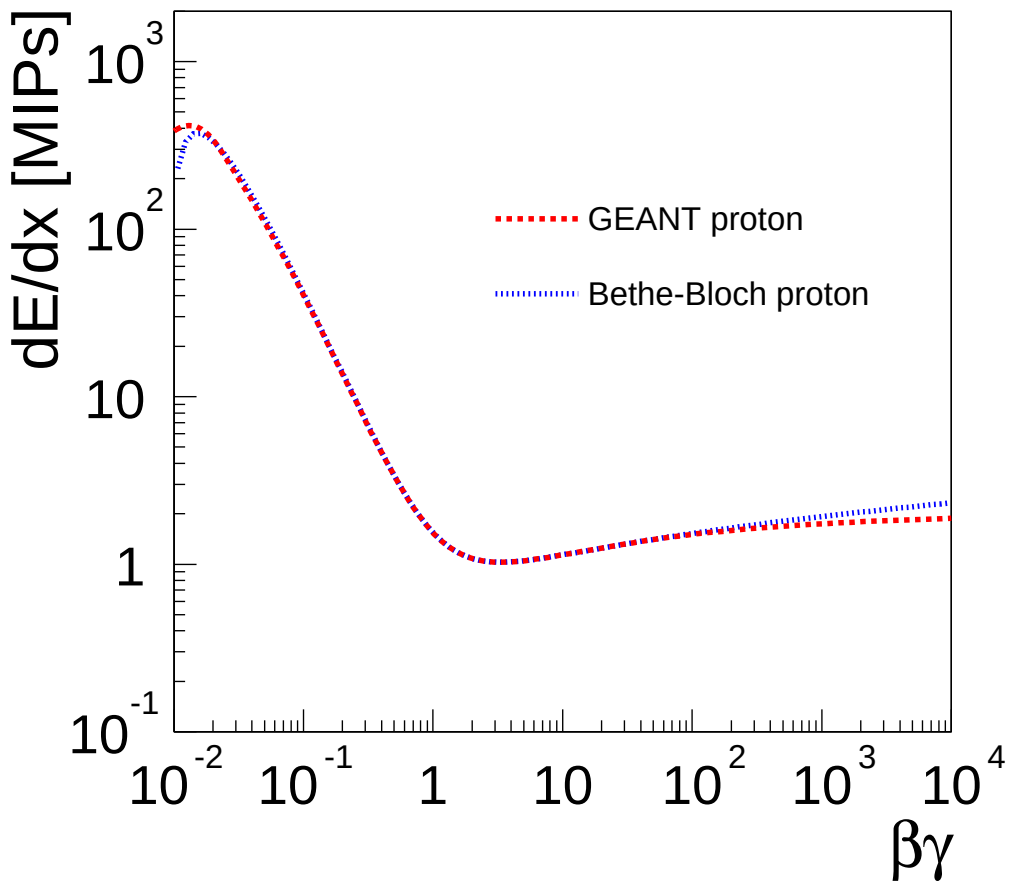

Figure 5-3: A comparison of the Bethe-Bloch formula with GEANT tables for the energy loss of protons in air.

Figures 5-3 and 5-4 compare the energy loss curve from the GEANT table with the Bethe-Bloch formula, for monopoles and protons. The energy loss for a monopole in GEANT agrees well with Equation 2.33. The curves only diverge significantly for $\beta\gamma < 2 \cdot 10^{-2}$, where the Bethe-Bloch formula is an inadequate description and GEANT uses a fit to measurements[1].

[1] After version 3.15 GEANT does not use direct linear interpolation of the energy loss tables for standard particles but uses stopping range tables instead. This is done in order to avoid overesti-

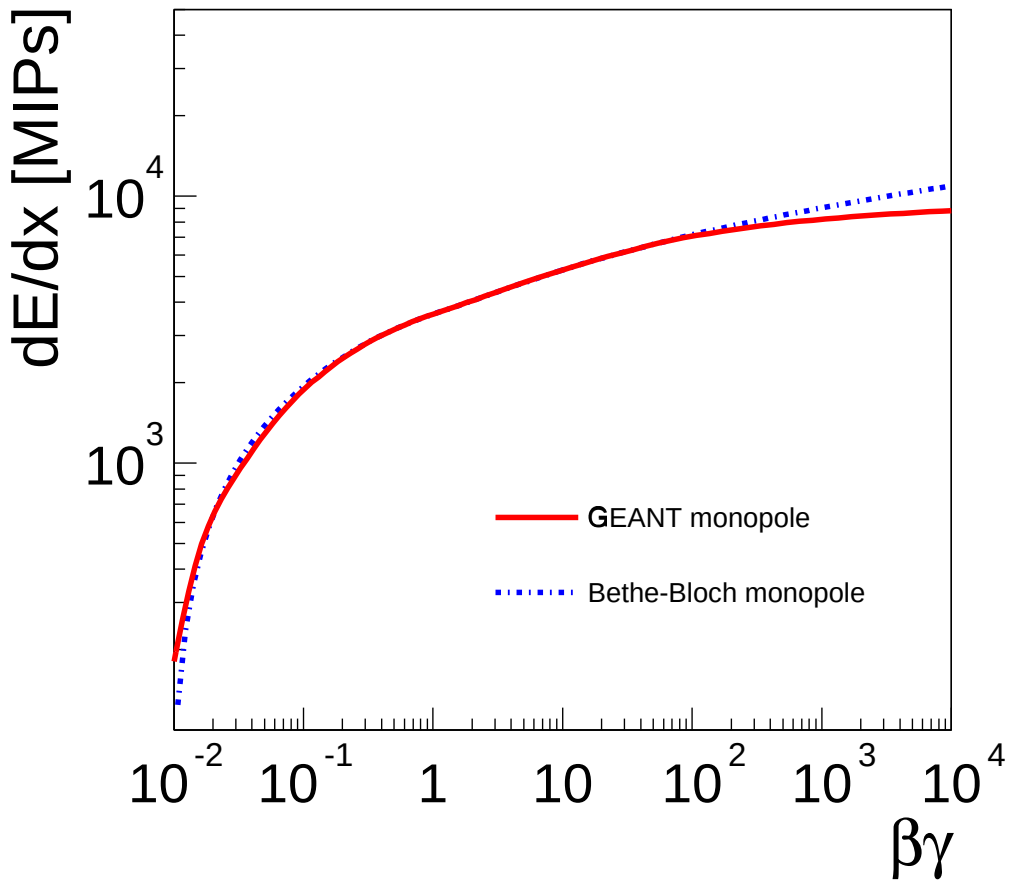

Figure 5-4: A comparison of the Bethe-Bloch formula with GEANT tables for the energy loss of monopoles in air.

The energy loss fluctuations and delta ray production are calculated using the standard GEANT methods, with the replacement of ze with $ng\beta$, as discussed in Section 2.6.

5.4 Multiple Scattering

For multiple scattering, GEANT provides a Molière model, a plural scattering model, and a Gaussian model. Because the monopoles we are considering are much heavier

mating energy losses near the $\beta = 0$ singularity of the Bethe-Bloch equation. Monopoles do not have this singularity so the older method is still applicable.

than ordinary hadrons ($m \geq 100$ GeV), they have very small scattering angles, and we do not need the non-Gaussian tails of the full Molière model. We modified the main multiple scattering routine, `GMULTS` to use the Gaussian model, `GMGAUS`, for monopoles. For electric charges this routine calculates the RMS scattering angle:

$$\theta_0 = 2.557\chi_{cc} ze \frac{\sqrt{d}}{E\beta^2} \ , \tag{5.2}$$

where χ_{cc} is a characteristic of the material and d is the integration step size. The scattering angle defines a cone around the particles momentum. For isotropic materials any direction within the cone is equally likely, and so one is chosen at random. We substitute $ng\beta$ for ze in two steps: in `GTMONP` by setting `CHCMOL` to $\chi_{cc}ng$ instead of χ_{cc} and in `GMULTS` by calling `GMGAUS` with β instead of β^2. These substitutions are made only for monopoles (`ITRTYP=9`).

5.5 Code Validation

One cannot—at least yet—compare the GEANT simulation with real data, meaning that cross checks are the only available tool for validating the code. We compare the GEANT code with a simpler monopole simulation and compare the Runge-Kutta integration with the analytic solution. None of these checks validate the assumptions and models discussed in the previous sections; they merely check for mistakes in the implementation.

5.5.1 Comparison with a Stand-Alone Simulation

We created a stand-alone monopole simulation using ROOT [34], called MonSim, which is completely independent from GEANT. MonSim uses a simplified detector geometry with most regions modeled as uniform cylinders. It treats the energy loss using the monopole Bethe-Bloch formula (Equation 2.33) and multiple scattering using the Gaussian model (Section 2.7). It also assumes that the magnetic field is uniform and points in the $+z$ direction. In this case, the equation of motion has an

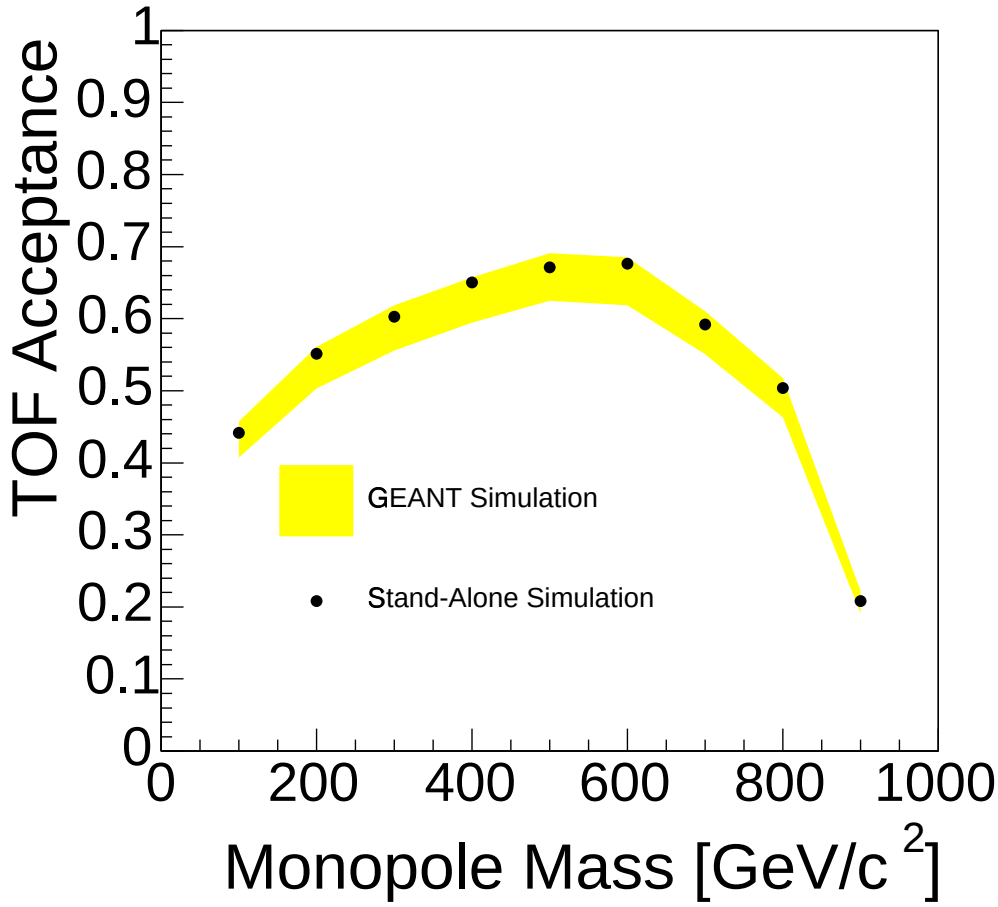

Figure 5-5: A comparison of the TOF acceptance for GEANT and MonSim.

analytic solution (Equation 2.12).

For the comparison, both simulations use a simplified model of the CDF detector, consisting of the beam-pipe, central tracker, TOF detector, and solenoid. We take the proton direction along the beam-pipe as $+z$, upward as $+y$, and the usual azimuthal angle as ϕ.

Monopole pair events with identical initial conditions were simulated in both programs. The acceptance of the TOF system across a range of monopole masses is shown in Figure 5-5 as measured by both programs; they are in good agreement. The difference between GEANT and MonSim calculations of the E, z, and ϕ of the monopole at the radius of the TOF scintillator are shown in Figure 5-6, Figure 5-7,

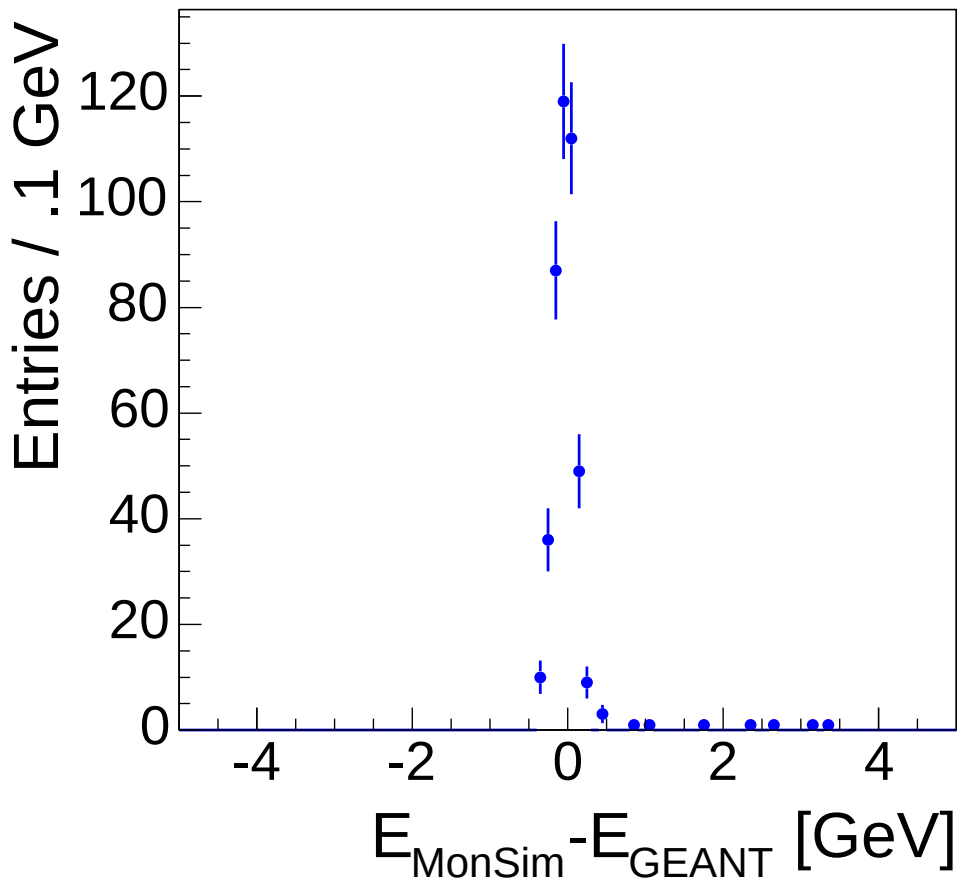

Figure 5-6: The total energy difference at the TOF radius for GEANT and MonSim.

and Figure 5-8 for a monopole with 500 GeV mass. The trajectory and energy dependence of single typical event is shown in Figure 5-9 and Figure 5-10. The agreement between the two programs is excellent.

There are some tails in the distributions, however. One tail event is shown in Figure 5-11 and Figure 5-12. At the turning point, the monopole has very little energy, and the discrepancy between the Bethe-Bloch formula and the GEANT tables becomes noticeable (Figure 5-4). The later rapid acceleration of the monopole has the effect of magnifying this small difference. Even for tail events, the discrepancy is less than 1% of the total energy of the particle.

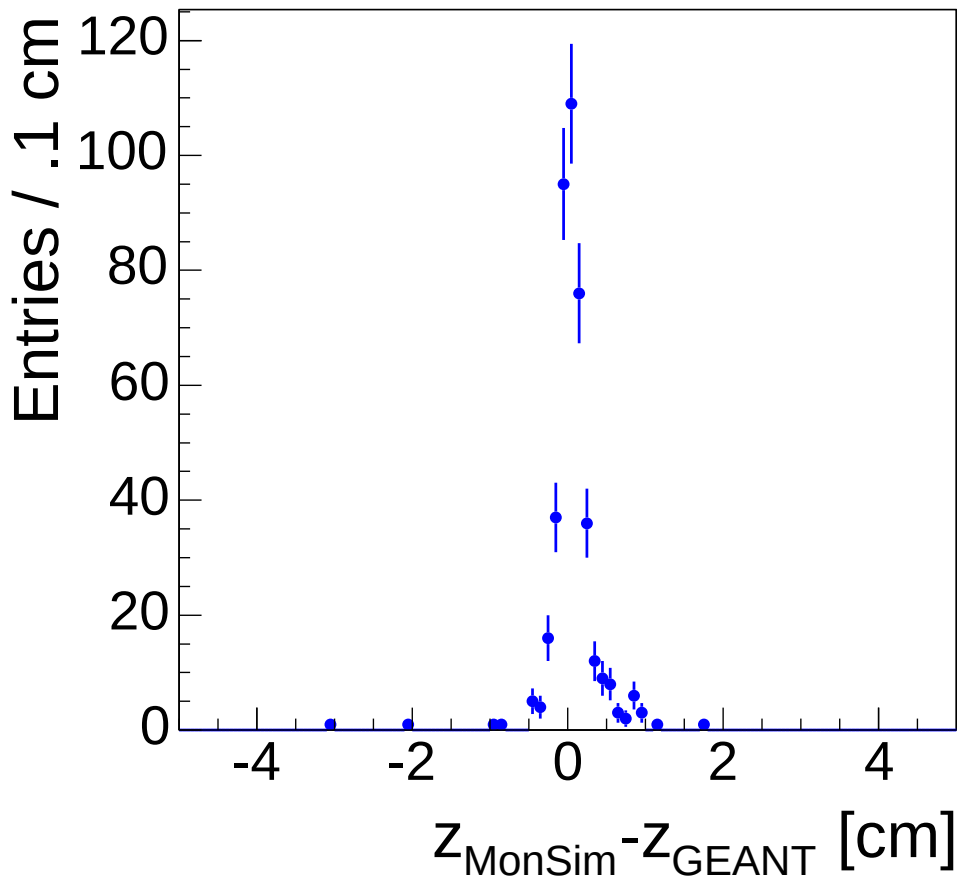

Figure 5-7: The z difference at the TOF radius for GEANT and MonSim.

5.5.2 Comparison between analytic and Runge-Kutta solutions

As an additional cross check, we compare both GEANT implementations: the analytic solution `GPARMP` and the Runge-Kutta integration `GRKTMP`. As in the previous section, we compare the Energy (Figure 5-13), z (Figure 5-14), and ϕ (Figure 5-15) difference at the TOF radius. The results are in excellent agreement, with slightly asymmetric tails due to the assumption, in `GPARMP`, that the magnetic field is in the z direction only.

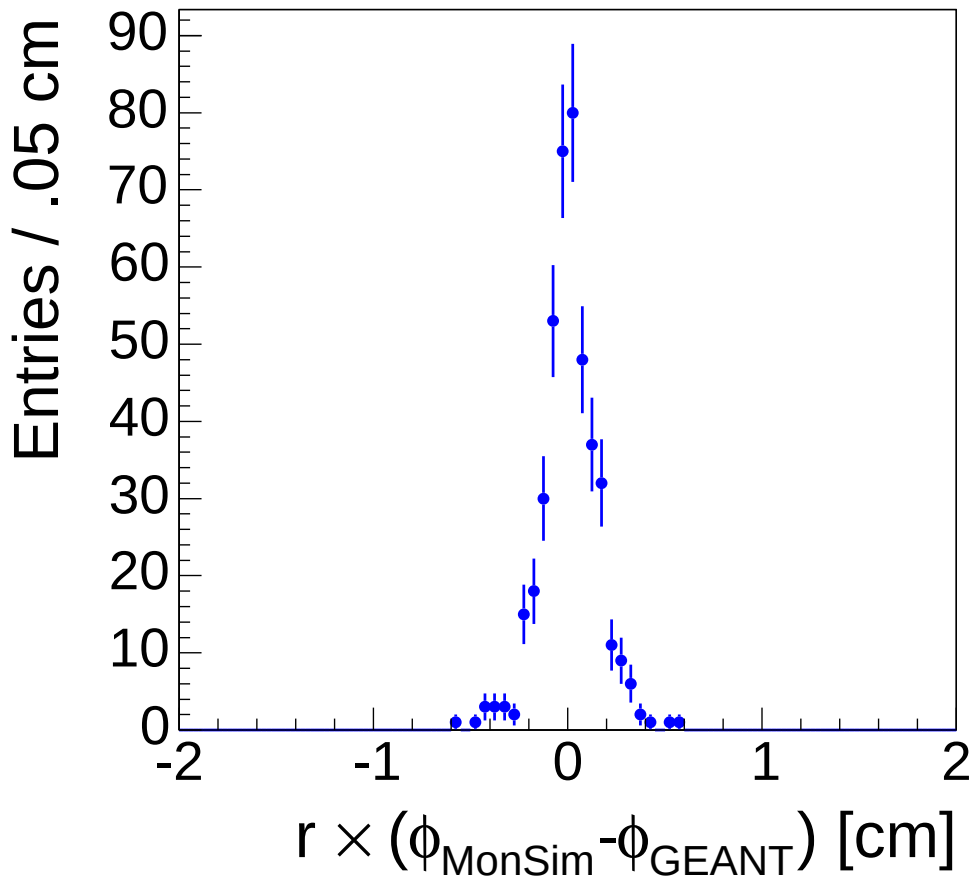

Figure 5-8: The ϕ difference at the TOF radius for GEANT and MonSim.

5.6 Summary

The extension of classical electromagnetism to include magnetic charge leads to a symmetry between electric and magnetic quantities. This symmetry can be exploited to deduce magnetic interactions from electric ones in a straightforward way. Using this model, GEANT has been extended in a consistent fashion to handle magnetic monopoles. We have tested our GEANT implementation against a much simpler dedicated monopole simulation. The two independent programs are in excellent agreement.

The magnetic monopole extension to GEANT is available for download from `http://fcdfhome.fnal.gov/usr/mulhearn/geant-monopoles/`

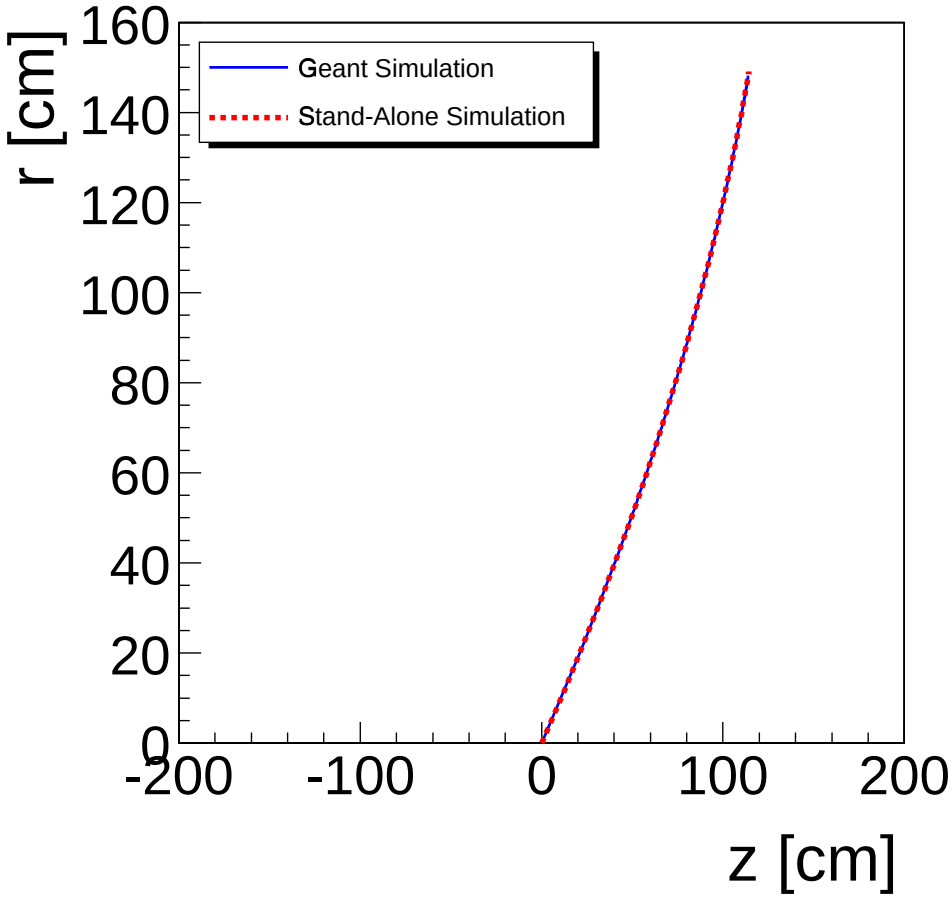

Figure 5-9: The monopole trajectories in r-z for a typical event.

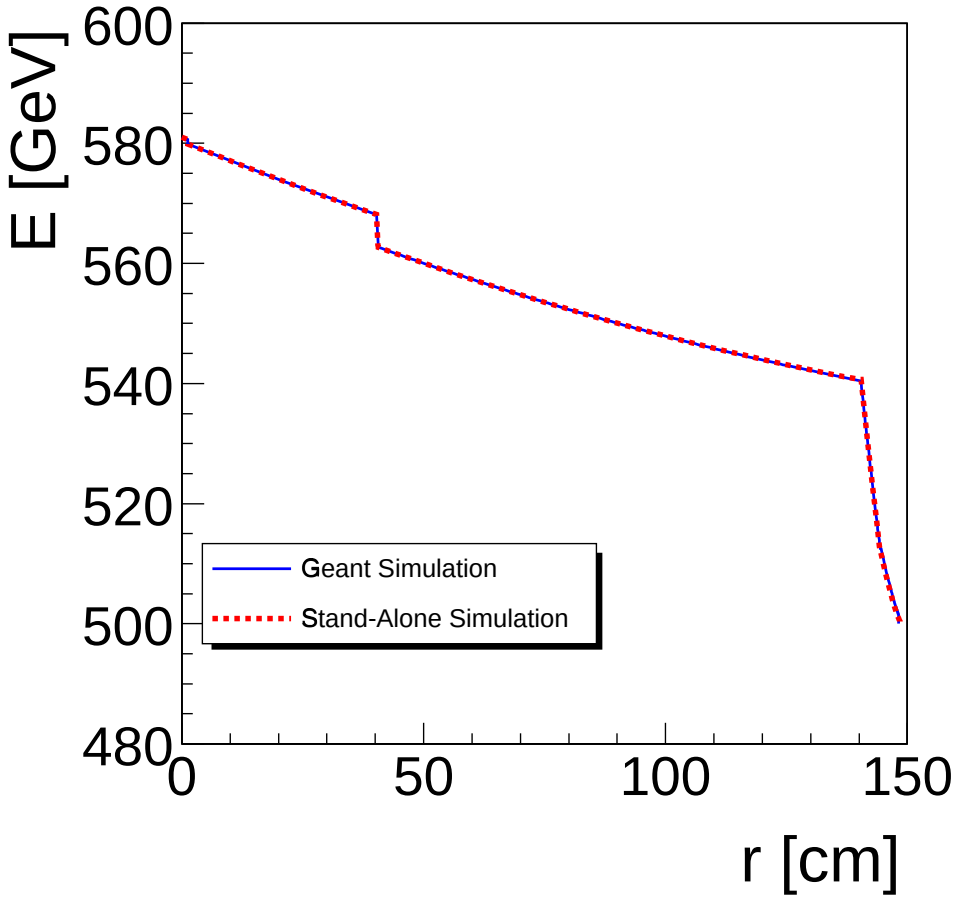

Figure 5-10: The monopole energy versus radial distance for Figure 5-9. The large kinks are due to rapid energy loss at the COT inner cylinder and TOF scintillator bars.

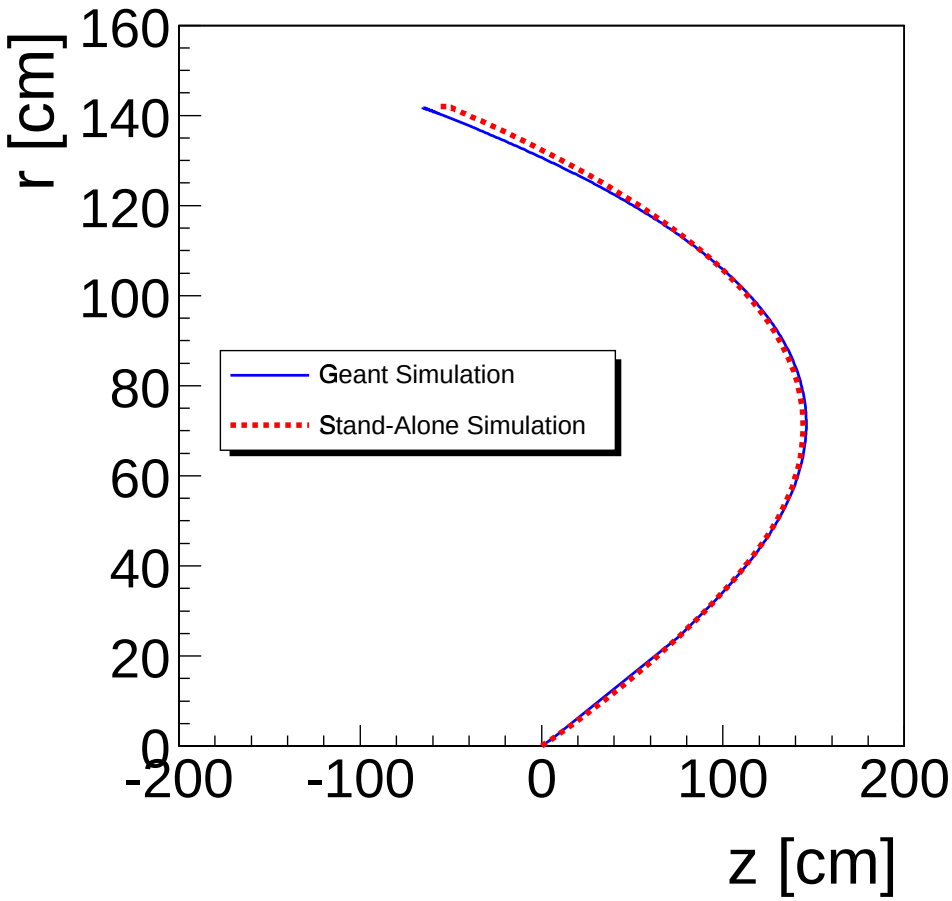

Figure 5-11: The monopole trajectories in r-z for an event with a large z-displacement of 12.0 cm at TOF radius.

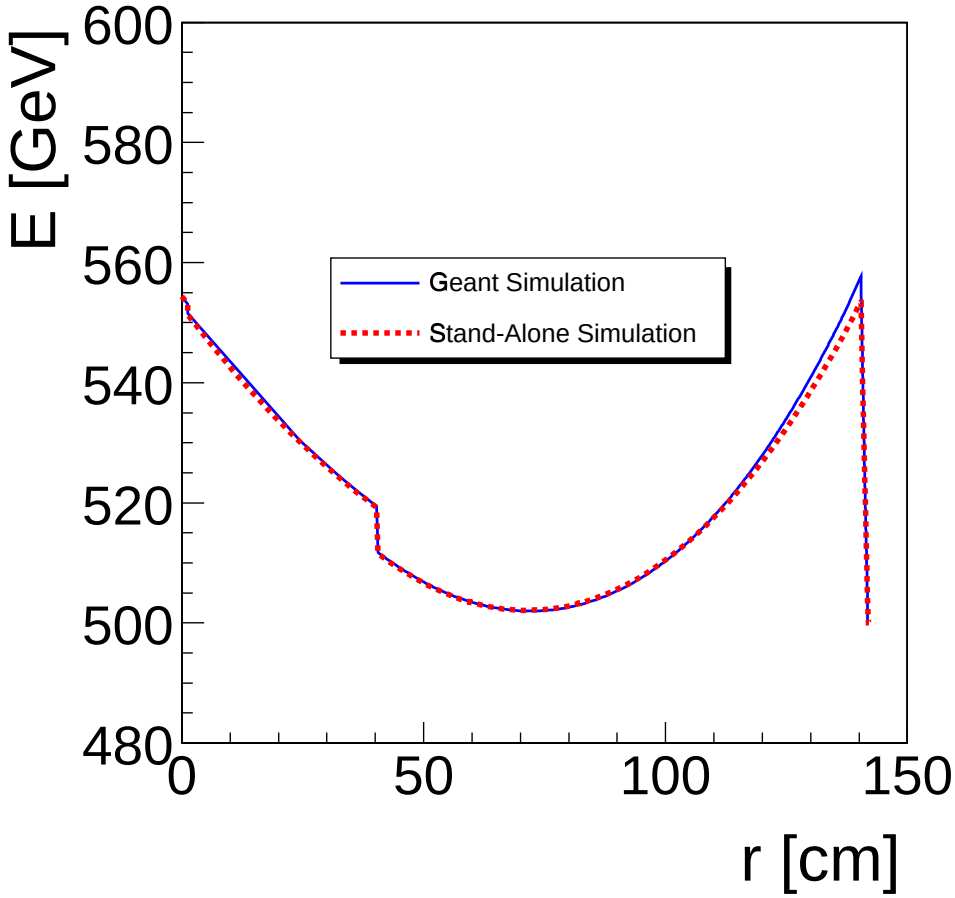

Figure 5-12: The monopole energies versus radial distance for Figure 5-11.

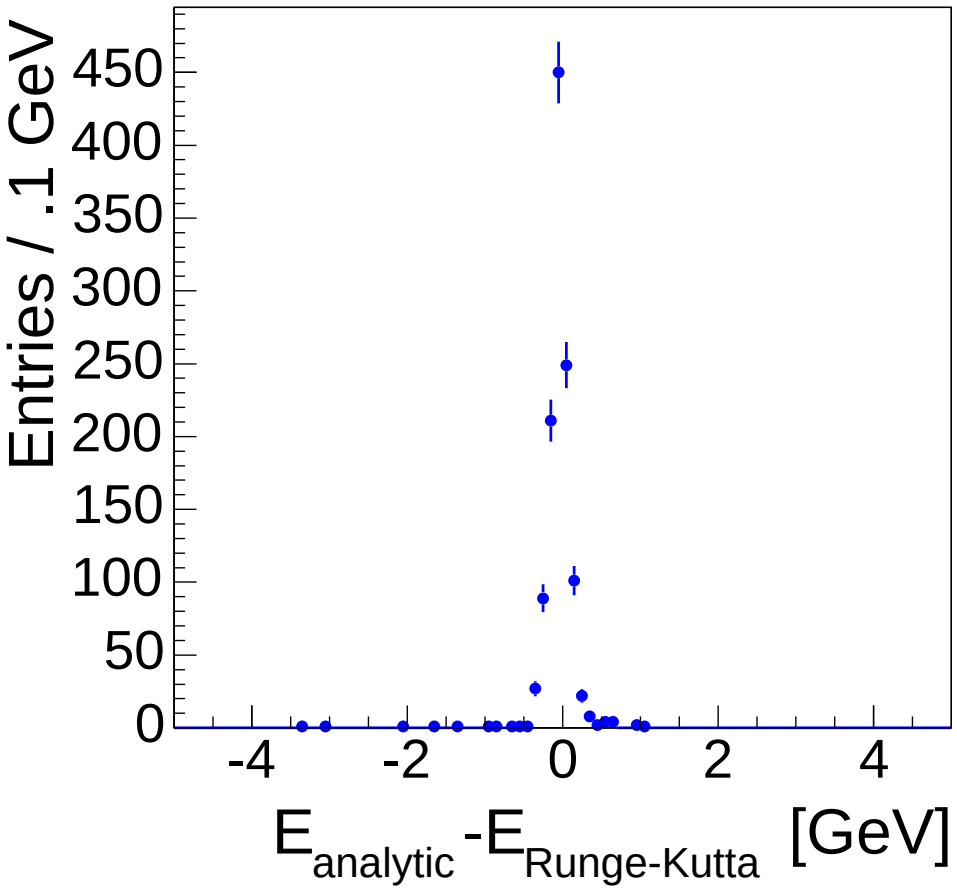

Figure 5-13: The total energy difference at TOF radius for the analytic and Runge-Kutta GEANT implementations.

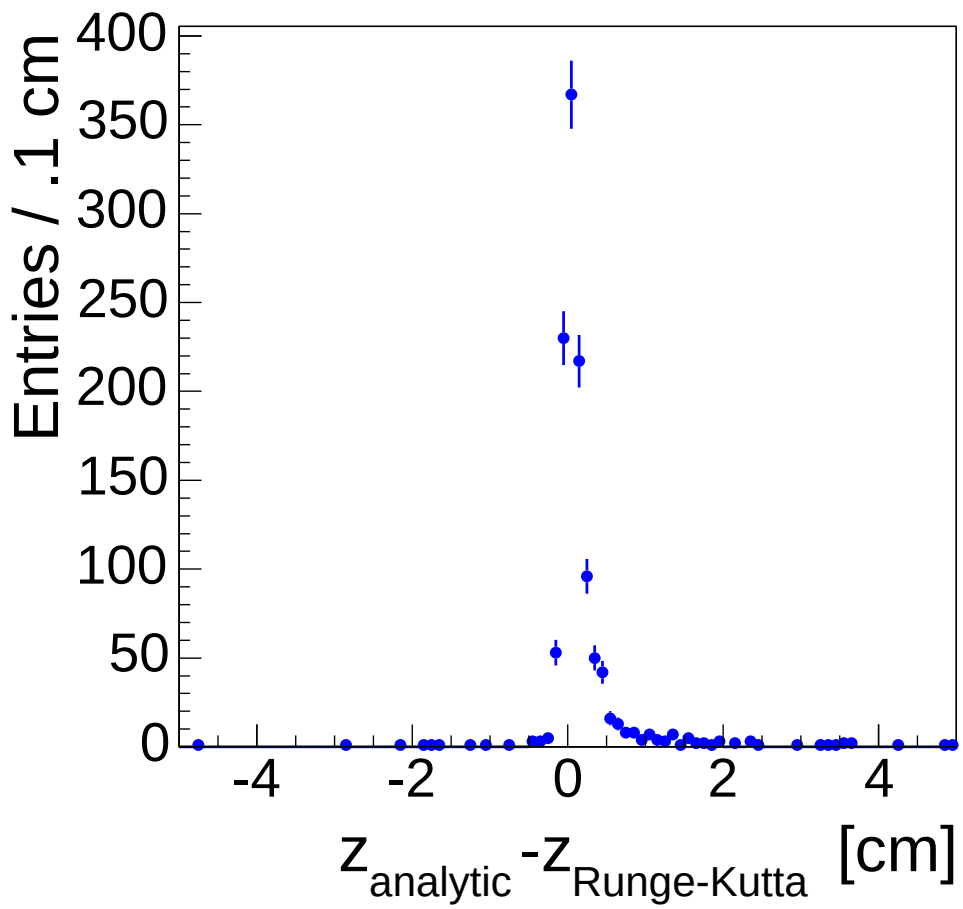

Figure 5-14: The z difference at the TOF radius for the analytic and Runge-Kutta GEANT implementations.

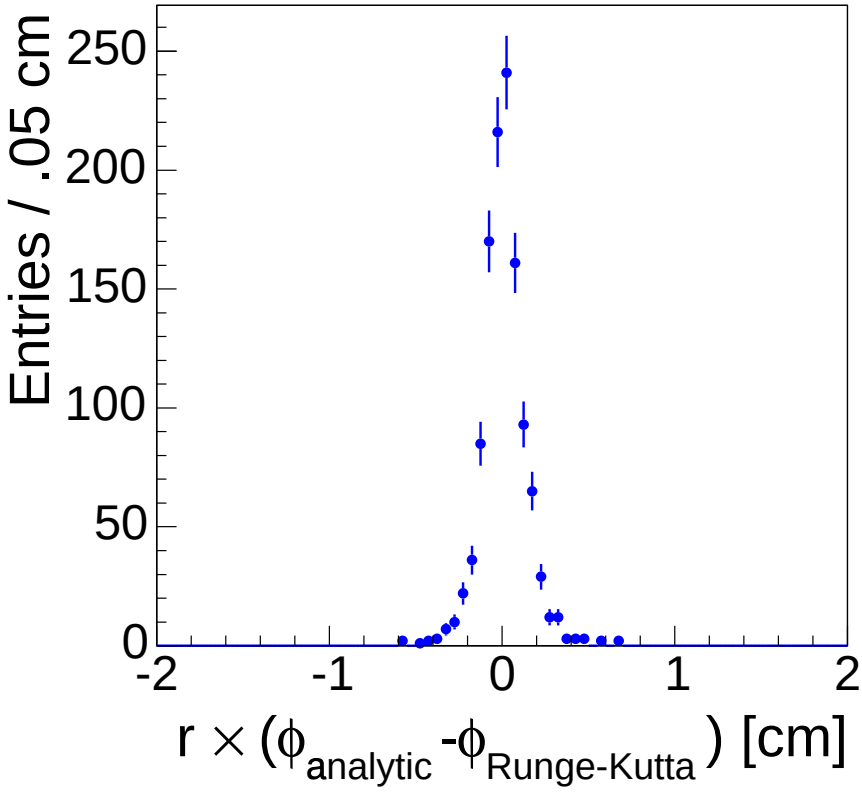

Figure 5-15: The ϕ difference at the TOF radius for the analytic and Runge-Kutta GEANT implementations.

Chapter 6

Trigger Efficiency and Dataset

The main feature of the analysis is the highly efficient dedicated monopole trigger, which requires a coincidence of large pulses from both sides of a Time-of-Flight scintillator bar. Due to their large ionization and massive production of delta rays, monopoles in scintillator with $\beta > 0.2$ are expected to produce light in excess of 500 MIPs. This is a tiny fraction of their overall energy loss, but it still represents a robust signal [6, 35]. Understanding the efficiency of the highly ionizing particle (HIP) trigger on monopoles is central to this analysis.

The trigger is allowed to consume 0.5 Hz of CDF bandwidth. We have demonstrated that we can control the rate while remaining efficient. In fact, we choose to keep the thresholds low enough to continuously exercise the trigger.

6.1 Acceptance

No other particle mimics the parabolic trajectory of a monopole, so the TOF acceptance must be estimated from Monte Carlo, which requires the modifications to GEANT discussed in the previous chapter.

Figure 6-1 shows the TOF acceptance, measured using a modified version of GEANT, for the Drell-Yan like production mechanism described in Section 2.5. Light monopoles, accelerated severely by the magnetic field, tend to be swept out along the beam-pipe. Heavy monopoles, produced near threshold with limited kinetic energy

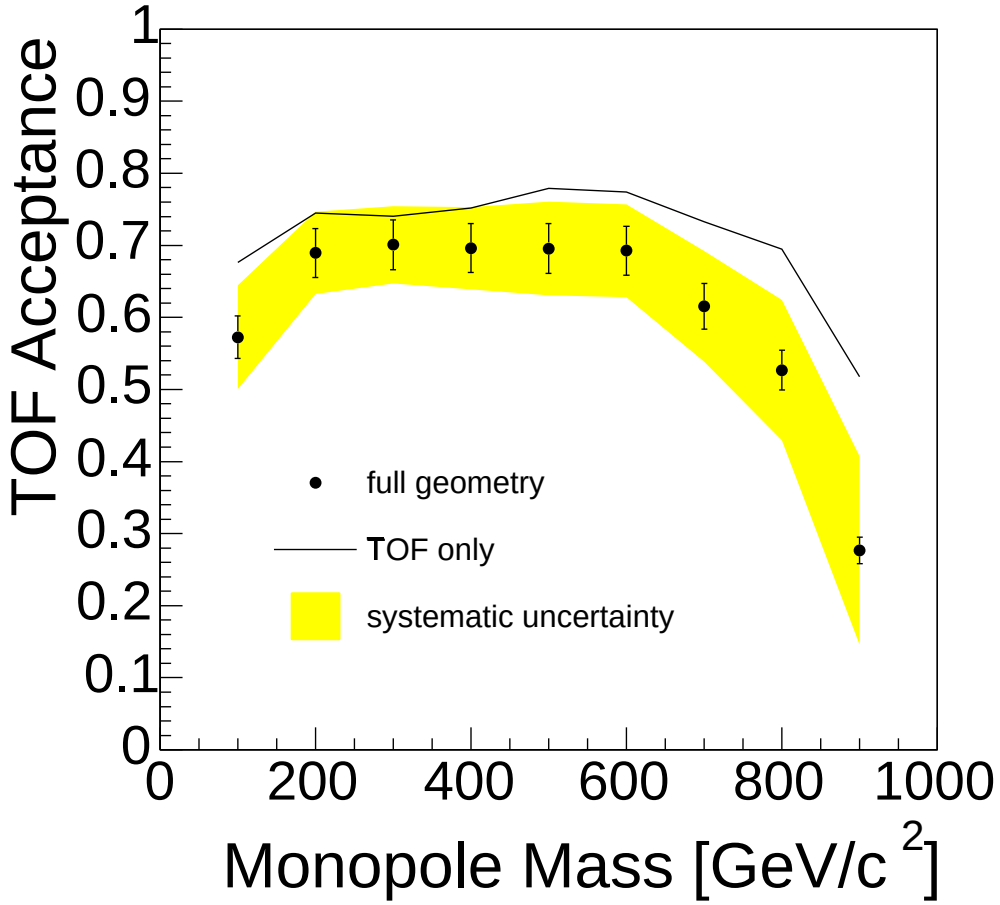

Figure 6-1: The acceptance of the TOF for monopoles, measured using a modified version of GEANT, for the Drell-Yan like production mechanism. Light monopoles, accelerated severely by the magnetic field, tend to be swept out along the beam-pipe. Heavy monopoles, produced near threshold with low kinetic energy and little p_{T}, suffer the same fate. The presence of material in the detector lowers the acceptance, due to energy loss and multiple scattering effects, and is more severe for higher masses.

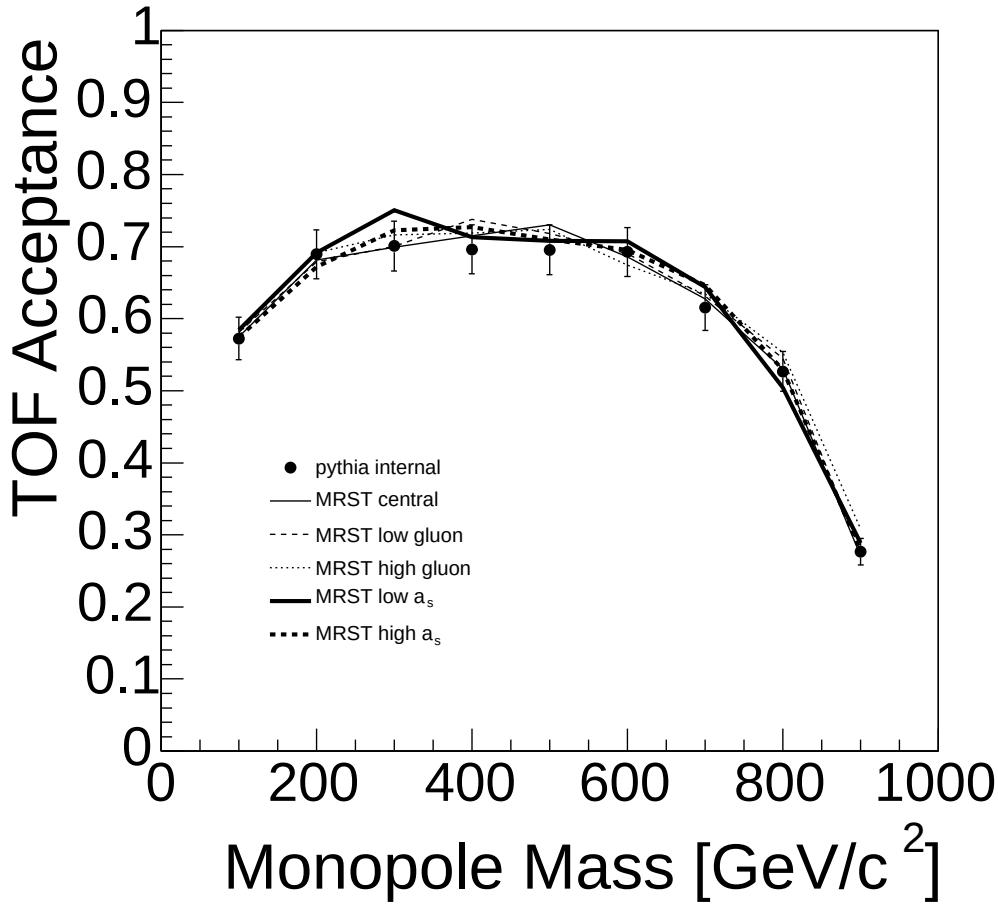

Figure 6-2: The acceptance of the TOF varying the parton distribution function.

and small p_{T}, suffer the same fate. The peak efficiency occurs for the intermediate masses, but the lower efficiency for low-mass monopoles has little effect on the sensitivity, as the production cross section increases for smaller mass.

Figure 6-1 also compares a full simulation of the detector with a fictitious configuration consisting solely of the TOF. The material in the detector lowers the acceptance, due to energy loss and multiple scattering, but is a small correction to the main effect of the magnetic field. The main systematic uncertainty to the acceptance is due to the monopole's interaction with material, which cannot be validated on data. We assign a systematic uncertainty of one half the total estimated effect of the material interactions; for intermediate masses, the systematic uncertainty is 4%.

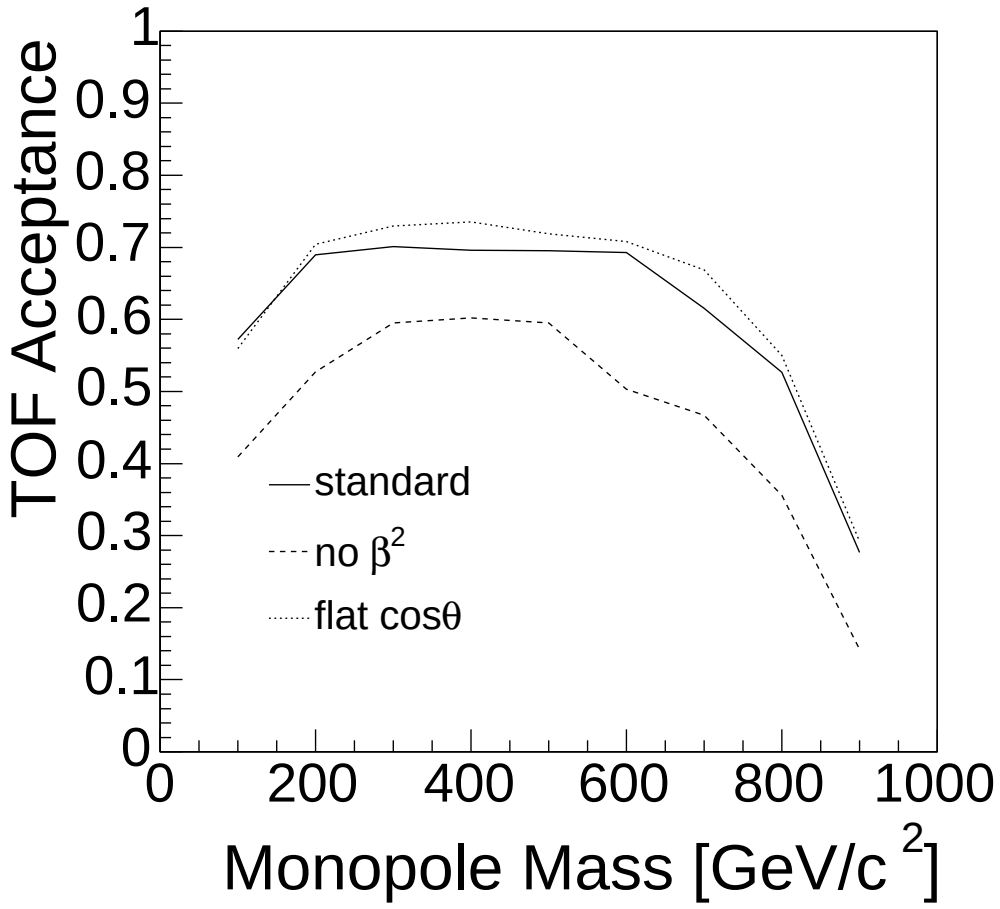

Figure 6-3: The acceptance of the TOF for monopoles using different kinematic distributions.

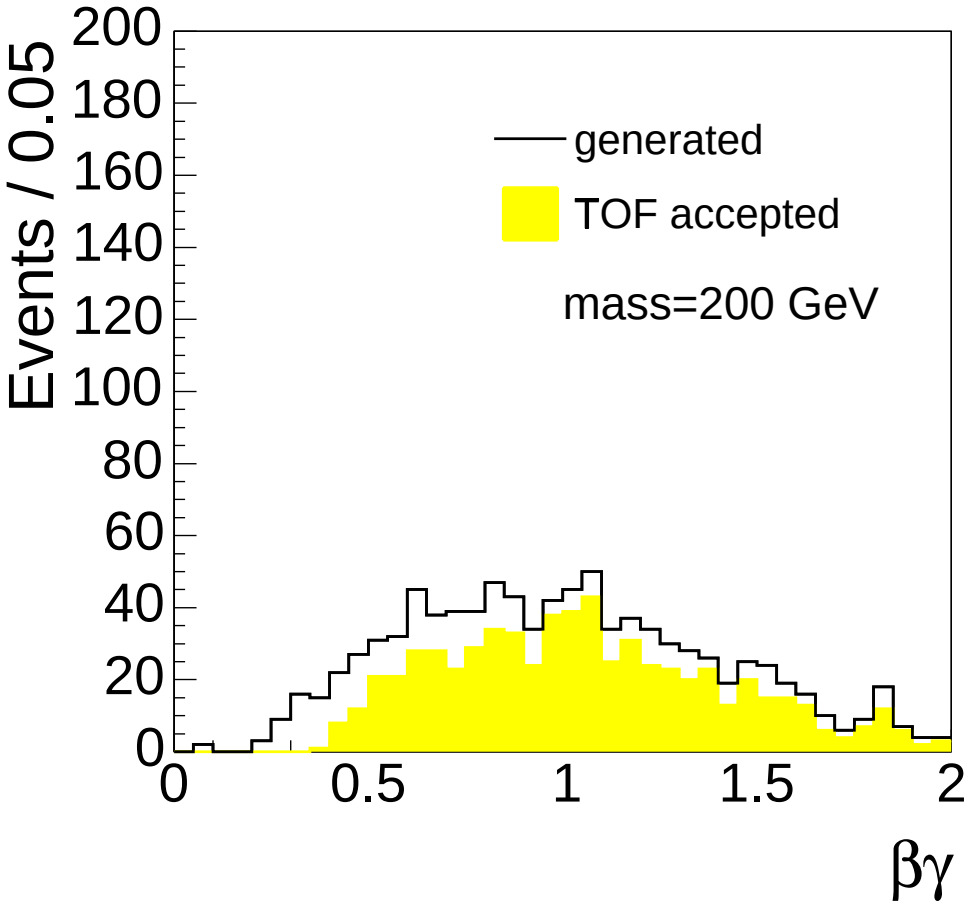

Figure 6-4: The $\beta\gamma$ distribution for generated and TOF-accepted monopoles with $m = 200$ GeV.

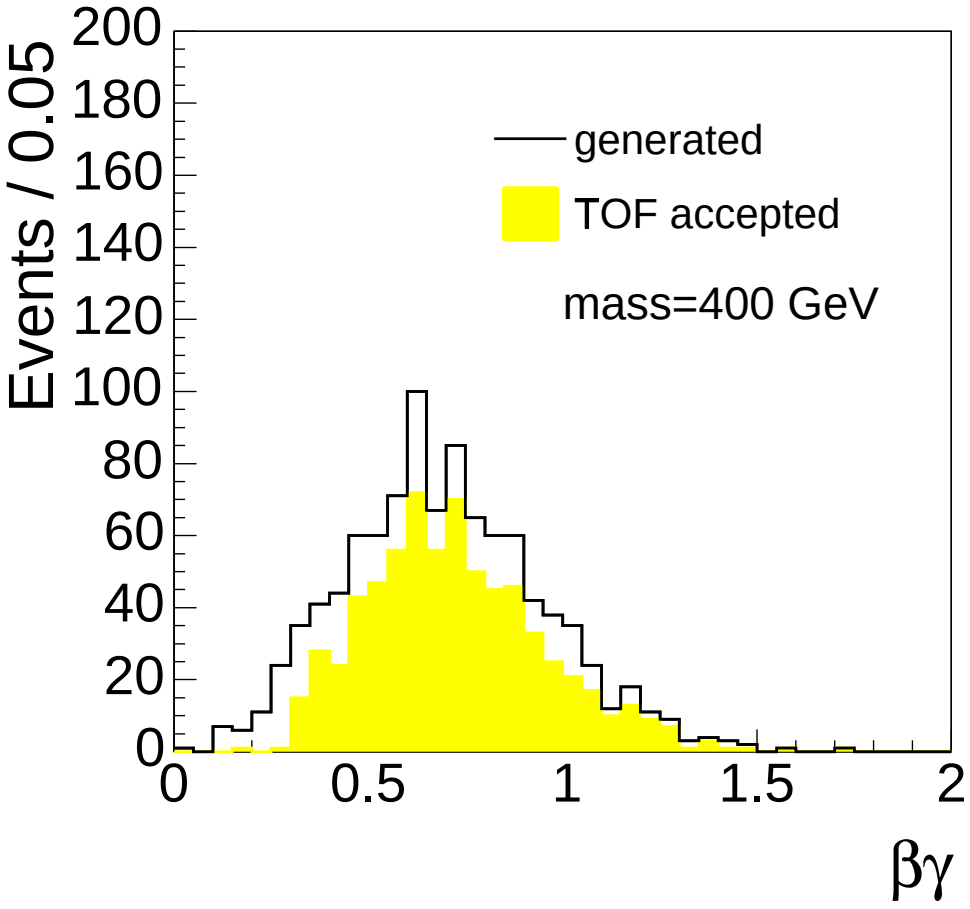

Figure 6-5: The $\beta\gamma$ distribution for generated and TOF-accepted monopoles with $m = 400$ GeV.

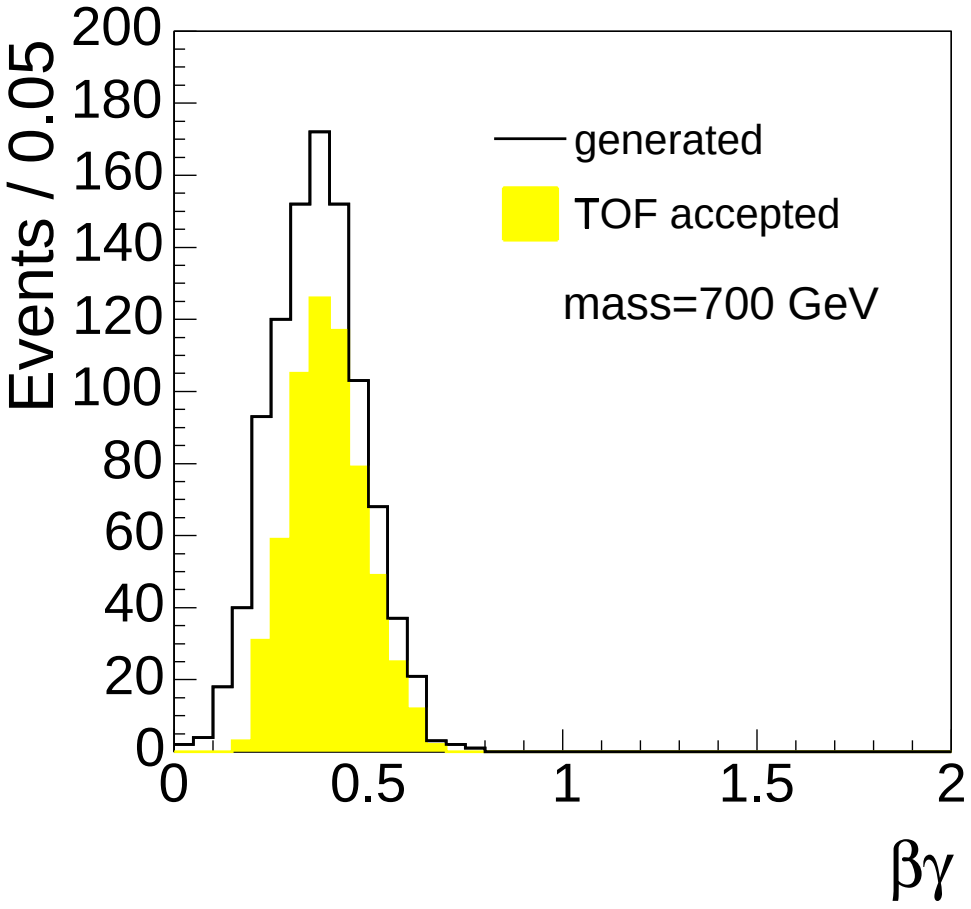

Figure 6-6: The $\beta\gamma$ distribution for generated and TOF-accepted monopoles with $m = 700$ GeV.

The acceptance depends on the kinematics of the production model, but not the overall scale. To ensure the results are applicable to other pair production models, the TOF acceptance is measured for alternate kinematic distributions. The kinematics come from three main effects: the parton behavior of the quarks, the extra β^2 term for electric-magnetic interactions, and the angular dependence of the monopole pair from their spins. As is seen in Figure 6-2, varying the parton distribution function is a negligible effect. In Figure 6-3, the TOF acceptance without the extra β^2 dependence and for a flat $\cos\theta$ angular dependence is compared with the acceptance of the Drell-Yan like mechanism. For the intermediate masses, there is a 10% difference, and so we assign one half of this effect, or 5%, to the systematic uncertainty for the kinematic model. Added in quadrature with the material interaction systematic, the total systematic error on the acceptance for intermediate masses is 6%.

The Monte Carlo models all TOF bars as fully operational. The acceptance must be scaled to account for problematic bars. For our data set, there were 3 bars with hardware problems out of 216, giving a scale factor:

$$\epsilon_{coverage} = \frac{216 - 3}{216} = 0.986$$

It is instructive to compare the kinematic distribution of generated monopoles to TOF-accepted monopoles. The $\beta\gamma$ distribution for $m = 200$, 400, and 700 GeV monopoles is shown in Figures 6-4, 6-5, and 6-6. The TOF requirement eliminates monopoles with low velocities. High-mass monopoles are much less relativistic.

6.2 Electronics Response

The trigger thresholds are chosen to keep the rate of the HIP trigger just below 0.5 Hz. This represents a tiny fraction of the total CDF bandwidth, but constantly exercises the trigger for validation. The rate calibration procedure is an operational matter and is described elsewhere [36]. Here, we calibrate the trigger electronics response and verify that the thresholds used are far below the expected response from monopoles.

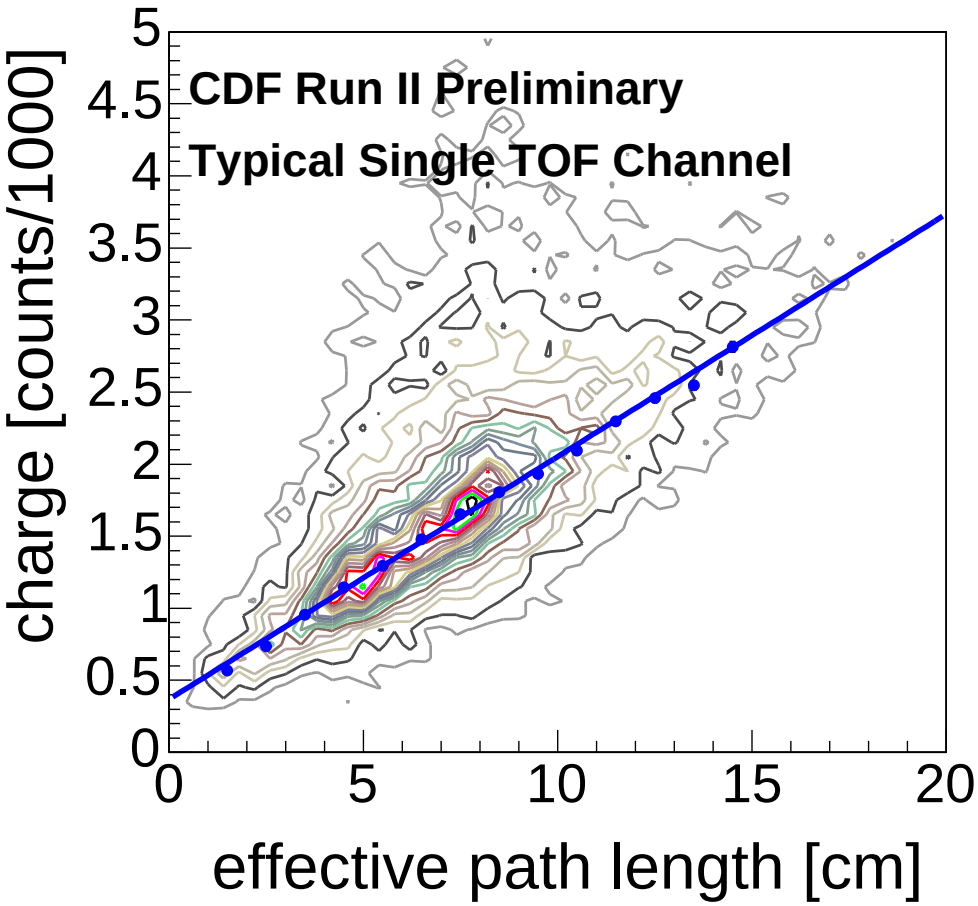

Figure 6-7: Light contributions from multiple tracks are summed, accounting for attenuation, and compared to the measured TOF charge. A binned fit to the Landau distributed charge shows a linear response from zero to four MIPs.

The TOF's response in the low charge region is calibrated using ordinary tracks. The light, L, arriving at a PMT depends on the tracks path length in the bar, s, and the distance from the center of the bar, $\pm z$:

$$L = L_0 \cdot s \cdot exp(\pm z/\lambda) \cdot exp(z^2/k)$$

L_0 is the normal light output for a $z = 0$ track per path length in bar, λ is the attenuation length in the bar, and the $\pm$ refers to east or west PMTs. The z^2/k term is an observed effect suggesting reflections at the ends of the bar [37]. The light arriving at a PMT is proportional to the effective path length, s_{eff}, which is the sum of path lengths from individual tracks corrected for the attenuation effects:

$$s_{\text{eff}} = \sum_{tracks} s \cdot exp(\pm z/\lambda) \cdot exp(z^2/k)$$

The light yield is a Landau distribution with most probable value $L_0 \cdot s_{\text{eff}}$. Plotting the measured charge as function of s_{eff} measures the response function of the TOF. This is shown in Figure 6-7. Each bin in s_{eff} is fit to a Landau distribution; the most probable values are the points, and the line a linear fit.

A one MIP signal has a most probable value corresponding to a single track passing straight through the 4 cm bars, at the center of the bar. The charge versus effective path length plot reveals a linear response of the TOF from 0 to 4 MIPs, or 0 to 16 cm. In this low charge region, we can now convert raw ADC counts to MIPs. This correction has been applied to the data shown in Figure 6-8 and fit to two Landau functions, Φ, with width σ_i, peak values Q_i, and signal fraction S_i plus a correction term for clipped bars, g, taken from [37]. The probability p used for the likelihood fit is given by:

$$\begin{aligned} p(Q) = S_1 \cdot \Phi((Q - Q_1)/\sigma_1) + S_2 \cdot \Phi((Q - Q_2)/\sigma_2) \\ +(1 - S_1 - S_2) \cdot g(Q; Q_1, \sigma_1) \end{aligned}$$

Figure 6-9 shows the TOF threshold values for East and West PMTs in units of

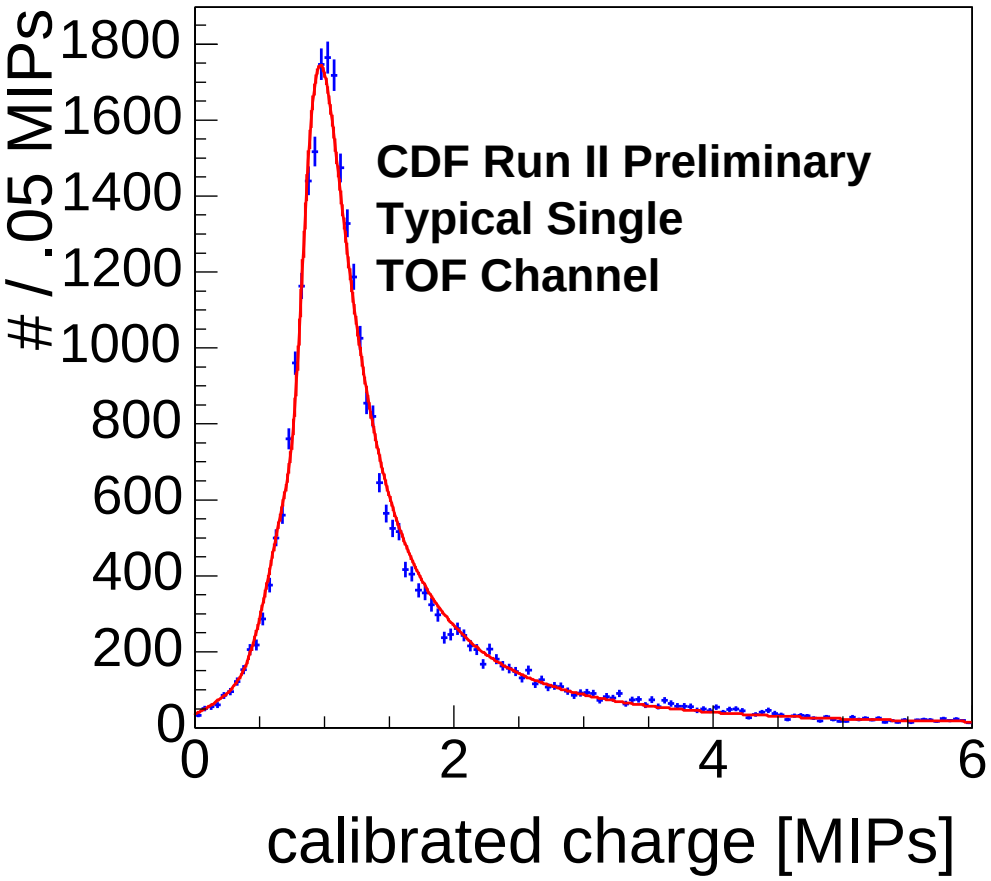

Figure 6-8: The calibrated charge distribution for a typical TOF bar.

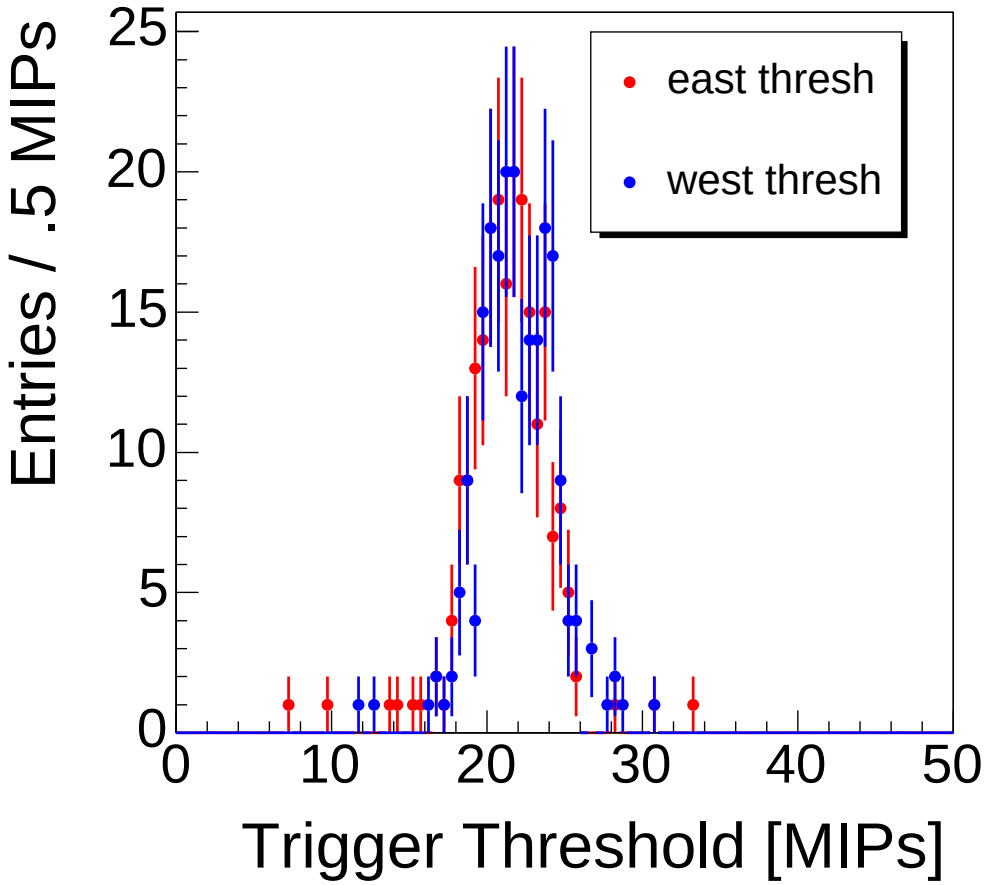

Figure 6-9: The trigger thresholds calibrated in MIPs. This does not include the non-linear effects of the TOF electronics considered below.

the energy deposited by a single MIP. They are all around 20 MIPs. The calibrated region only extends to four MIPs.

To extend the calibrated region, we use the TOF's laser calibration system, which injects laser light into the TOF's bars through fiber optic cables. The optical coupling to the laser varies from bar to bar, but is linear with laser intensity. For the calibration, we pair a strongly coupled bar with a weakly coupled bar, and vary the intensity of the laser. The weakly coupled reference bar remains in its linear region, and is used as a linear scale. The strongly coupled bar is in its linear region for low intensities, passes through a non-linear transition, and returns to linearity at a lower gain, as demonstrated in Figure 6-10.

From the original calibration in Figure 6-7, the response of the strongly coupled bar is known at low intensities, which is used to scale the laser fit and obtain a true response function, as shown in Figure 6-11. The trigger thresholds is now seen to be well inside the second linear region.

By setting the initial linear region to a slope of 1, the non-linear response is compared from bar to bar. This is essentially a correction factor for the effect of the gain switching. The response of three PMTs shown in Figure 6-12 is nearly identical, as expected from test stand measurements of the TOF electronics [26]. The overall effect of the gain switching is that the nominally 20 MIP thresholds are actually at 30 to 40 MIPs. This has no effect; monopoles would deposit more that 500 MIPs of light.

The trigger thresholds are much smaller than the expected response to a monopole, therefore the inefficiency due to the trigger thresholds is negligible. We assign an efficiency of 100% with negligible uncertainty to this effect.

6.3 Spoilers

Because the TOF electronics make a single measurement for each photomultiplier tube for each event, tracks arriving early in the TOF bar effectively screen later arriving monopoles. This effect is mitigated by the long charge integration window

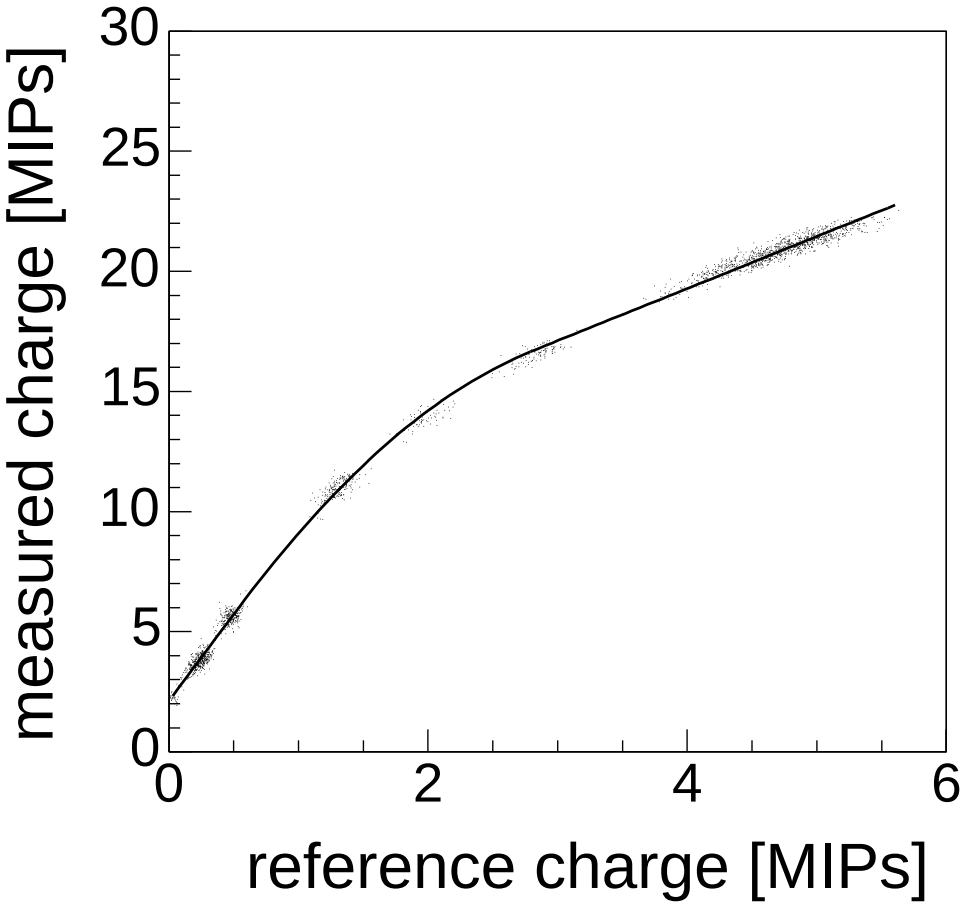

Figure 6-10: The non-linear response of a TOF PMT measured using the laser calibration system. The charge measurement of a weakly coupled PMT (along x axis) is used to provide a linear scale, since the charge is never outside it's linear region. The charge response of a strongly coupled bar (along y axis) exhibits the expected behavior: an initial linear region, a transition region, and second linear region at a new low gain is observed and fit.

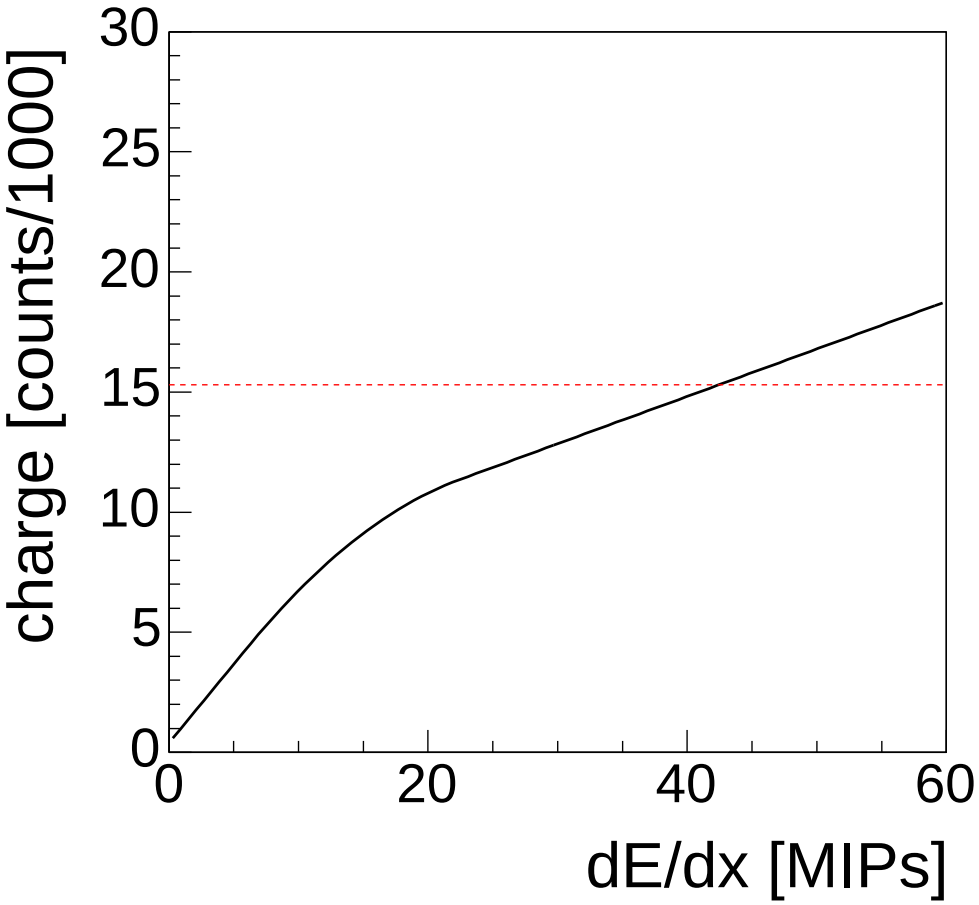

Figure 6-11: The non-linear response obtained from the laser calibration is scaled using the data calibration of the low charge region to obtain a true response curve. The trigger thresholds are well inside the second linear region.

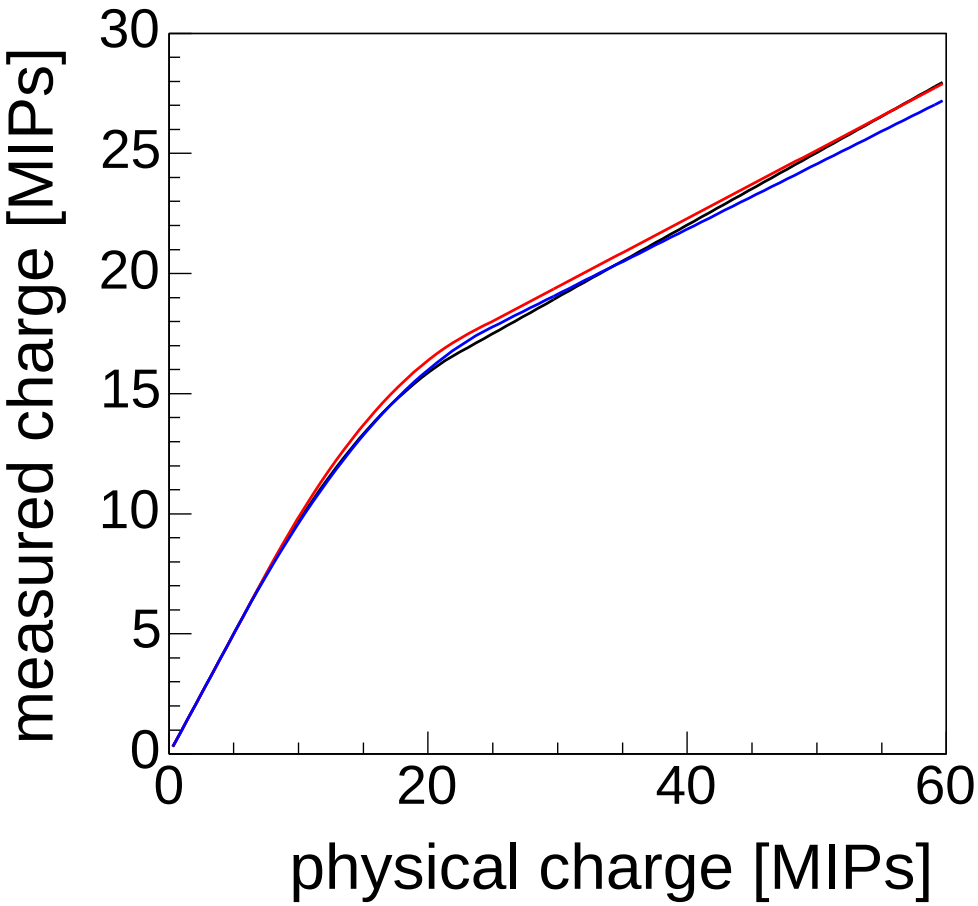

Figure 6-12: By setting the initial gain to one, the non-linear response of different PMTs is shown to be nearly identical. This is essentially a correction factor for the non-linear response, meaning that the nominally 20 MIP thresholds are actually at 30 to 40 MIPs. This doesn't have any effect; monopoles produce more than 500 MIPs of light.

($\sim 20\ ns$) used for our data set. This is not true in the more recent data (since run 168766) which is not considered in this analysis.

It is believed that the higher than expected occupancy of the TOF is due to calorimeter back-splash. In principal, we could use nearly any sample to measure this effect, since the back-splash is not correlated with the underlying event. However, we choose to use $Z \to e^+e^-$ events, which have an underlying event similar to monopole pair production. Also, the high p_{T} electrons mimic the $r - \phi$ non-curvature of monopoles, meaning that we can check for the presence of spoilers in the electron bars to estimate the effect for monopoles. Each end of a TOF bar—the east and west—is instrumented with a PMT. For events with spoilers, the two pulses are inconsistent with the z position of the track.

We apply the standard central electron Z cuts [38] to the Z data sample `btop0j` and obtain the e^+e^- events with invariant mass distribution shown in Figure 6-13. We make our measurement on the loose electron, which does not have an isolation cut. For each electron, we extrapolate its trajectory to the TOF, and record any pulses from the TOF for the hit bar. We convert the pulse time at the PMT to an arrival time at the bar using the z position of the track and the known speed of light in the bar.

The difference between the east and west arrival time measurements versus z is shown in Figure 6-14. Consistent events form the central band, with the width determined by the timing resolution. Spoilers form the parallelogram with size equal to the optical length of the bar (~ 20 ns). The shape comes from the fact that the phase space for a spoiler between a track and the PMT vanishes as the track gets close to the PMT. A likelihood fit including resolution and spoiler contributions measures the spoiler fraction at 14%.

The dependence of the spoiler fraction on luminosity is shown in Figure 6-15; one half of the effect is 2%. Because the underlying event from $Z \to e^+e^-$ may be different from monopole pair production, we also measure the dependence on the summed p_{T} of all tracks in the event, as shown in Figure 6-16. One half of the effect is 4%. Finally, our fit doesn't completely disentangle resolution effects from spoiler effects, due to

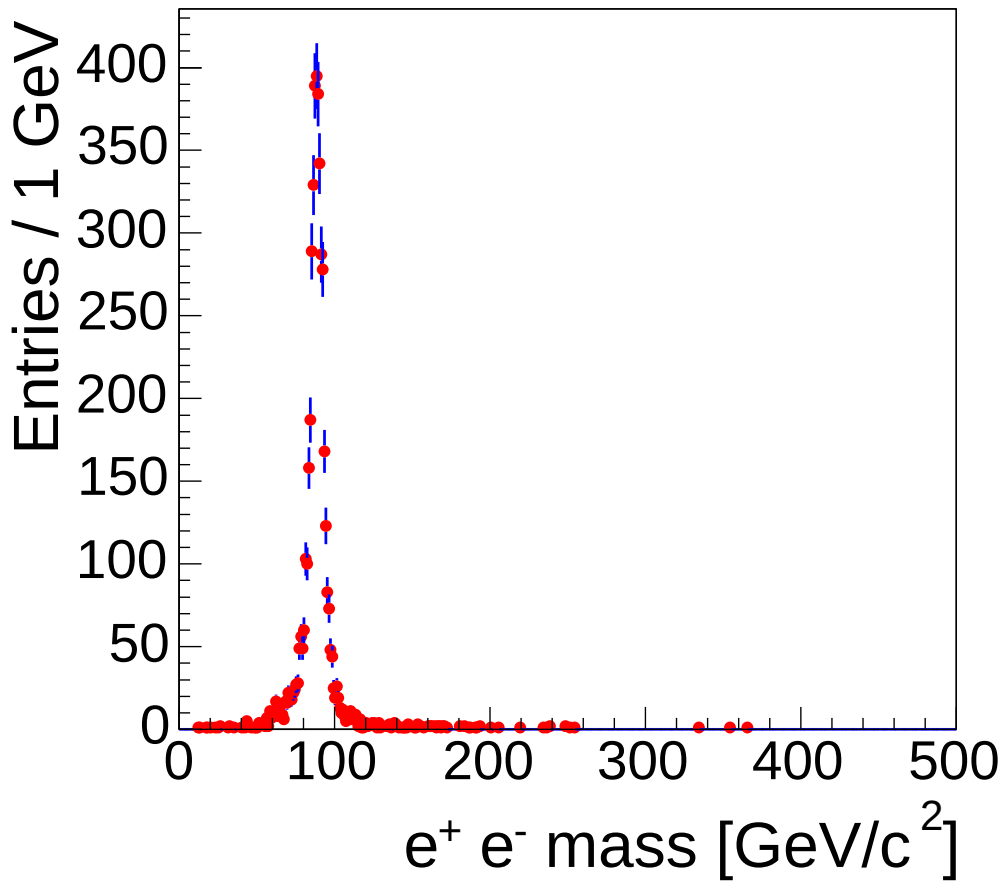

Figure 6-13: The invariant mass of the e^+e^- system using the standard Z electron cuts. The underlying event from Z pair production should be similar to monopole pair production.

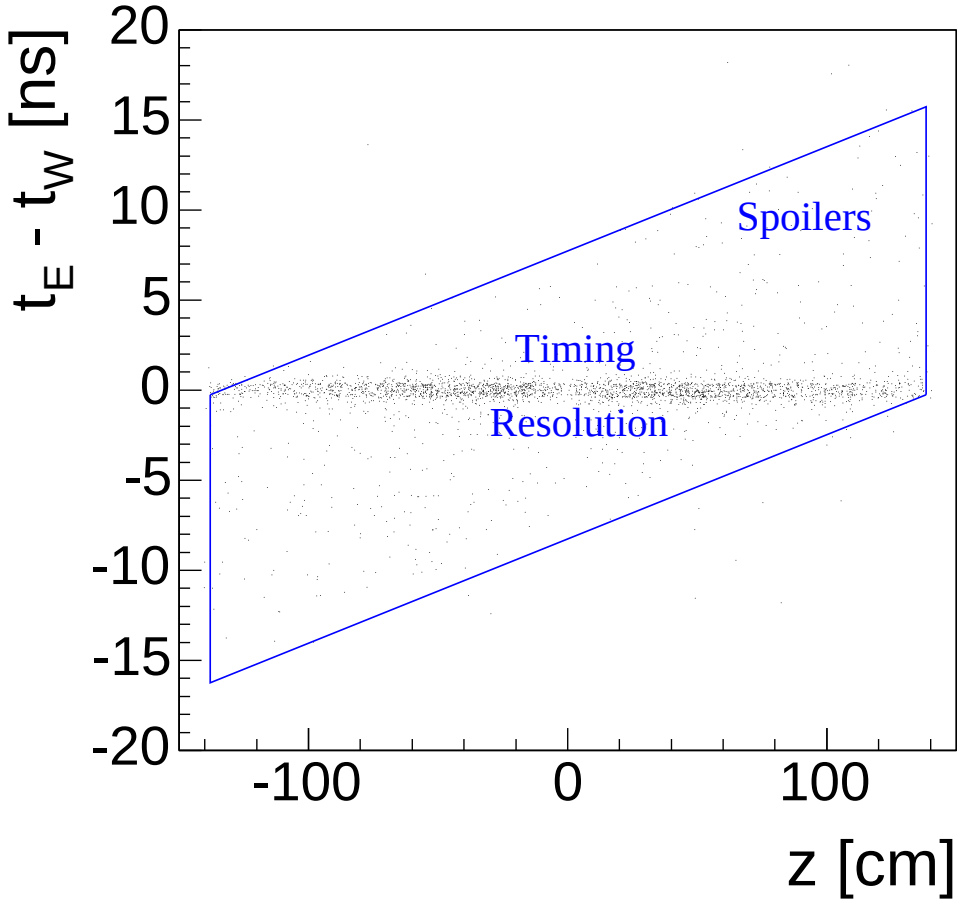

Figure 6-14: The east minus west arrival time measurement versus track z position. Consistent events form the central band, with the width determined by the timing resolution. Spoilers form the parallelogram with size equal to the optical length of the bar ($\sim$ 20 ns). The shape comes from the fact that the phase space for a spoiler between a track and the PMT vanishes as the track gets close to the PMT. A likelihood fit including resolution and spoiler contributions measures the spoiler fraction at 14%.

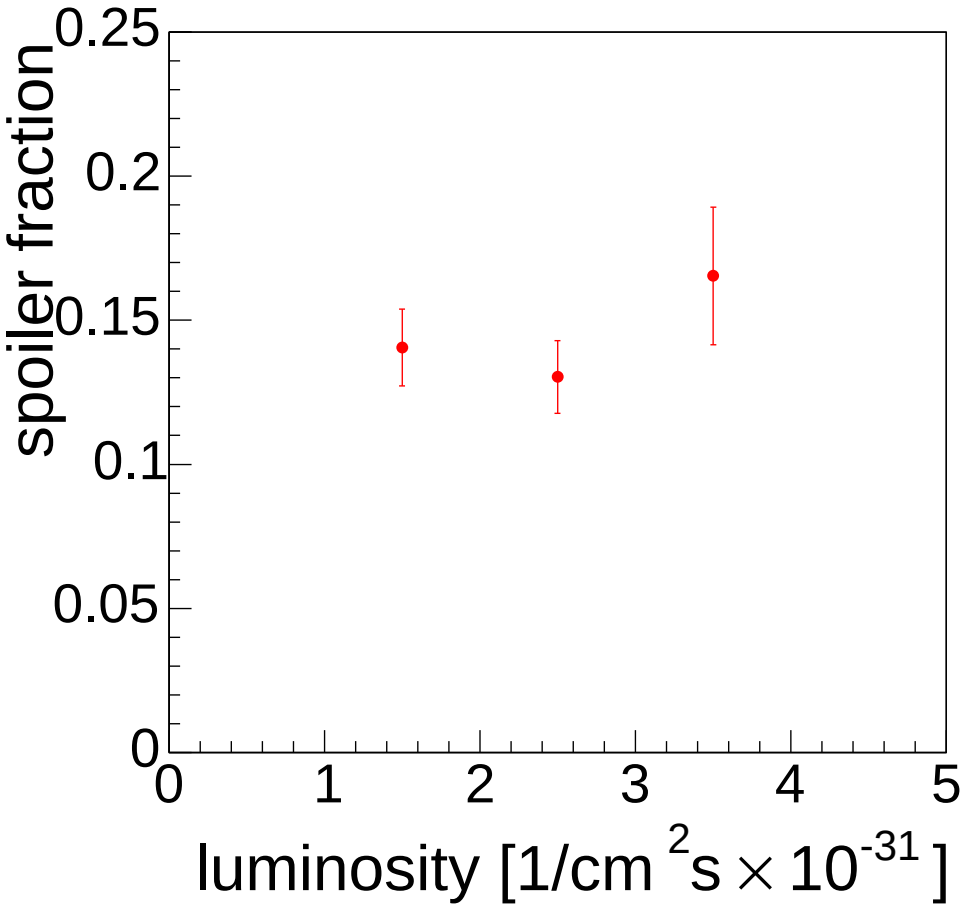

Figure 6-15: The dependence of the spoiler fraction on instantaneous luminosity. There are slightly more spoilers at higher luminosity.

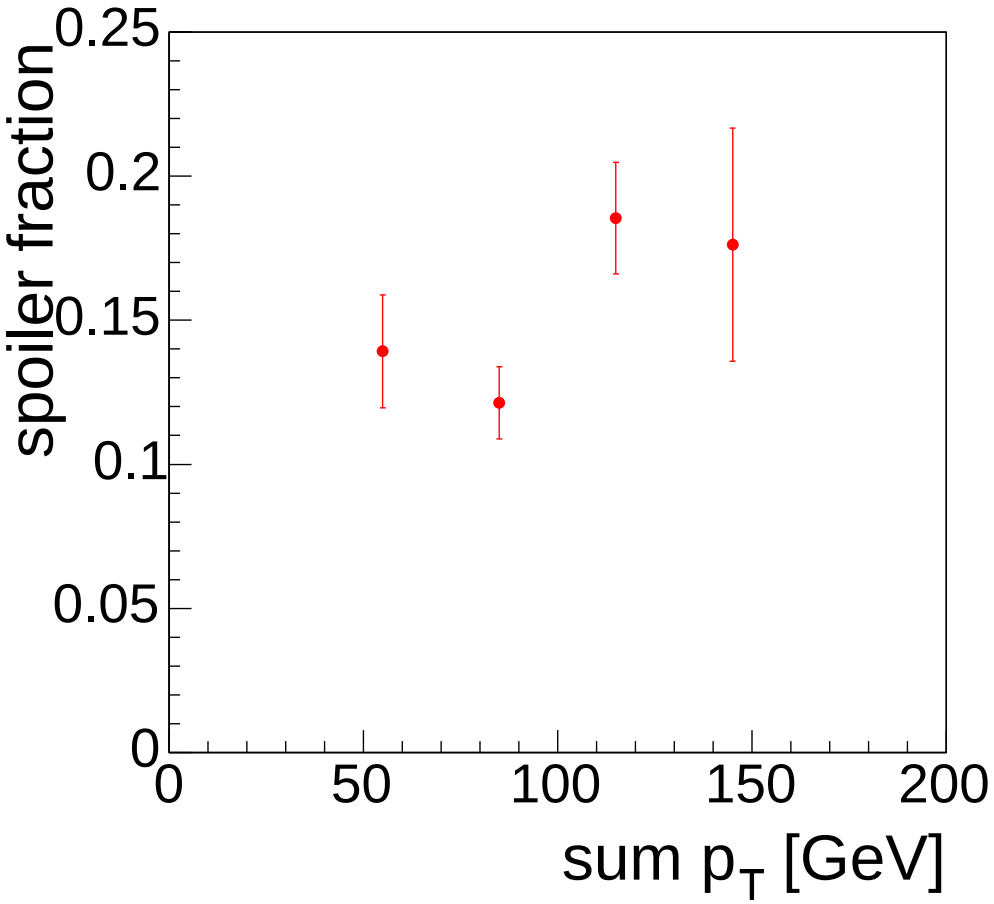

Figure 6-16: The dependence of the spoiler fraction on the the sum p_{T} from tracks in the event. There are slightly more spoilers at higher sum p_{T}.

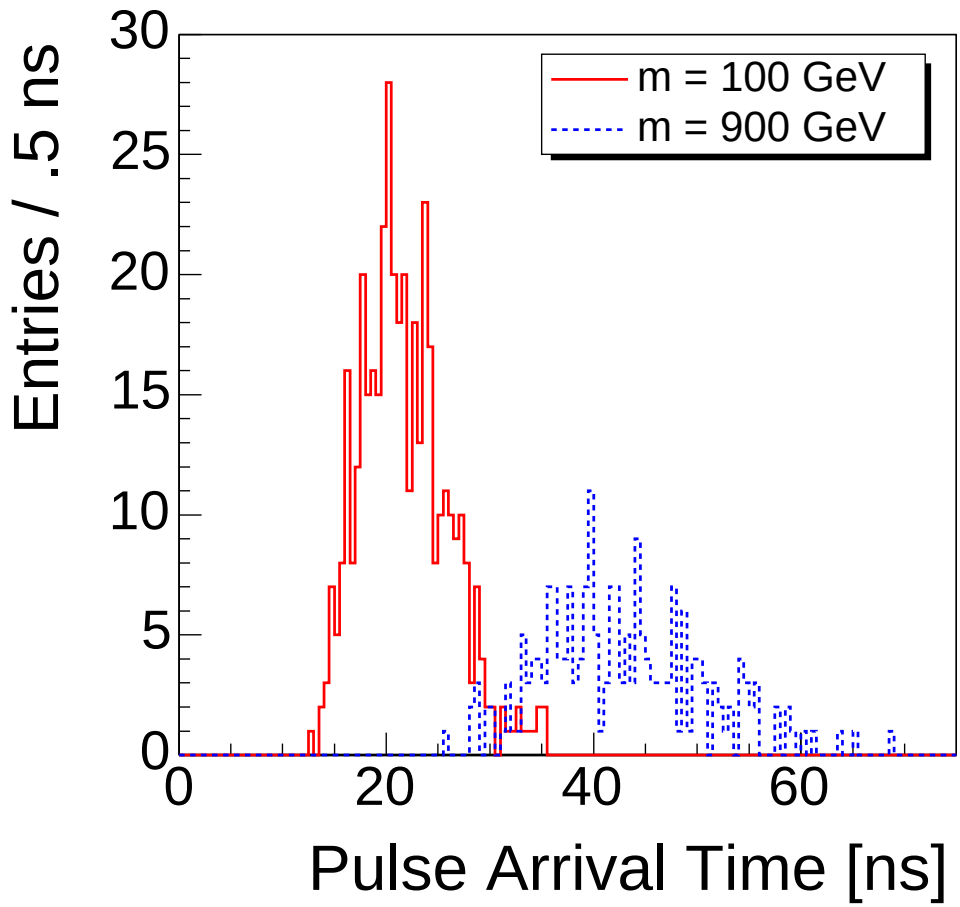

Figure 6-17: The arrival time at the furthest TOF PMT of light pulses from 100 GeV and 900 GeV monopoles, from Monte Carlo.

broad shoulders in the resolution description. To estimate the size of this effect, we fix the broad Gaussian in the resolution description to 500 ns and refit. This is shown to increase the spoiler fraction by 1%. We assign a systematic uncertainty of 5% by adding all of these effects in quadrature.

6.4 Timing

Monopoles are massive, so they can have slow velocities, and arrive at the TOF too late to cause a trigger. Because the trigger requires a coincidence from both the

east and the west PMTs, some pulses must travel the whole distance of the bar, taking 20 ns. The latest pulses from 900 GeV monopoles arrive as late as 70 ns after the collision, as shown in Figure 6-17. To estimate the timing efficiency from these distributions, we need to know the end of the TOF's timing window, which we call the timing edge.

To measure the timing efficiency, the timing edge with respect to the interaction time is needed. This is obtained by first measuring the distance between the timing edge and the arrival of prompt particles, then adding the time of flight of a prompt particle.

The TOF measures the time interval between pulse arrival and a common stop, meaning that earlier arrivals have a larger time measurement. Prompt particles cause the sharp edge to the right of the pulse time distribution shown in Figure 6-18. The width of the central peak is roughly 20 ns, the optical length of the TOF bars. The timing edge comes just before the common stop, revealed by the abrupt end of the late tail. Taking the prompt arrival time at the half maximum value of the prompt edge, the timing window is 54.3 ns. The edge is not perfectly sharp due mainly to the event t_0, but also because there is vanishing phase space for particles to arrive exactly at the PMT. Because our choice of half maximum is arbitrary, we assign an uncertainty from the difference between the time at half maximum to the time at 20% and 80% of maximum, or 2 ns.

The efficiency of the latest pulse (as in Figure 6-17) to reach the PMT within the timing window is shown for a range of monopole masses in Figure 6-19. The systematic uncertainty is dominated by the uncertainty of the timing edge measurement, which is a small effect. It has been added to the statistical uncertainty in the plot.

6.5 Digital Response

The digital part of the trigger is thoroughly validated on minimum bias and trigger data. In both cases, the measured trigger response is in perfect agreement with the emulated response to the digitized data. Thus all our inefficiency comes from the

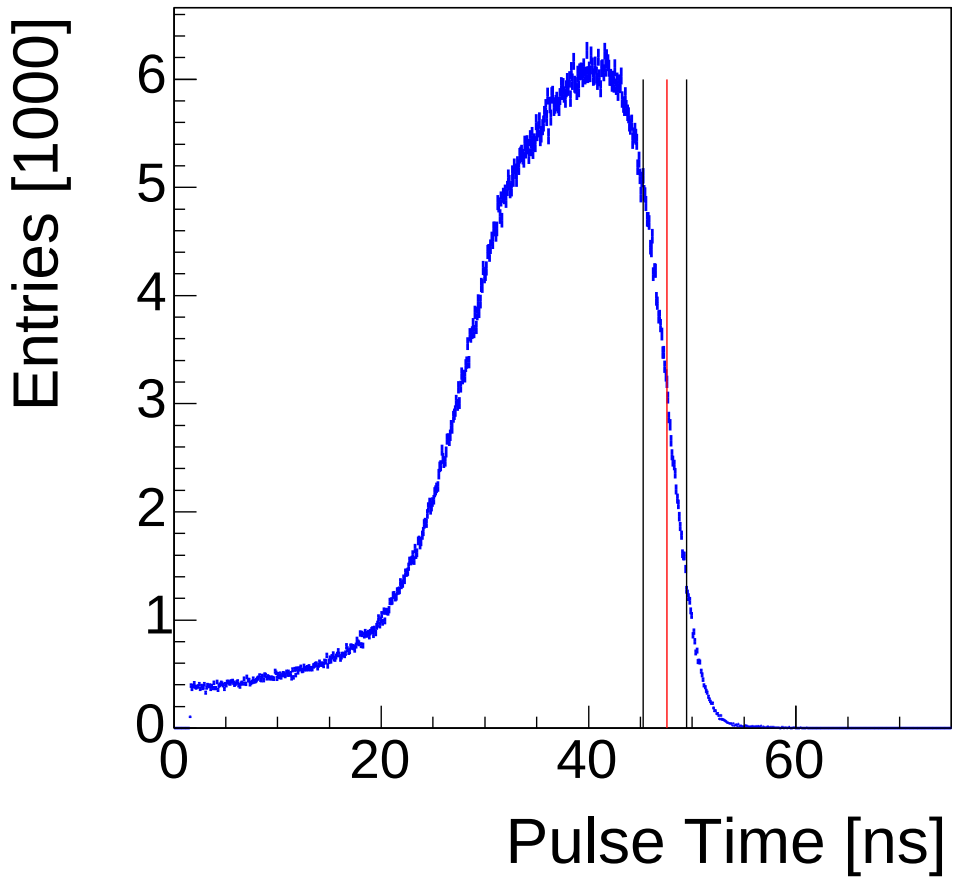

Figure 6-18: The arrival time of pulses to the TOF PMTs. The timing measurement is the time between a PMT going above threshold and a common stop, so earlier arrival times are to the right. The sharp turn on is from promptly arriving particles, the width of the main peak is the optical length of the TOF bars, and the long tail is from slower particles. The sharp cutoff near $t = 0$ is the end of the TOF timing window. This is from 10,000 `jphysc` events.

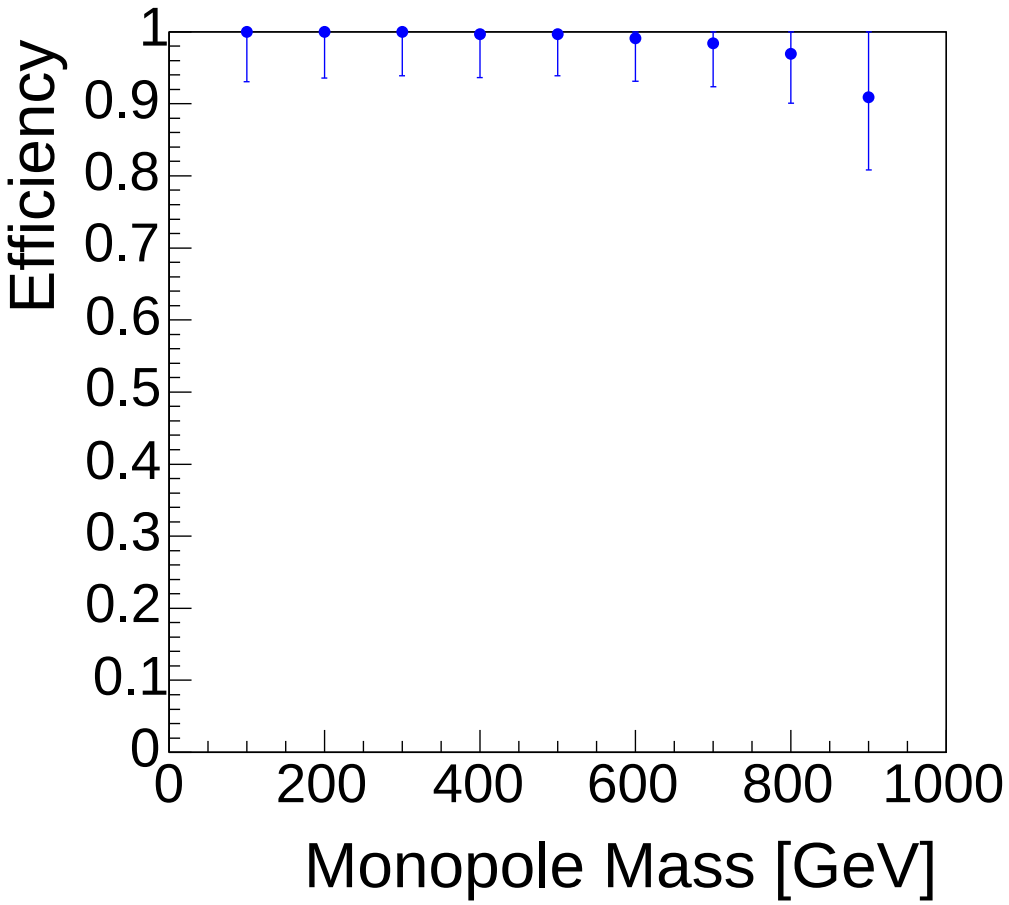

Figure 6-19: The efficiency for both light pulses to reach the TOF PMTs within the timing window, as a function of monopole mass. Only heavy monopoles move slowly enough to be effected.

analog response of the electronics. For the digital response we assign an efficiency of 100% with no uncertainty. Most of the effort for this analysis was to make the trigger work reliably.

6.6 Dataset

The TOF trigger was operational shortly after the summer shutdown of 2003, but the early data did not use calibrated trigger thresholds. The first physics quality data with calibrated thresholds was rate limited; events were thrown out at level 2 if the rate was too high. Even though the average rate was below the threshold, statistical fluctuations at this low rate caused about 20% of the events to be thrown out. The rate limit was removed when the trigger was deemed stable. Shortly before the winter shutdown, the integration window for the TOF's charge measurement was reduced from 20 ns to 12 ns, invalidating the calibrations. This was done to minimize the spoiler effect for typical physics analysis, but actually enhances the effect for the monopole search. For this reason, the most recent data is not considered in this analysis.

The TOF trigger used calibrated thresholds as of run 166011, but the rate limit was not removed until run 166713. At run 168766, the integration window was changed. Our dataset consists of the 25 pb^{-1} of non-rate limited data, and 10 pb^{-1} of rate-limited data. The luminosity measurement has a 6% uncertainty [39].

Chapter 7

Candidate Selection

The signature from a monopole is so unique, a single event could represent a discovery. While deciding how to select monopole candidates from the data sample, we are primarily concerned with not losing any monopoles. If an event passes our cuts there are many additional requirements we can use to determine if it is a monopole. This is not a blind analysis.

The dataset was generating using the dedicated magnetic monopole trigger, which checks for large pulses in the TOF scintillator bars. Offline, we look for abnormally high ionization combined with non-curvature in $r - \phi$, as illustrated in Figure 7-1. We require ϕ_0 coincident COT segments with small curvature. The segments must be composed entirely of large dE/dx hits. These cuts are more than 90% efficient, and completely eliminate ordinary tracks in minimum bias data. But we *do not* claim that only a monopole could pass these cuts. Any candidates will require further scrutiny to determine if they are monopoles.

The COT measures the time interval for which the current on a sense wire is above a threshold, which is an indirect measurement of the amount of ionization from the passing particle. This measurement, called the hit width and measured in nanoseconds, is the offline measurement of ionization used for monopole candidate selection.

The default COT tracking first finds small track segments in each super-layer. We have modified it to ignore hits with widths smaller than an adjustable threshold.

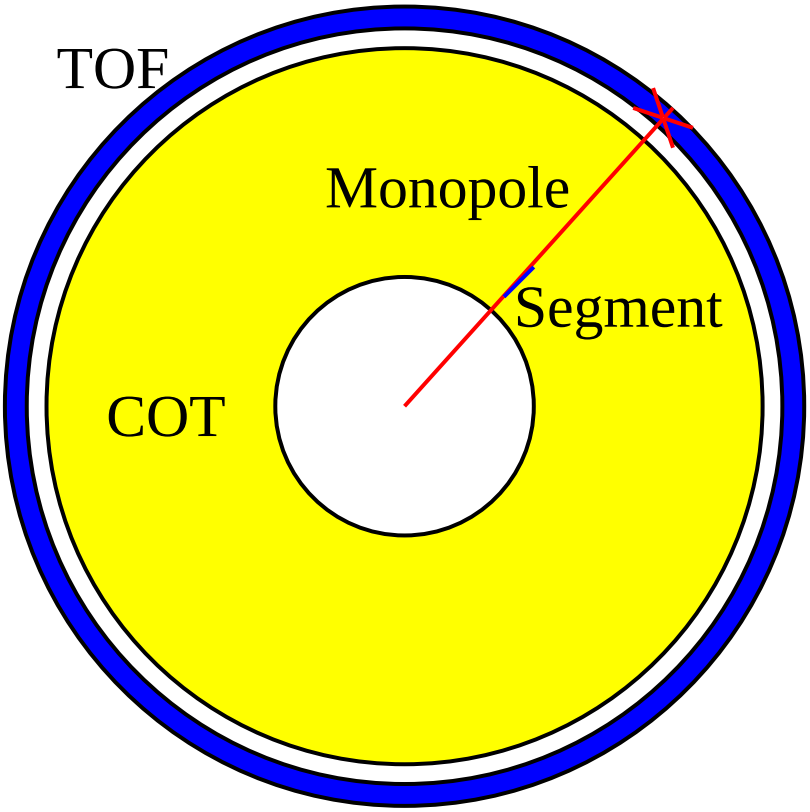

Figure 7-1: Monopoles reach the Time-of-Flight detector, produce hundreds of MIPs of light, and fire the dedicated trigger. Offline, they are detected by many ϕ_0 coincident segments with high dE/dx and low curvature.

Also, because a monopole can have a slow and changing transverse velocity, the usual timing assumption ($t_{\text{flight}} = r/c$) cannot be used. Instead, the time-of-flight to each super-layer is allowed to vary.

With these changes, we check for ϕ_0 coincident low curvature segments in each super-layer. We first calibrate the COT dE/dx measurement for high ionization, choose a width cut, and estimate its effect. Then we remove the width cut, and check the efficiency of our track finding algorithm on high p_{T} tracks. This keeps our dependence on Monte Carlo to a minimum.

7.1 Width Cut

For particles with masses much higher than an electron, the Bethe-Bloch energy loss formula depends only on the velocity. For this reason, the COT dE/dx calibration produces a universal curve [40] that predicts the truncated average width of hits composing a track with velocity β. By adding a mass hypothesis, the same universal curve is used to predict the width's momentum dependence for different particles. This is shown in Figure 7-2 for pions, kaons, protons, and deuterons.

Not surprisingly, the default COT width calibration does not consider the large ionization part of the COT's dynamic range. For this reason, we have added a correction factor by using TOF identified low-momentum protons and deuterons.

The universal curve predicts an output width from a tracks velocity, which combines the COT response with the well understood Bethe-Bloch ionization energy loss. Factoring out the Bethe-Bloch portion reveals the COT response function, which predicts an output width from an amount of ionization, as shown in Figure 7-3. It is logarithmic, exactly as the COT specs (ASDQ) suggest [15].

Using a logarithmic extrapolation, a monopole, which deposits more than 1000 MIPs of energy for $\beta > 0.5$, has a truncated average width of 232 ns, as demonstrated in Figure 7-4. This is still within the dynamic range of the COT, but far outside the range of ordinary tracks. To avoid blindly trusting an extrapolation into an uncalibrated region, we set the width threshold in the tail of the dynamic range from

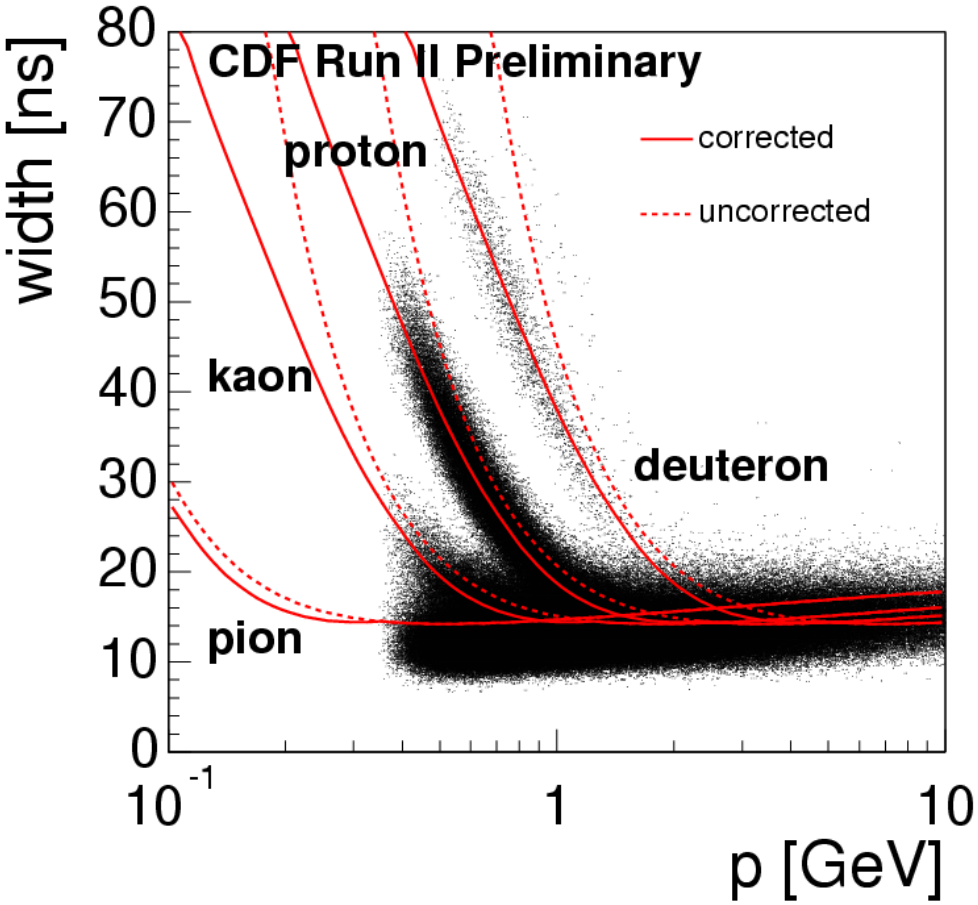

Figure 7-2: The COT dE/dx calibration produces a universal curve, which predicts the truncated average width of hits composing a track of velocity β. For the momentum dependence there are a family of curves; one curve for each mass. For high dE/dx, the default curve fails, so a correction factor has been applied.

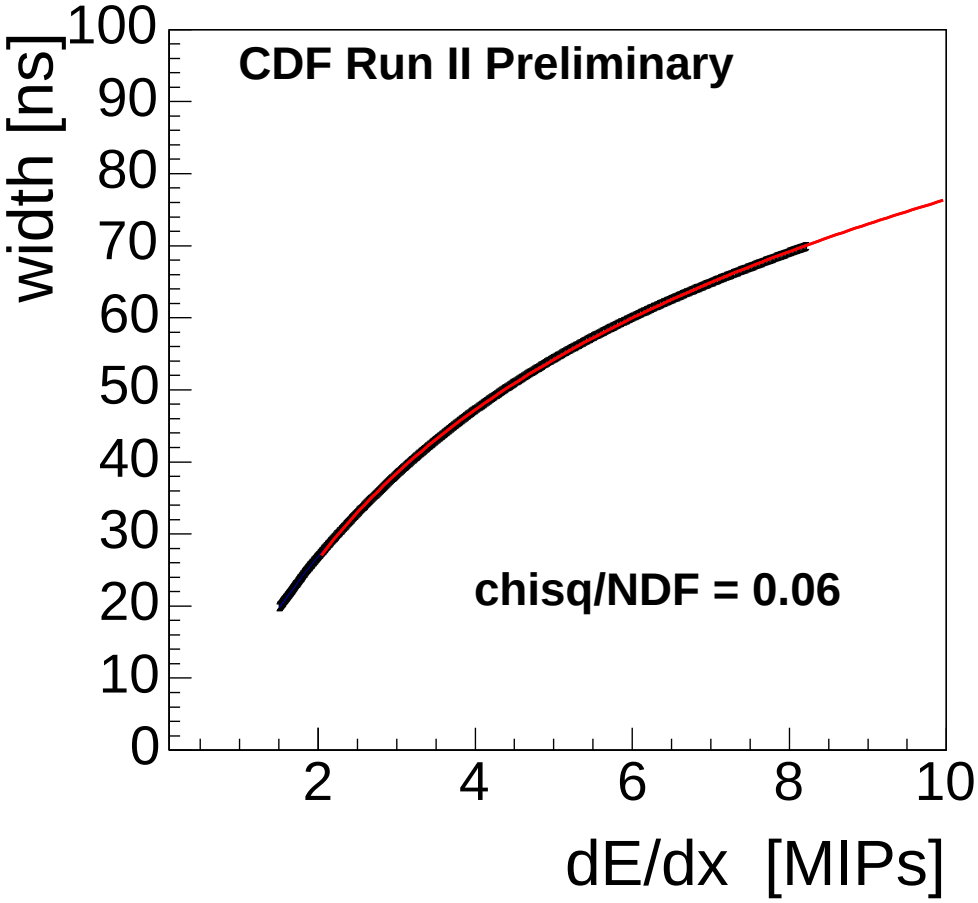

Figure 7-3: The universal curve conveniently combines the ionization of a particle with the electronic response of the COT. We extract the COT response to energy by factoring out the well understood Bethe-Bloch formula. The logarithmic response obtained is exactly as expected from the COT's ASDQ specifications.

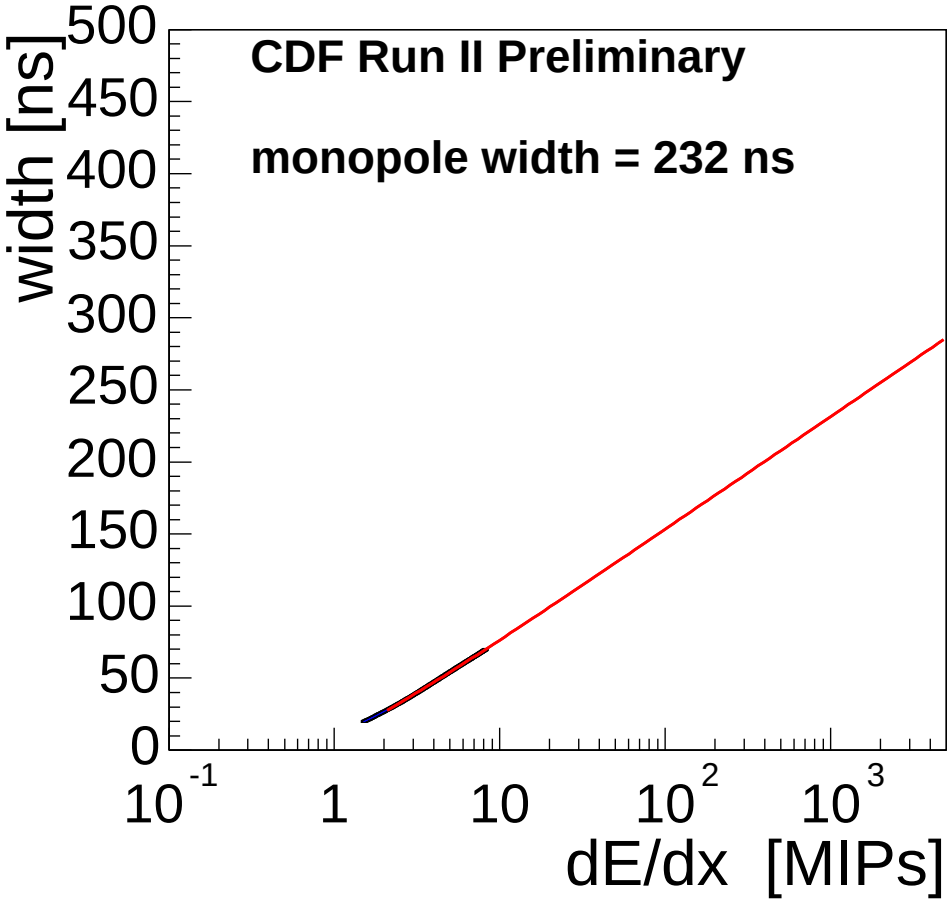

Figure 7-4: Using a logarithmic extrapolation, we find the expected response to a monopole. At 232 ns, it is within the dynamic range of the COT. In fact, their are many individual hits with widths much greater. Nonetheless, we take care not to cut far beyond the dynamic range of ordinary tracks.

ordinary tracks.

The raw hit distribution from tracks with a truncated average width greater than 100, 110, 120, and 130 ns is shown in Figure 7-5. Early on, each successively larger width cut reduces the number or tracks by nearly an order of magnitude, but by 130 ns to 140 ns there is little to be gained by cutting harder; we are in the tail. For this reason, we cut at 140 ns, in the tail of the distribution from ordinary matter, but far below the expected response from a monopole. For this reason, the width cut will have a negligible effect on the efficiency.

To check the run dependence of the COT response, we compare the corrected universal curve calculated with the first 20% of the data with the last 20% of the data. The curve remains in good agreement, as shown in Figure 7-6.

7.2 Segment Finding

The monopole segment finding algorithm is a modified version of the default COT segment finding algorithm [41] that adds a minimum width and allows for a variable time-of-flight to each super-layer. A monopole candidate consists of several ϕ_0 coincident monopole segments with small curvature. The width cut was already considered above.

In Monte Carlo, the track segments from monopoles have very small curvature and are coincident in segment ϕ_0. As shown in Figure 7-7, a cut on the curvature ρ requiring $\rho < .001$ m^{-1} is highly efficient. Likewise, Figure 7-8 shows that a ϕ_0 tolerance of 0.2 radians for counting coincident segments is extremely loose.

By ignoring the width cut, the segment finding algorithm efficiency is measured using high p_{T} tracks. The efficiency dependence on the minimum number of hits allowed in a segment and the minimum number of coincident segments is shown in Figure 7-9. We choose a highly efficient cut requiring 7 coincident super-layers with at least 8 hits in each segment.

We also measure the algorithm's efficiency on monopoles, using Monte Carlo. With Monte Carlo, the efficiency for intermediate or high mass monopoles is nearly

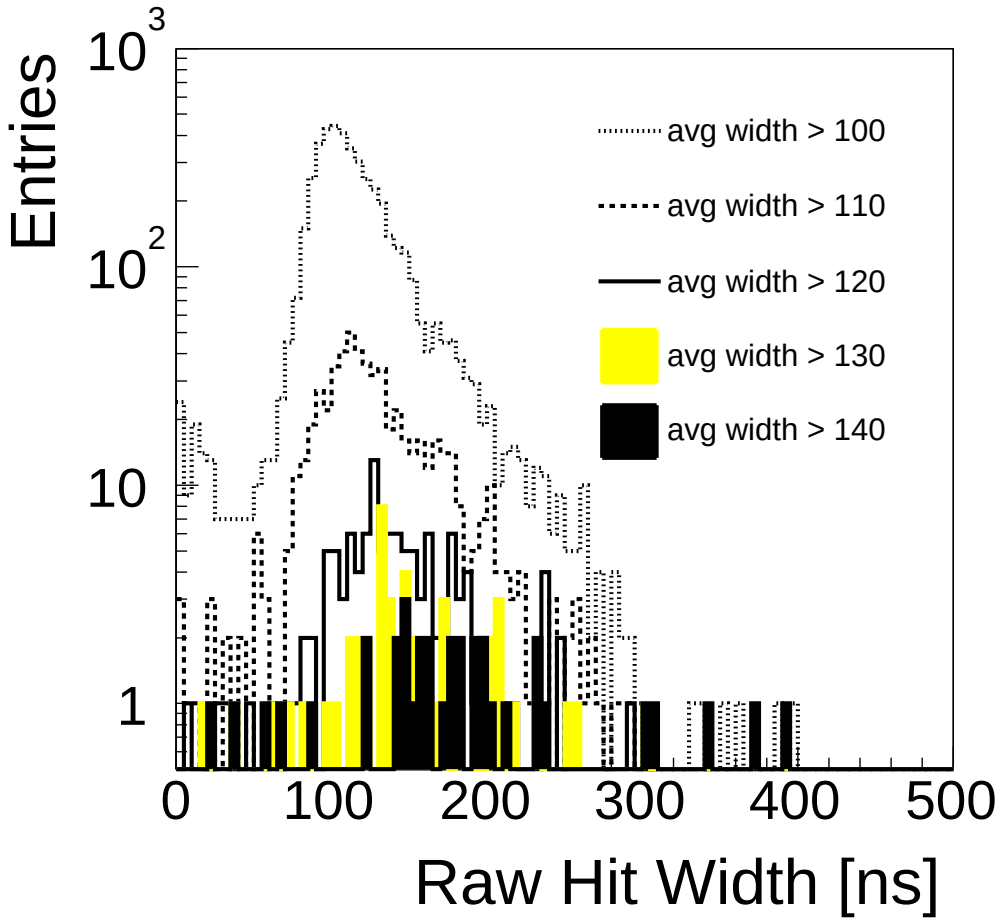

Figure 7-5: The raw hit distributions for ordinary tracks with cuts on the truncated average dE/dx. There is little to be gained by cutting above 140 ns. Although our expected response to a monopole is 232 ns, we cut at 140 ns to remain inside the dynamic range of ordinary tracks.

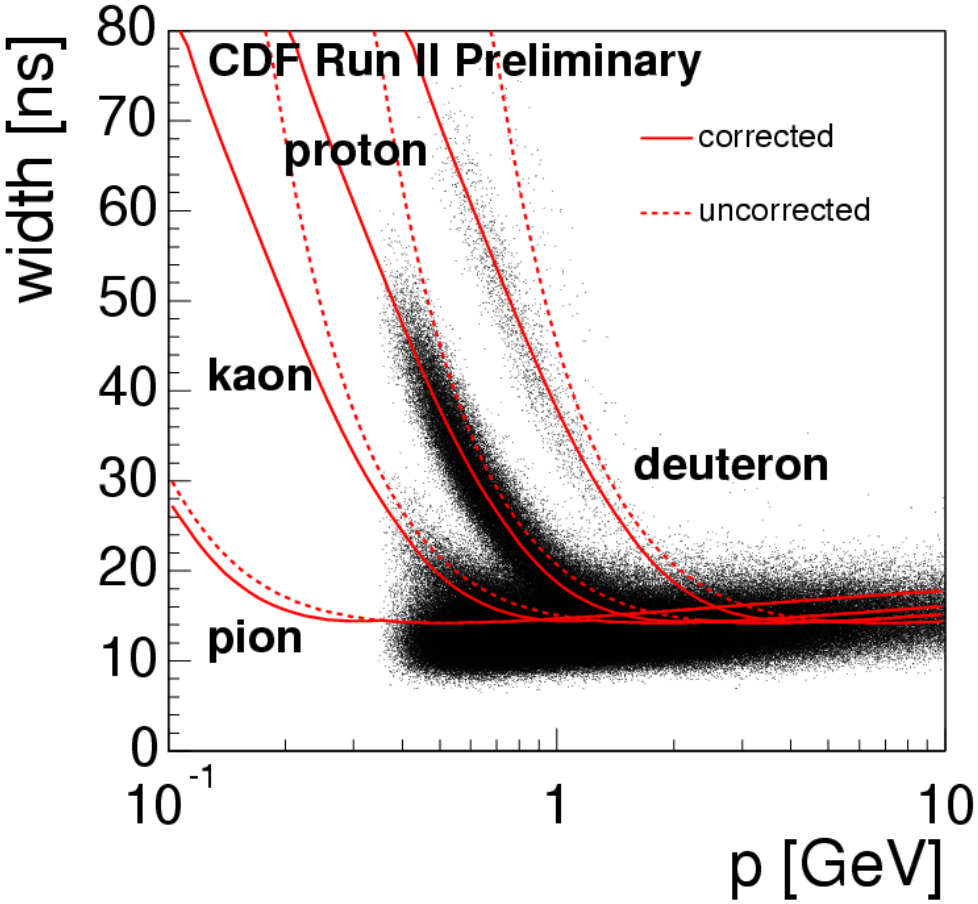

Figure 7-6: To check the run dependence of the cot width calibration, we check how well the corrected universal curve calculated using the first 20% of the data describes the last 20% of the data.

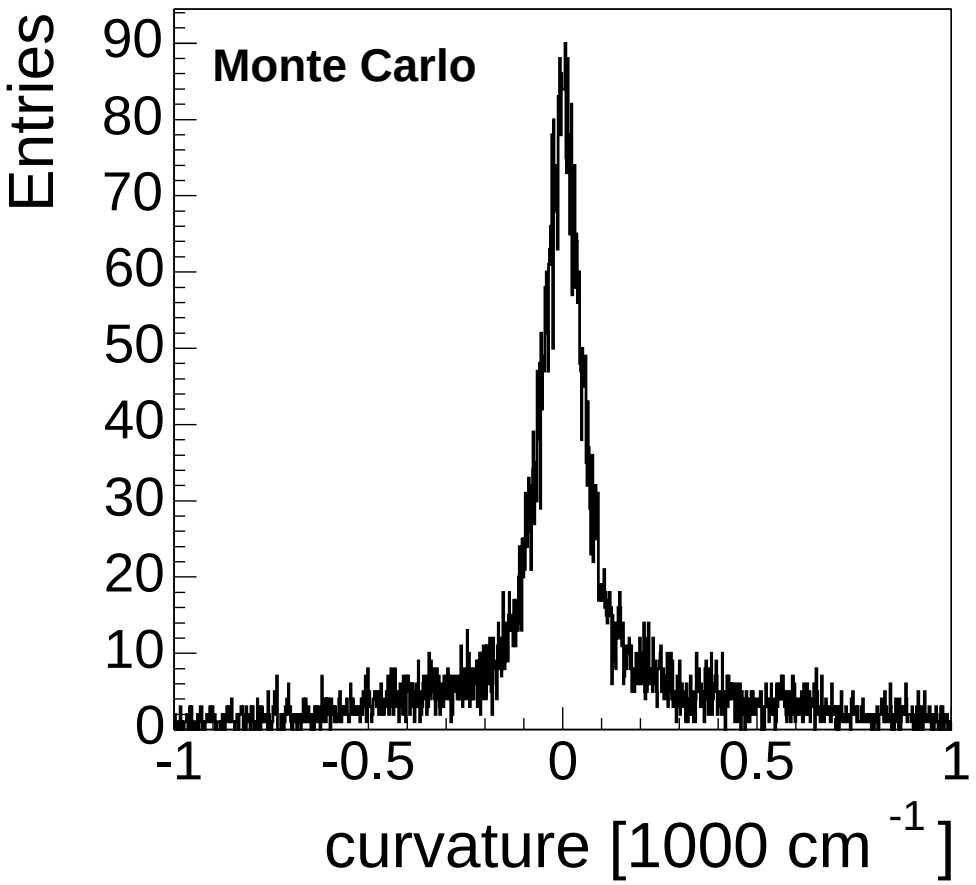

Figure 7-7: The curvature of segments from Monte Carlo monopoles. Our requirement that $\rho < 0.001$ m^{-1} is a loose cut.

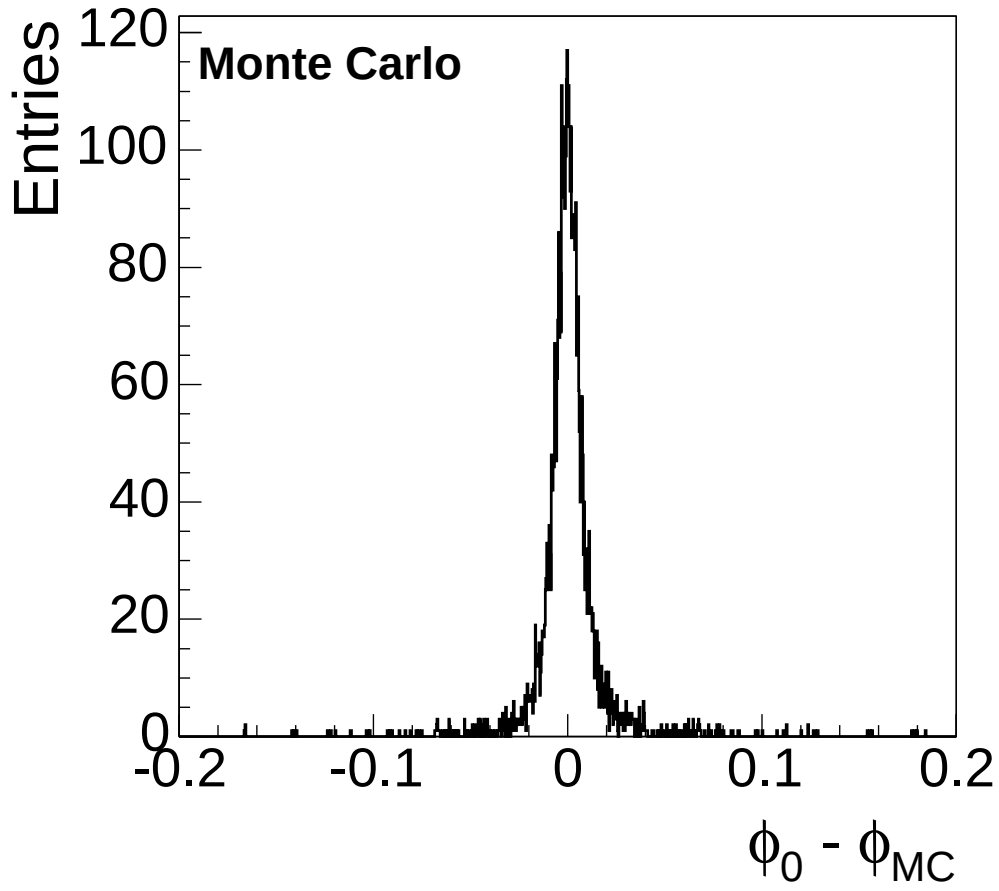

Figure 7-8: Comparison of the segment ϕ_0 with the monopoles true ϕ direction in Monte Carlo. We consider wedges to be ϕ coincident if they are within 0.2 radians, a loose cut.

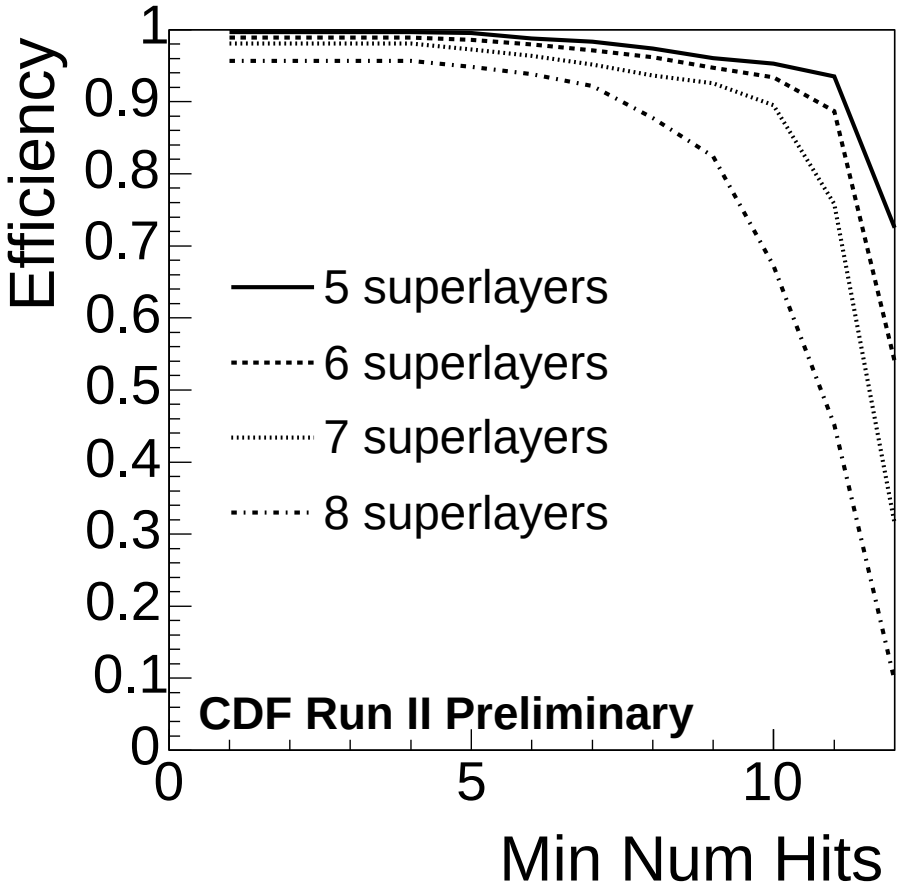

Figure 7-9: By removing the high dE/dx requirement, the efficiency of the segment finding algorithm is measured on high p_{T} tracks. Requiring 7 segments with at least 8 hits each is $94\% \pm 5\%$ efficient.

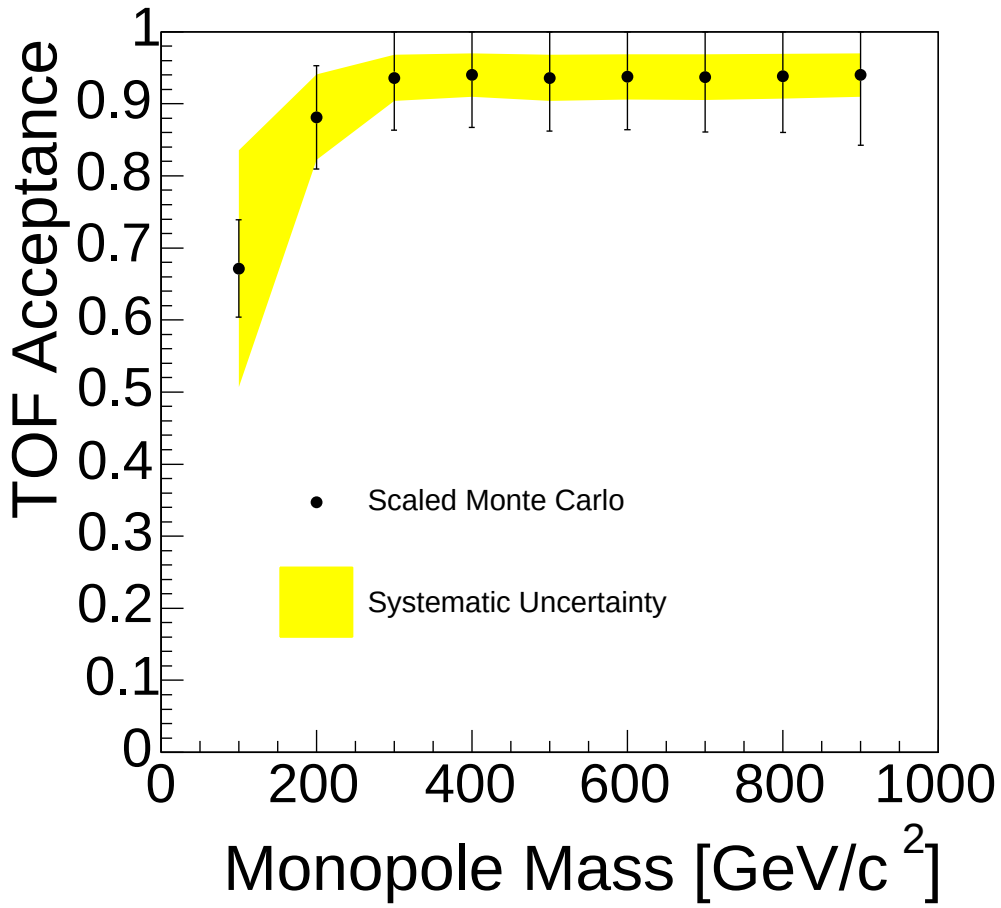

Figure 7-10: The efficiency of the segment finding algorithm using Monte Carlo, scaled by the efficiency measured in data with high p_{T} tracks. The lower mass monopoles are relativistic, and produce delta rays that confuse the pattern recognition.

100%, which is optimistic. To correct this, we scale the Monte Carlo efficiency by the high p_{T} efficiency, and obtain the efficiency shown in Figure 7-10. One half the total inefficiency is taken as a systematic error: 3% for intermediate masses.

Low mass monopoles are relativistic, and the production of delta rays alters the monopole trajectory and confuses the segment finding algorithm. The GEANT simulation explicitly produces delta rays, and their effect is clearly visible in Figure 7-10.

As an additional cross check, we test the algorithm efficiency on the GEANT simulation of Uranium, which has been validated on data and also produces large amounts of delta rays. The Uranium is modified to ignore the magnetic field, causing non-curving trajectories like a monopole, and produced with a velocity characteristic of intermediate mass monopoles. For one thousand Uranium events with $\beta\gamma = 0.8$, every event passed the segment finding criteria.

To estimate how effective these requirements will be at rejecting background, we use minimum bias data. The maximum number of coincident segments found for a given minimum number of hits in each segment is shown in Figure 7-11. Out of 800 thousand events, only a few had a two-fold coincidence of segments with at least 7 hits. We require a seven-fold coincidence of 8 hits or more.

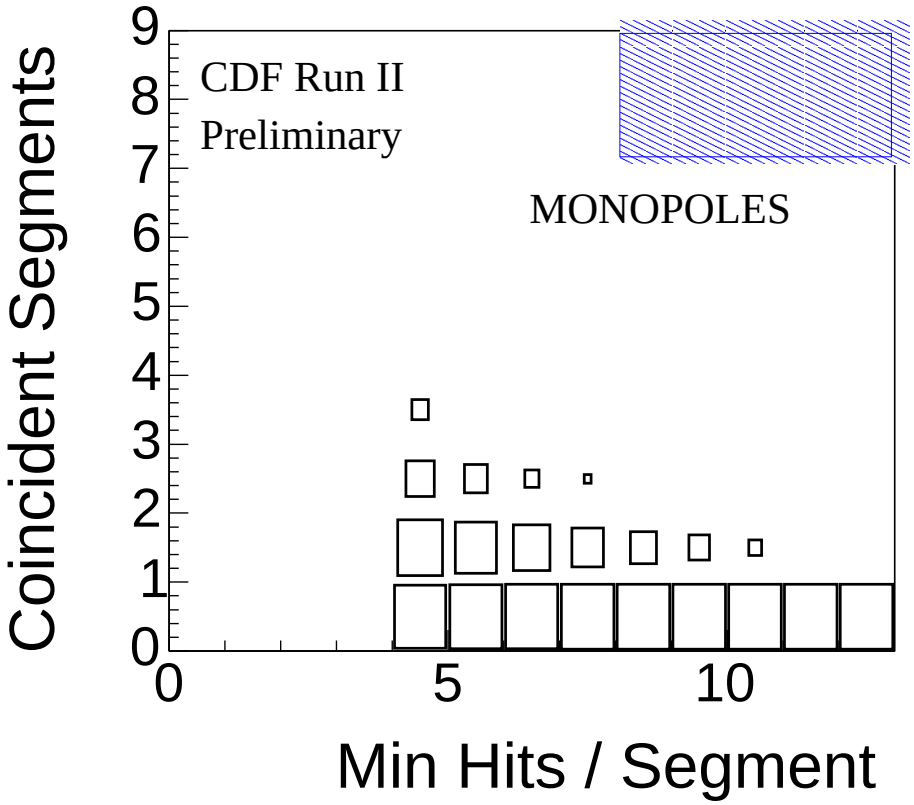

Figure 7-11: A background estimate from minimum bias data. The monopole width and curvature requirements are applied to segments, then the number of coincident segments for a minimum number of hits per segment is counted. There is extremely little background to a sevenfold coincidence with more than 8 hits per segment.

Chapter 8

Results

No events from the 35.7 pb^{-1} monopole trigger sample pass the monopole candidate selection criteria. Based on this result, we set a monopole cross section limit and a monopole mass limit.

The expected number of events N from a process with cross section σ and detector efficiency ϵ after integrated luminosity L is given by:

$$N = L\epsilon\sigma \ .$$

A cross section sensitivity is thus given by

$$\sigma^* = N^*/L\epsilon \ .$$

Where now N^* is the experimentally determined upper limit on the number of signal events. Using Bayesian statistics, N^* absorbs the fractional uncertainty in the total acceptance and luminosity. Typically, N^* also depends on the number of expected background events and the uncertainty, but in the case of zero observed events it does not. For a 95% CL limit with a 0.1 fractional uncertainty on the acceptance and zero observed events $N^* = 3.084$.

The efficiency of this search is summarized in Table 8.1. The primary factor in the efficiency is the TOF acceptance, roughly 70% for monopole masses near 500 GeV.

Effect	Efficiency	Statistical Uncertainty	Systematic Uncertainty
TOF acceptance (MC)	Figure 6-1	Figure 6-1	Figure 6-1
TOF response	100%	negl.	negl.
TOF spoilers	86%	1%	5%
TOF timing (MC)	Figure 6-19	Figure 6-19	Figure 6-19
TOF digital	100%	negl.	negl.
COT width cut	100%	negl.	negl.
COT segment finding	Figure 7-10	Figure 7-10	Figure 7-10

Table 8.1: The efficiency of the monopole search.

The only other major source of inefficiency is the spoiler effect, where an early arriving ordinary track screens the TOF from the monopole, with an efficiency of 86%. The offline candidate selection efficiency is 94% efficient because the monopole's unique signature allows for loose cuts. The remaining factors are all much smaller.

The cross section exclusion limit, using the Bayesian method, is shown in Figure 8-1 for a monopole with charge quantum number $n = 1$. The production cross section for the Drell-Yan like mechanism intersects the cross section limit at the mass limit $m > 360$ GeV. Mass limits for any production model can be obtained in this manner, provided the kinematics are not dramatically different than those considered in Section 6.1.

An additional limit for an $n = 2$ monopole is shown in Figure 8-2. Even though the acceptance is reduced, the larger production cross section results in a higher mass limit $m > 390$ GeV. For $n = 3$ and higher, the acceptance is smaller than the uncertainty, and no meaningful limit can be set.

A comparison of our cross section limit with other recent limits is shown in Figure 8-3. Care must be taken when using this figure; the monopole production cross section depends on the experiment, meaning that the theory curves will differ. Ours is the present best limit at high mass.

It is instructive to consider looser cuts. We repeat the minimum bias background estimation from Figure 7-11 with trigger data in Figure 8-4. The background closely resembles the result for minimum bias data; the background is extremely far from

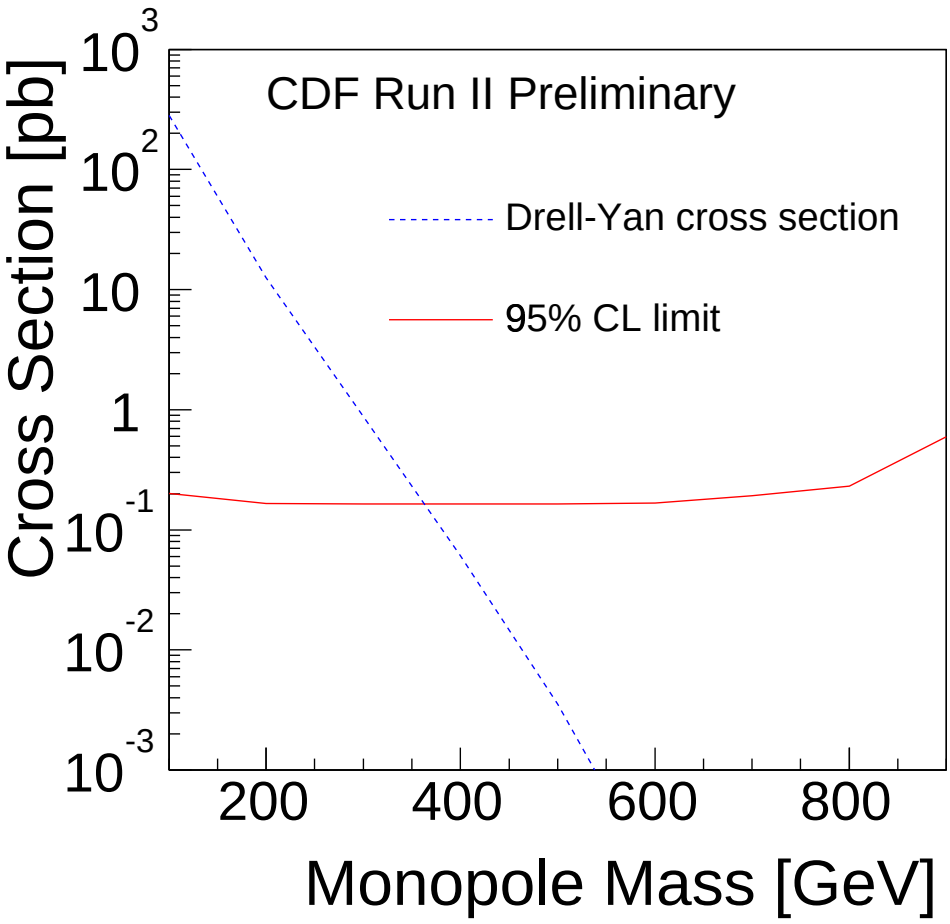

Figure 8-1: Cross section limit at 95% CL versus magnetic monopole mass, for an $n = 1$ monopole. The excluded region is above.

the monopole candidate requirements.

With the COT width cut reduced to 100 ns, several events pass the remaining cuts, all pointing to the same TOF bar. One of the events is shown in Figure 8-5. This width cut is now well within the reach of ordinary tracks, as demonstrated in Figure 7-5. A particle has high enough dE/dx to trigger the most sensitive bar, pass the weakened COT dE/dx cut, but with high enough momentum to pass the loose curvature cut. The curvature is for a positive charge in all three cases; it is likely a high mass particle such as deuteron.

Had a magnetic monopole candidate been discovered, additional measurements

would be interesting. From the monopoles time-of-flight and trajectory in the magnetic field, the charge to mass ratio g/m could be determined. A determination of the charge g could be made by comparing the measured energy loss in the COT to that of a MIP particle with the same velocity. The energy loss measurement uncertainty is dominated by energy loss fluctuations. Initial performance measurements find that for typical tracks the energy loss resolution is about 15%. Energy loss fluctuations do not increase linearly with the energy loss, so the performance for highly ionizing monopoles should be even better:

$$\sigma(g^2)/g^2 = \sigma(E)/E < \sigma(E_{\mathrm{MIP}})/E_{\mathrm{MIP}} = 0.15$$

We expect that the charge could be accurately determined for a monopole candidate.

The negative result has little cosmological import, as the monopoles required by Grand Unified Theories have characteristic masses $m \sim 10^{17}$ TeV. However, we can ignore this harsh reality and assume that monopoles might still have been produced by the early universe at a lower mass. In this case, our limit also places a limit on the recombination of monopole pairs into leptons and quarks, and determines the density that would remain today.

Assuming the monopole pairs where frozen out, as in GUT theories, at a temperature equal to their mass, there would be an ideal gas of monopoles with luminosity

$$L \sim (N^2/V)\sqrt{3kT/m}$$

Our cross section limit places a restriction on the rate of change of the monopole density:

$$-d\rho/dt < \rho^2 \cdot \sqrt{3kT/m} \cdot \sigma_*$$

which has a characteristic decay time $\tau = \sqrt{m/3kT}/(\rho\sigma_*)$. We calculate the density with a characteristic decay time of the age of the universe, assuming that at freeze-out $m/kT \sim 1$, and find that the stable density of monopoles is huge: $\rho = 10^{10}\ cm^{-3}$. This is another way of interpreting our null result; if monopoles of this mass were

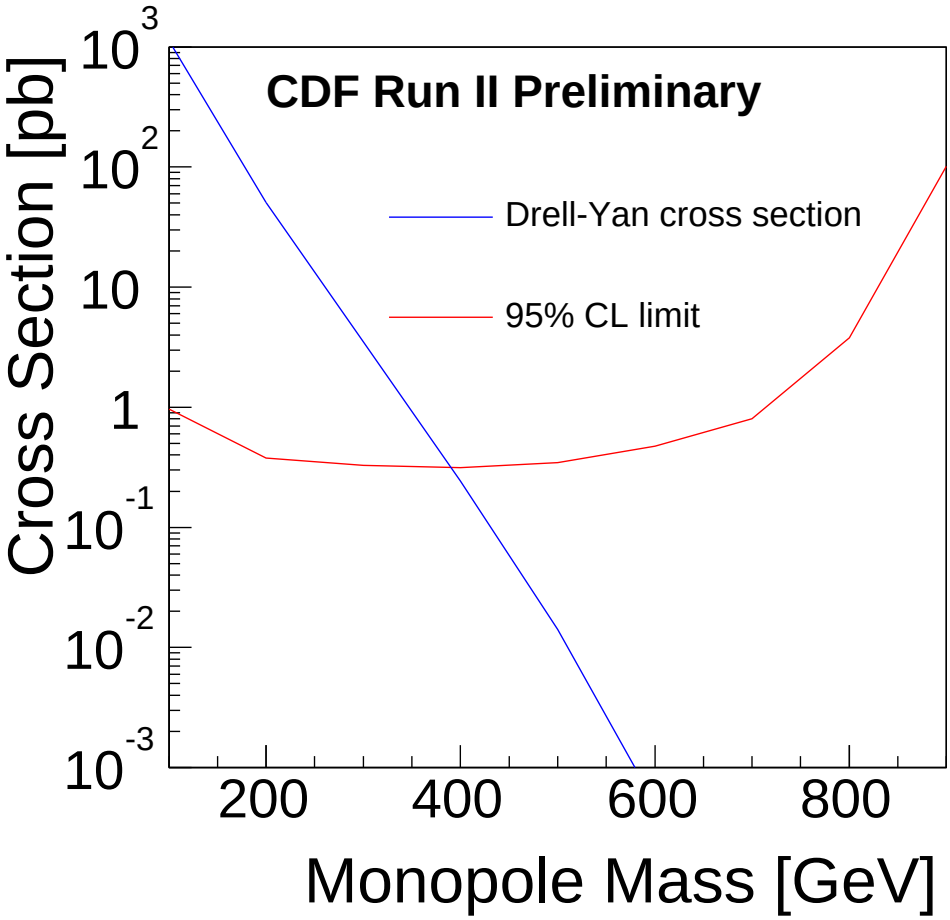

Figure 8-2: Cross section limit at 95% CL versus magnetic monopole mass, for an $n = 2$ monopole. The excluded region is above.

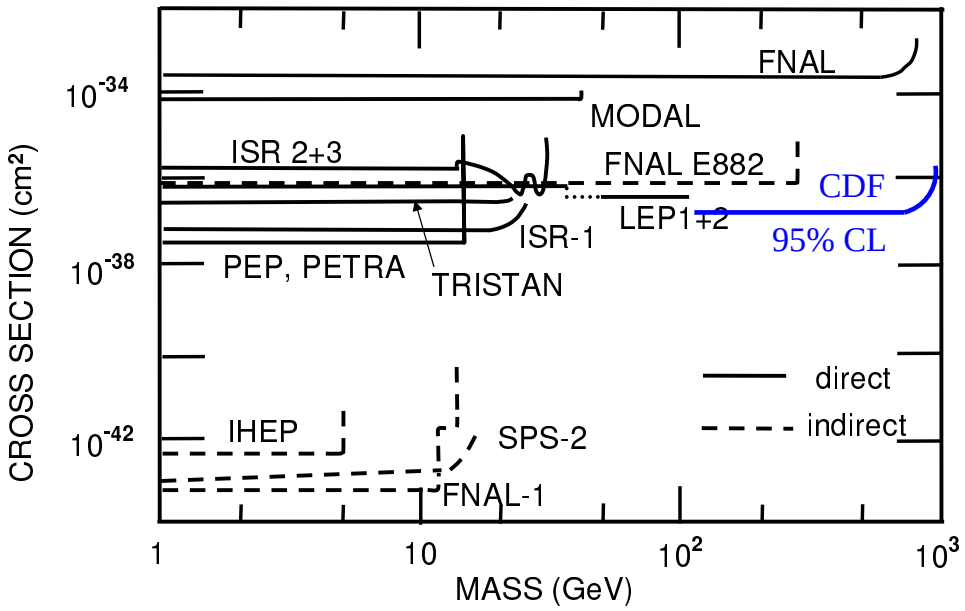

Figure 8-3: The present limit (approximate) is superimposed on a plot of current limits [6]. Ours is the present best limit at high mass.

produced by the early universe, they would still have been around today.

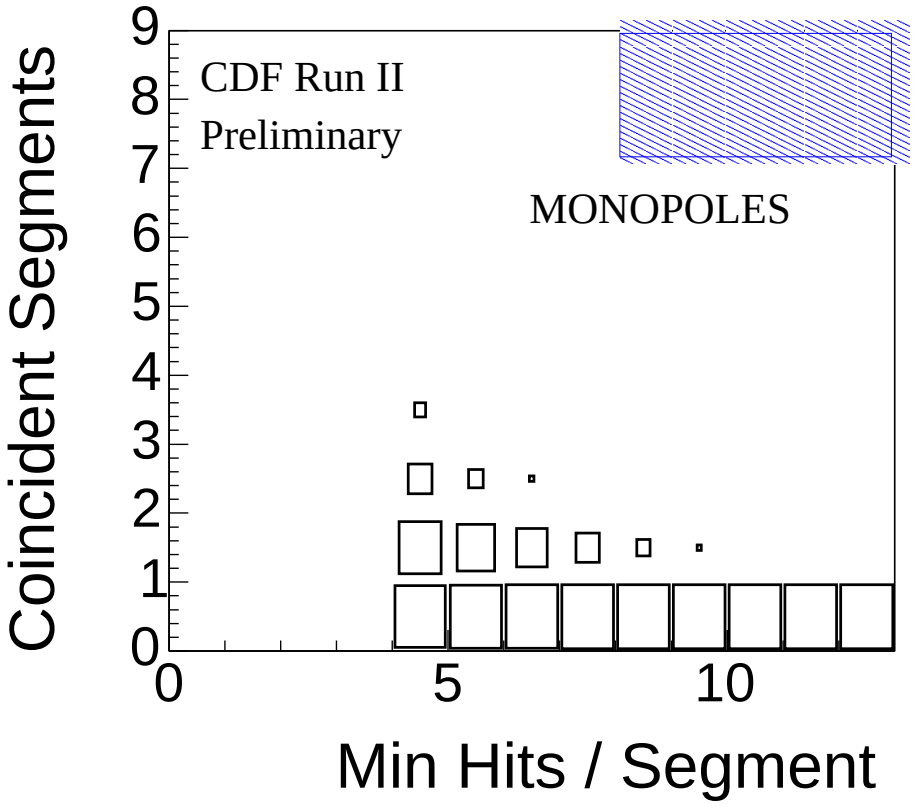

Figure 8-4: A background estimate from trigger data. The monopole width and curvature requirements are applied to segments, then the number of coincident segments for a minimum number of hits per segment is counted. This closely resembles the minimum data in Figure 7-11.

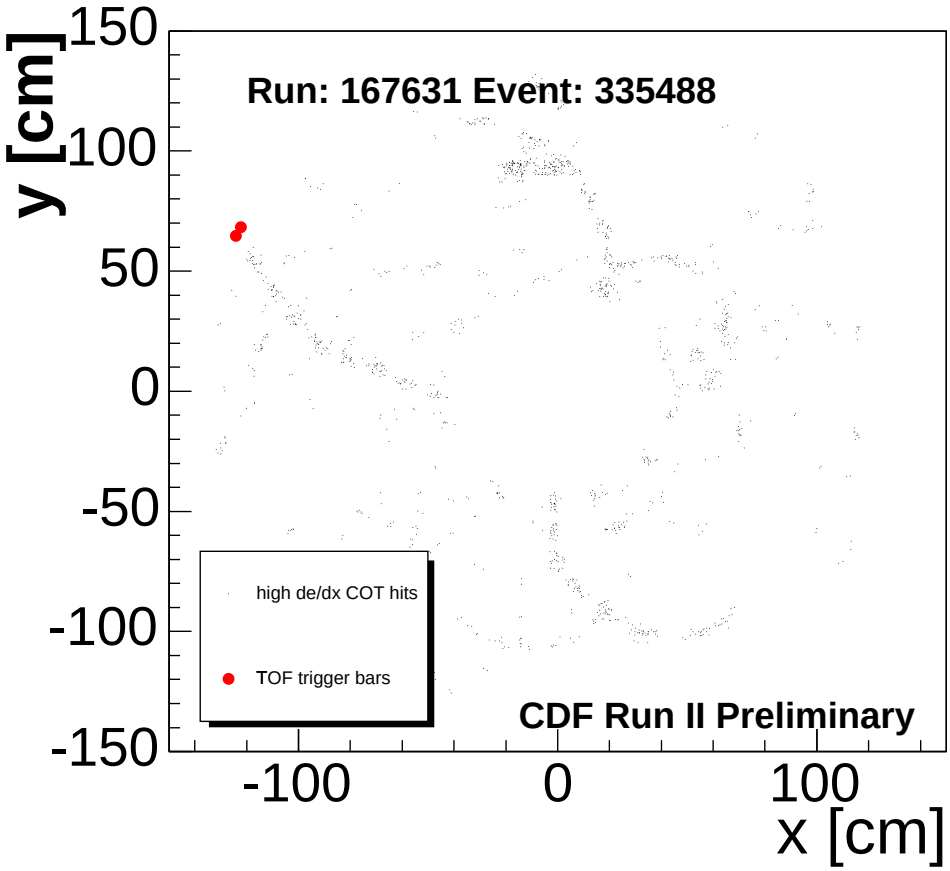

Figure 8-5: The nearest candidate, obtained by reducing the COT width cut to 100 ns, well within the reach of ordinary tracks. The triggered TOF bar is shown, as well as hits in the COT with width above the reduced threshold.

Appendix A

Time-of-Flight Trigger Details

This appendix contains technical details of the TOF trigger, including hardware locations, TOTRIB pin-outs, VME buffer addresses, and bit-wise channel interpretations.

front end crate	slots	TOF trigger hardware	neighbors
b0wcal00-b0wcal07	5-10	TOF ADMEM	Wall Calorimetry
b0cmx01	18-21	TOTRIB	Central Muon Extension
b0mutr00	7-18	Muon Matchbox	Muon Trigger
b0l1g00	6	BSC-TOF PreFRED (MIP decision)	Beam Shower Counter, Roman Pot, Miniplug
b0l1g00	10	Muon PreFRED (HIP decision)	Muon Trigger

Table A.1: The crate locations of hardware related to the TOF trigger.

FPGA	ped offset
1	0x34
2	0x38
3	0x3c
4	0x40
5	0x44

Table A.2: The VME address offset of the pedestal register for each trigger FPGA on an ADMEM.

Signal	Input	Output
CDF_CLK	J2-A-6	J3-38-D
CDF_B0*	J2-A-10	J3-38-C
CDF_RECOVER*	J2-A-18	J3-38-B
CDF_HALT*	J2-A-16	J3-38-A

Table A.3: The TOTRIB takes CDF control signals from the J2 backplane, modifies them as needed, and sends them to the Muon Transition Card through the J3 connector.

Signal	Input
CDF_CLK*	J2-A-7
CDF_BC*	J2-A-9
CDF_L1A*	J2-A-12
CDF_L2A*	J2-A-27
CDF_L2B0	J2-A-14
CDF_L2B1	J2-A-15

Table A.4: The TOTRIB uses additional CDF control signals taken from the J2 backplane.

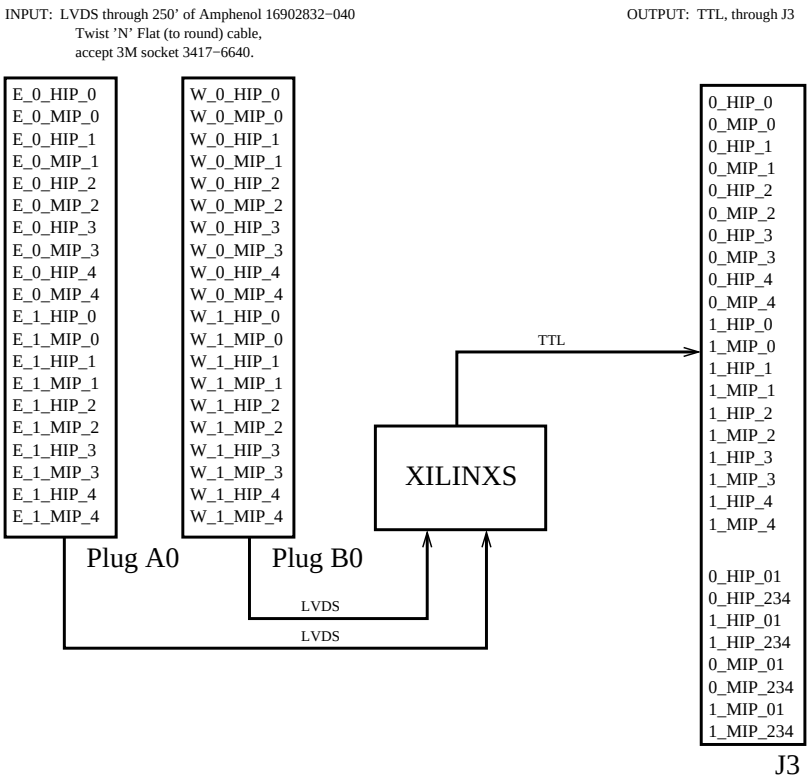

Figure A-1: Each of the TOTRIB coincidence unit FPGAs takes input from two front plane connectors, calculates coincidence data, and outputs it through the J3 backplane connector. Only the first of three FPGAs is shown.

		plug:		TOTRIB:							
		A0	B0	0		1		2		3	
chan	pins			phi	bars	phi	bars	phi	bars	phi	bars
0	1, 2	E_0_HIP_0	W_0_HIP_0	0°	0, 1	90°	54, 55	180°	108,109	270°	162,163
1	3, 4	E_0_MIP_0	W_0_MIP_0		0, 1		54, 55		108,109		162,163
2	5, 6	E_0_HIP_1	W_0_HIP_1		2, 3		56, 57		110,111		164,165
3	7, 8	E_0_MIP_1	W_0_MIP_1		2, 3		56, 57		110,111		164,165
4	9,10	E_0_HIP_2	W_0_HIP_2		4, 5		58, 59		112,113		166,167
5	11,12	E_0_MIP_2	W_0_MIP_2		4, 5		58, 59		112,113		166,167
6	13,14	E_0_HIP_3	W_0_HIP_3		6, 7		60, 61		114,115		168,169
7	15,16	E_0_MIP_3	W_0_MIP_3		6, 7		60, 61		114,115		168,169
8	17,18	E_0_HIP_4	W_0_HIP_4		8		62		116		170
9	19,20	E_0_MIP_4	W_0_MIP_4		8		62		116		170
10	21,22	E_1_HIP_0	W_1_HIP_0	15°	9, 10	105°	63, 64	195°	117,118	285°	171,172
11	23,24	E_1_MIP_0	W_1_MIP_0		9, 10		63, 64		117,118		171,172
12	25,26	E_1_HIP_1	W_1_HIP_1		11, 12		65, 66		119,120		173,174
13	27,28	E_1_MIP_1	W_1_MIP_1		11, 12		65, 66		119,120		173,174
14	29,30	E_1_HIP_2	W_1_HIP_2		13, 14		67, 68		121,122		175,176
15	31,32	E_1_MIP_2	W_1_MIP_2		13, 14		67, 68		121,122		175,176
16	33,34	E_1_HIP_3	W_1_HIP_3		15, 16		69, 70		123,124		177,178
17	35,36	E_1_MIP_3	W_1_MIP_3		15, 16		69, 70		123,124		177,178
18	37,38	E_1_HIP_4	W_1_HIP_4		17		71		125		179
19	39,40	E_1_MIP_4	W_1_MIP_4		17		71		125		179

Table A.5: TOTRIB input channel definitions (first 30°): the channel mapping of A0 and B0 plugs of the TOTRIB. As these are differential signals, each channel corresponds to two pins; the first pin is positive, the second negative. The physical location of the bars associated with each bit are listed by TOTRIB.

		plug:		TOTRIB:							
		A1	B1	0		1		2		3	
chan	pins			phi	bars	phi	bars	phi	bars	phi	bars
0	1, 2	E_2_HIP_0	W_2_HIP_0	30°	18, 19	120°	72, 73	210°	126,127	300°	180,181
1	3, 4	E_2_MIP_0	W_2_MIP_0		18, 19		72, 73		126,127		180,181
2	5, 6	E_2_HIP_1	W_2_HIP_1		20, 21		74, 75		128,129		182,183
3	7, 8	E_2_MIP_1	W_2_MIP_1		20, 21		74, 75		128,129		182,183
4	9,10	E_2_HIP_2	W_2_HIP_2		22, 23		76, 77		130,131		184,185
5	11,12	E_2_MIP_2	W_2_MIP_2		22, 23		76, 77		130,131		184,185
6	13,14	E_2_HIP_3	W_2_HIP_3		24, 25		78, 79		132,133		186,187
7	15,16	E_2_MIP_3	W_2_MIP_3		24, 25		78, 79		132,133		186,187
8	17,18	E_2_HIP_4	W_2_HIP_4		26		80		134		188
9	19,20	E_2_MIP_4	W_2_MIP_4		26		80		134		188
10	21,22	E_3_HIP_0	W_3_HIP_0	45°	27, 28	135°	81, 82	225°	135,136	315°	189,190
11	23,24	E_3_MIP_0	W_3_MIP_0		27, 28		81, 82		135,136		189,190
12	25,26	E_3_HIP_1	W_3_HIP_1		29, 30		83, 84		137,138		191,192
13	27,28	E_3_MIP_1	W_3_MIP_1		29, 30		83, 84		137,138		191,192
14	29,30	E_3_HIP_2	W_3_HIP_2		31, 32		85, 86		139,140		193,194
15	31,32	E_3_MIP_2	W_3_MIP_2		31, 32		85, 86		139,140		193,194
16	33,34	E_3_HIP_3	W_3_HIP_3		33, 34		87, 88		141,142		195,196
17	35,36	E_3_MIP_3	W_3_MIP_3		33, 34		87, 88		141,142		195,196
18	37,38	E_3_HIP_4	W_3_HIP_4		35		89		143		197
19	39,40	E_3_MIP_4	W_3_MIP_4		35		89		143		197

Table A.6: TOTRIB input channel definitions (second 30°): the channel mapping of A1 and B1 plugs of the TOTRIB. As these are differential signals, each channel corresponds to two pins; the first pin is positive, the second negative. The physical location of the bars associated with each bit are listed by TOTRIB.

		plug:		TOTRIB:							
		A2	B2	0		1		2		3	
chan	pins			phi	bars	phi	bars	phi	bars	phi	bars
0	1, 2	E_4_HIP_0	W_4_HIP_0	60°	36, 37	150°	90, 91	240°	144,145	330°	198,199
1	3, 4	E_4_MIP_0	W_4_MIP_0		36, 37		90, 91		144,145		198,199
2	5, 6	E_4_HIP_1	W_4_HIP_1		38, 39		92, 93		146,147		200,201
3	7, 8	E_4_MIP_1	W_4_MIP_1		38, 39		92, 93		146,147		200,201
4	9,10	E_4_HIP_2	W_4_HIP_2		40, 41		94, 95		148,149		202,203
5	11,12	E_4_MIP_2	W_4_MIP_2		40, 41		94, 95		148,149		202,203
6	13,14	E_4_HIP_3	W_4_HIP_3		42, 43		96, 97		150,151		204,205
7	15,16	E_4_MIP_3	W_4_MIP_3		42, 43		96, 97		150,151		204,205
8	17,18	E_4_HIP_4	W_4_HIP_4		44		98		152		206
9	19,20	E_4_MIP_4	W_4_MIP_4		44		98		152		206
10	21,22	E_5_HIP_0	W_5_HIP_0	75°	45, 46	165°	99,100	255°	153,154	345°	207,208
11	23,24	E_5_MIP_0	W_5_MIP_0		45, 46		99,100		153,154		207,208
12	25,26	E_5_HIP_1	W_5_HIP_1		47, 48		101,102		155,156		209,210
13	27,28	E_5_MIP_1	W_5_MIP_1		47, 48		101,102		155,156		209,210
14	29,30	E_5_HIP_2	W_5_HIP_2		49, 50		103,104		157,158		211,212
15	31,32	E_5_MIP_2	W_5_MIP_2		49, 50		103,104		157,158		211,212
16	33,34	E_5_HIP_3	W_5_HIP_3		51, 52		105,106		159,160		213,214
17	35,36	E_5_MIP_3	W_5_MIP_3		51, 52		105,106		159,160		213,214
18	37,38	E_5_HIP_4	W_5_HIP_4		53		107		161		215
19	39,40	E_5_MIP_4	W_5_MIP_4		53		107		161		215

Table A.7: TOTRIB input channel definitions (last 30°): the channel mapping of A2 and B2 plugs of the TOTRIB. As these are differential signals, each channel corresponds to two pins; the first pin is positive, the second negative. The physical location of the bars associated with each bit are listed by TOTRIB.

Trigger Bit	J3 pin	Muon Hotlink
0_HIP_0	J3-23-A	OUT_A_0
0_MIP_0	J3-23-B	OUT_A_1
0_HIP_1	J3-23-C	OUT_A_2
0_MIP_1	J3-23-D	OUT_A_3
0_HIP_2	J3-23-E	OUT_A_4
0_MIP_2	J3-24-A	OUT_A_5
0_HIP_3	J3-24-B	OUT_A_6
0_MIP_3	J3-24-C	OUT_A_7
0_HIP_4	J3-24-D	OUT_A_8
0_MIP_4	J3-24-E	OUT_A_9
0_HIP_01	J3-25-A	OUT_A_10
0_HIP_234	J3-25-B	OUT_A_11
0_MIP_01	J3-27-E	OUT_A_24*
0_MIP_234	J3-28-A	OUT_A_25*
1_HIP_0	J3-25-C	OUT_A_12
1_MIP_0	J3-25-D	OUT_A_13
1_HIP_1	J3-25-E	OUT_A_14
1_MIP_1	J3-26-A	OUT_A_15
1_HIP_2	J3-26-B	OUT_A_16
1_MIP_2	J3-26-C	OUT_A_17
1_HIP_3	J3-26-D	OUT_A_18
1_MIP_3	J3-26-E	OUT_A_19
1_HIP_4	J3-27-A	OUT_A_20
1_MIP_4	J3-27-B	OUT_A_21
1_HIP_01	J3-27-C	OUT_A_22
1_HIP_234	J3-27-D	OUT_A_23
1_MIP_01	J3-28-B	OUT_A_26*
1_MIP_234	J3-28-C	OUT_A_27*

Table A.8: TOTRIB output channel mapping (first 30°): The logical trigger bits are output through a J3 pin associated with the hotlink for the correct 30° wedge. Entries marked * are unavailable for readout at Level 2.

Trigger Bit	J3 pin	Muon Hotlink
2_HIP_0	J3-29-C	OUT_B_0
2_MIP_0	J3-29-D	OUT_B_1
2_HIP_1	J3-29-E	OUT_B_2
2_MIP_1	J3-30-A	OUT_B_3
2_HIP_2	J3-30-B	OUT_B_4
2_MIP_2	J3-30-C	OUT_B_5
2_HIP_3	J3-30-D	OUT_B_6
2_MIP_3	J3-30-E	OUT_B_7
2_HIP_4	J3-31-A	OUT_B_8
2_MIP_4	J3-31-B	OUT_B_9
2_HIP_01	J3-31-C	OUT_B_10
2_HIP_234	J3-31-D	OUT_B_11
2_MIP_01	J3-37-B	OUT_B_24*
2_MIP_234	J3-37-C	OUT_B_25*
3_HIP_0	J3-31-E	OUT_B_12
3_MIP_0	J3-32-A	OUT_B_13
3_HIP_1	J3-32-B	OUT_B_14
3_MIP_1	J3-32-C	OUT_B_15
3_HIP_2	J3-32-D	OUT_B_16
3_MIP_2	J3-32-E	OUT_B_17
3_HIP_3	J3-33-A	OUT_B_18
3_MIP_3	J3-33-B	OUT_B_19
3_HIP_4	J3-33-C	OUT_B_20
3_MIP_4	J3-33-D	OUT_B_21
3_HIP_01	J3-33-E	OUT_B_22
3_HIP_234	J3-37-A	OUT_B_23
3_MIP_01	J3-37-D	OUT_B_26*
3_MIP_234	J3-37-E	OUT_B_27*

Table A.9: TOTRIB output channel mapping (second 30°) : The logical trigger bits are output through a J3 pin associated with the hotlink for the correct 30° wedge. Entries marked * are unavailable for readout at Level 2.

Trigger Bit	J3 pin	Muon Hotlink
4_HIP_0	J3-1-A	OUT_C_0
4_MIP_0	J3-1-B	OUT_C_1
4_HIP_1	J3-1-C	OUT_C_2
4_MIP_1	J3-1-D	OUT_C_3
4_HIP_2	J3-1-E	OUT_C_4
4_MIP_2	J3-2-A	OUT_C_5
4_HIP_3	J3-2-B	OUT_C_6
4_MIP_3	J3-2-C	OUT_C_7
4_HIP_4	J3-2-D	OUT_C_8
4_MIP_4	J3-2-E	OUT_C_9
4_HIP_01	J3-3-A	OUT_C_10
4_HIP_234	J3-3-B	OUT_C_11
4_MIP_01	J3-28-D	OUT_C_24*
4_MIP_234	J3-28-E	OUT_C_25*
5_HIP_0	J3-3-C	OUT_C_12
5_MIP_0	J3-3-D	OUT_C_13
5_HIP_1	J3-3-E	OUT_C_14
5_MIP_1	J3-4-A	OUT_C_15
5_HIP_2	J3-4-B	OUT_C_16
5_MIP_2	J3-4-C	OUT_C_17
5_HIP_3	J3-4-D	OUT_C_18
5_MIP_3	J3-4-E	OUT_C_19
5_HIP_4	J3-5-A	OUT_C_20
5_MIP_4	J3-5-B	OUT_C_21
5_HIP_01	J3-5-C	OUT_C_22
5_HIP_234	J3-5-D	OUT_C_23
5_MIP_01	J3-29-A	OUT_C_26*
5_MIP_234	J3-29-B	OUT_C_27*

Table A.10: TOTRIB output channel mapping (last 30°): The logical trigger bits are output through a J3 pin associated with the hotlink for the correct 30° wedge. Entries marked * are unavailable for readout at Level 2.

Pins	Output Bit
1,2	0_MIP
3,4	1_MIP
5,6	2_MIP
7,8	3_MIP
9,10	4_MIP
11,12	5_MIP

Table A.11: TOTRIB MIP front-panel connector A3 channel mapping : The first output connector contains the MIP hit pattern for 15° wedges. It is in LVDS format. The first pin is positive, the second pin is negative. (Note: in original specs, this was B3)

Pins	Output Bit
1,2	MIP_SUM(0)
3,4	MIP_SUM(1)
5,6	MIP_SUM(2)
7,8	MIP_SUM(3)
9,10	MIP_SUM(4)

Table A.12: TOTRIB MIP front-panel connector B3 channel mapping : The second output connector contains the total number of MIP coincidences in the 90 degrees covered by the TOTRIB. It is in LVDS format with a programmable delay. The first pin is positive, the second pin is negative. (Note: in original specs, this was A3)

pins	trigger bit
1,2	0_HIP_0
3,4	0_HIP_1
5,6	0_HIP_2
7,8	0_HIP_3
9,10	0_HIP_4
11,12	1_HIP_0
13,14	1_HIP_1
15,16	1_HIP_2
17,18	1_HIP_3
19,20	1_HIP_4
21,22	2_HIP_0
23,24	2_HIP_1
25,26	2_HIP_2
27,28	2_HIP_3
29,30	2_HIP_4
31,32	3_HIP_0
33,34	3_HIP_1
35,36	3_HIP_2
37,38	3_HIP_3
39,40	3_HIP_4
41,42	4_HIP_0
43,44	4_HIP_1
45,46	4_HIP_2
47,48	4_HIP_3
49,50	4_HIP_4
51,52	5_HIP_0
53,54	5_HIP_1
55,56	5_HIP_2
57,58	5_HIP_3
59,60	5_HIP_4

Table A.13: TOTRIB C0 connector output channel mapping: The first board mounted connector outputs the raw HIP coincidence data in LVDS format. As these are differential signals, each channel corresponds to two pins; the first pin is positive, the second negative.

pins	trigger bit
1,2	0_MIP_0
3,4	0_MIP_1
5,6	0_MIP_2
7,8	0_MIP_3
9,10	0_MIP_4
11,12	1_MIP_0
13,14	1_MIP_1
15,16	1_MIP_2
17,18	1_MIP_3
19,20	1_MIP_4
21,22	2_MIP_0
23,24	2_MIP_1
25,26	2_MIP_2
27,28	2_MIP_3
29,30	2_MIP_4
31,32	3_MIP_0
33,34	3_MIP_1
35,36	3_MIP_2
37,38	3_MIP_3
39,40	3_MIP_4
41,42	4_MIP_0
43,44	4_MIP_1
45,46	4_MIP_2
47,48	4_MIP_3
49,50	4_MIP_4
51,52	5_MIP_0
53,54	5_MIP_1
55,56	5_MIP_2
57,58	5_MIP_3
59,60	5_MIP_4

Table A.14: TOTRIB C1 connector output channel mapping: The second board mounted connector outputs the raw MIP coincidence data in LVDS format. As these are differential signals, each channel corresponds to two pins; the first pin is positive, the second negative.

register	offset
TOTRIB_IDPROM	0x100000
TOTRIB_CLKDELAY	0x400000
TOTRIB_BODELAY	0x400004
TOTRIB_RCVRLNG	0x400008
TOTRIB_JTAGREG	0x40000c
TOTRIB_L2BUF0	0x800000
TOTRIB_L2BUF1	0x900000
TOTRIB_L2BUF2	0xa00000
TOTRIB_L2BUF3	0xb00000

Table A.15: The VME address offsets for TOTRIB registers.

XTRP interpretation	TOF interpretation	XTRP bit	TCMD bit
A CMX Lo Crack	$\phi + 0^\circ$ to $\phi + 6\frac{2}{3}^\circ$	45	24
A CMX Hi Crack	$\phi + 6\frac{2}{3}^\circ$ to $\phi + 15^\circ$	44	26
B CMX Lo Crack	$\phi + 15^\circ$ to $\phi + 21\frac{2}{3}^\circ$	39	25
B CMX Hi Crack	$\phi + 21\frac{2}{3}^\circ$ to $\phi + 30^\circ$	38	27

Table A.16: TOF interpretation of the XTRP's crack bits. The muon trigger is divided into 30° wedges; here ϕ refers to the lowest ϕ of the wedge. The XTRP crack bits are also saved in the muon trigger data bank (TCMD).

FPGA	TOTRIB bits (T)	XTRP bits (X)	HIP decision
"East"	0-11, 24, 25	45, 44, 39, 38	$\mathrm{HIP}_{\mathrm{I},0}$ = (T(10) & X(45)) | (T(11) & X(44))
"West"	12-23, 26, 27	39, 38, 45, 44	$\mathrm{HIP}_{\mathrm{I},1}$ = (T(22) & X(39)) | (T(23) & X(38))

Table A.17: The order of HIP bits at the two FPGAs in each Muon Matchbox allows for identical HIP trigger logic in both devices.

Bibliography

[1] J.D. Jackson, *Classical Electrodynamics*, Second Edition. New York: de Gruyter, (1982).

[2] P.A.M. Dirac, *Quantized Singularities In The Electromagnetic Field*, Proc. R. Soc. (London), A133 (1931).

[3] I. De Mitri, *Search For Magnetic Monopoles in the Cosmic Radiation with the Macro Detector at Gran Sasso*, Budapest 2001, High energy physics, hep2001/213.

S. Cecchini et al., *Search for Magnetic Monopoles at the Chacaltaya Cosmic Ray Laboratory*, Nuovo Cim.24C:639-644 (2001).

S.D. Wick, T.W. Kephart, T.J. Weiler, P.L. Biermann, *Signatures for a Cosmic Flux of Magnetic Monopoles*, astro-ph/0001233 (2000).

[4] I.F. Ginzburg, A. Schiller, *Search For a Heavy Magnetic Monopole at the Tevatron and LHC*, Phys.Rev.D57:6599-6603 (1998), HEP-PH 9802310.

B. Abbot et al, *A Search for Heavy Pointlike Dirac Monopoles*, Fermilab-Pub-98/095-E (1998).

M. Acciarri et al., *Search for Anomalous $Z \to \gamma\gamma\gamma$ Events at Lep*, Phys. Lett. B345, 609-616 (1995).

L. Gamberg, G.R. Kalbfleisch, K.A. Milton, *Direct and Indirect Searches for Low-Mass Magnetic Monopoles*, hep-ph/9906526, (1999).

[5] G.R. Kalbfleisch, W. Luo, K.A. Milton, E.H. Smith, M.G. Strauss, *Limits on Production of Magnetic Monopoles Utilizing Samples from the D0 and CDF Detectors at the Tevatron*, hep-ex/0306045.

[6] G. Giacomelli, L. Patrizii, *Magnetic Monopole Searches*, Trieste 2002, Astroparticle physics and cosmology 121-144, hep-ex/0302011.

[7] J. Schwinger, L.L. DeRaad Jr., K.A. Milton, W. Tsai, *Classical Electrodynamics*, Reading, MA: Perseus Books, (1998).

M.E. Peskin, D.V. Schroeder, *An Introduction to Quantum Field Theory*, Reading, MA: Perseus Books, (1995).

[8] J. Schwinger, K.A. Milton, W. Tsai, L.L. DeRaad, D.C. Clark, *Nonrelativistic Dyon-Dyon Scattering*, Ann. Phys. (N.Y.) 101, 451 (1976)

L. Gamberg, K.A. Milton, *Dual quantum electrodynamics: Dyon-dyon and charge-monopole scattering in a high-energy approximation*, Phys. Rev. D 61, (2000).

L. Gamberg, K.A. Milton, *Eikonal scattering of monopoles and dyons in dual QED*, OKHEP-00-05, (2000).

[9] Particle Data Group, Eur. Phys. J. C3, 144 (1998).

[10] S. P. Ahlen, *Stopping Power Formula For Magnetic Monopoles,* Phys. Rev. D **17**, 229 (1978).

[11] *Fermilab's Chain of Accelerators*
`http://www-bd.fnal.gov/public/chain.html`

Fermilab Beams Division, *Run II Handbook*,
`http://www-bd.fnal.gov/runII/index.html`

[12] G. Aubrecht *et al.*, *A Teachers Guide to the Nuclear Science Wall Chart*, Contemporary Physics Education Project, 2003.
`http://www.lbl.gov/abc/wallchart/teachersguide/pdf/Chap11.pdf`

[13] C. W. Schmidt, *The Fermilab 400-MeV Linac upgrade* FERMILAB-CONF-93-111 (1993).

[14] J. Marriner, *Stochastic Cooling Overview*, FERMILAB-CONF-03-158 (2003).

[15] R. Blair *et al.*, *The CDF-II detector: Technical design report*, FERMILAB-PUB-96/390-E (1996). `http://www-cdf.fnal.gov/upgrades/tdr/tdr.html`

[16] F. Abe *et al.*, Nucl. Inst. and Meth. Phys. Res, **271A**, 387 (1988); FERMILAB-PUB-94/024-E (1994).

[17] T. K. Nelson *et al.* FERMILAB-CONF-01/357-E

[18] A. Sill *et al.*, Nucl. Instrum. Meth., **A447**, 1–8 (2000).

[19] T. Affolder *et al.*, Nucl. Instrum. Meth., **A485** , 6–9 (2002).

[20] K. T. Pitts *et al.*, FERMILAB-CONF-96-443-E

[21] CDF Collaboration, *A Time-Of-Flight System for CDF*, FERMILAB-PROPOSAL-0830-3 (1995). .

[22] C.M. Ginsburg, *CDF Run 2 Muon System*, FERMILAB-Conf-03/386-E (2004).

[23] R. Wagner *et al.*, *CDF Central Outer Tracker*, CDF Note 6267 (2003).

[24] G. Bauer et al., *Search for Magnetic Monopoles at CDF using the Time-of-Flight Detector*, CDF Note 5506 (2000);

N. Moggi and F. Rimondi, *A Simple Study for a TOF High Multiplicity Trigger*, CDF Note 5603 (2001);

M. Albrow, *Glueballs and Exclusive Hadron Production at the Tevatron*, CDF Note 5360 (1999).

[25] G. Bauer et al., *Proposal of a Level-1 Trigger using the Time-of-Flight Detector*, CDF Note 5597 (2001);

J. Lewis and D. Stuart, *A monopole trigger in Run II*, CDF Note 4697 (1998);

G. Bauer et al., *Time-of-Flight Trigger, Cable Design and Grounding Scheme* CDF Note 5709 (2001).

Trigger Cuts and Options.
`http://www-cdf.fnal.gov/trigger_database/Trigger_Options.pdf`

[26] C. Chen et al., *Electronics for the CDF Time-of-Flight Detector: a Status Report*, CDF Note 5361 (2000);

C. Chen et al., *Cables, Grounding and Shielding for the CDF-II Time-of-Flight System*, CDF Note 5340 (2000);

M. Jones, *PMT Base Design for the CDF-II Time-of-Flight System* CDF Note 5358 (2000);

C. Chen et al., *The Time-of-Flight Preamplifier* CDF Note 5362 (2000);

C. Chen et al., *Design and Implementation of TOAD Board for CDF-II Time-of-Flight System*, CDF Note 5632 (2001);

C. Chen et al., *CDF DECAF Daughter Board for Time-Of-Flight Detector*, CDF Note 5612 (2001);

S. Cabrera, *Tests and calibration of the photomultipliers of the CDF-II Time-of-Flight system*, CDF Note 5386 (2000).

[27] T. Shaw, *Specification for ADC/Memory Module*, CDF Note 4685 (1998);

T. Shaw and G. Sullivan, *The CDF Readout Crate*, CDF Note 2388 (1998);

[28] TOF ADMEM firmware written by T. Shaw.

[29] LVDS is defined by the `ANSI/ITA/EIA-644` standard.

[30] private communications with Eric James.

[31] E. J. Thomson *et al.*, IEEE Trans. Nucl. Sci **49**, 1063 (2002).

[32] *GEANT Detector Description and Simulation Tool*, CERN Program Library Writeup W5013, (1994).

[33] W.H. Press, B.P. Flannery, S.A. Teukolsky, W.T. Vetterling, *Numerical Recipes in Pascal*, Cambridge University Press, (1989).

[34] Rene Brun and Fons Rademakers, *ROOT - An Object Oriented Data Analysis Framework*, Proceedings AIHENP'96 Workshop, Lausanne, Sep. 1996, Nucl. Inst. & Meth. in Phys. Res. A 389 (1997) 81-86. `http://root.cern.ch/`

[35] M. Ambrosio et al., *Final Results of Magnetic Monopole Searches with the Macro Experiment.* Eur.Phys.J.C25:511-522, (2002) hep-ex/0207020

[36] G. Bauer et al., *Calibration of the Time-of-Flight Highly Ionizing Particle Trigger.* CDF Note 6935.

[37] G. Gomez et al., *Online Calibrations of the CDF-II Time-of-Flight Detector.* CDF Note 6050 (2002)

M. Jones, *Initial Performance Studies of the CDF-II Time-of-Flight Detector.* CDF Note 5930 (2002)

[38] G. Manca and Y. Kim, $Z \to e^+e^-$ *Cross-Section Measurement with Run II Data.* CDF Note 6202.

[39] "Luminosity Monitor Based on Cherenkov Counters for P-Pbar Colliders" Nucl. Instr. & Meth. A441, 366-373 (2000).

S.M. Wang, "The Uncertainty in the CLC Luminosity", Presentation at CDF joint physics meeting 12-Jul-2002.

[40] D. Ambrose et al., *dE/dx Studies*, CDF Note 6369.

D. Ambrose et al., *COT dE/dx Measurement and Corrections*, CDF note 6361.

[41] private communication about COT segment finding with Chris Hays.

[42] Torbjoern Sjoestrand, *Pythia 5.7 and Jetset 7.4 Physics and Manual*, (1998).